NASA/TM—2017-219071

Airborne Hyperspectral Sensing of Harmful Algal Blooms in the Great Lakes Region: System Calibration and Validation

From Photons to Algae Information: The Processes In-Between

John Lekki
Glenn Research Center, Cleveland, Ohio

Robert Anderson
Glenn Research Center, Cleveland, Ohio

Dulcinea Avouris
Kent State University, Kent, Ohio

Richard Becker
University of Toledo, Toledo, Ohio

James Churnside
NOAA Earth System Research Lab, Boulder, Colorado

Michael Cline
University of Toledo, Toledo, Ohio

James Demers
Glenn Research Center, Cleveland, Ohio

George Leshkevich
NOAA Great Lakes Environmental Research Lab, Ann Arbor, Michigan

Larry Liou
Glenn Research Center, Cleveland, Ohio

Jeffrey Luvall
NASA Marshall Space Flight Center, Huntsville, Alabama

Joseph Ortiz
Kent State University, Kent, Ohio

Anthony Royce
Glenn Research Center, Cleveland, Ohio

Steve Ruberg
NOAA Great Lakes Environmental Research Lab, Ann Arbor, Michigan

Reid Sawtell
Michigan Technological Research Institute, Ann Arbor, Michigan

Michael Sayers
Michigan Technological Research Institute, Ann Arbor, Michigan

Stephen Schiller
South Dakota State University, Brookings, South Dakota

Robert Shuchman
Michigan Technological Research Institute, Ann Arbor, Michigan

Anita Simic
Bowling Green State University, Bowling Green, Ohio

Dack Stuart
University of Michigan, Ann Arbor, Michigan

Glenn Sullivan
Michigan Technological Research Institute, Ann Arbor, Michigan

Paul Tavernelli
Glenn Research Center, Cleveland, Ohio

Roger Tokars
Glenn Research Center, Cleveland, Ohio

Andrea Vander Woude
University of Michigan, Ann Arbor, Michigan

February 2017

NASA STI Program . . . in Profile

Since its founding, NASA has been dedicated to the advancement of aeronautics and space science. The NASA Scientific and Technical Information (STI) Program plays a key part in helping NASA maintain this important role.

The NASA STI Program operates under the auspices of the Agency Chief Information Officer. It collects, organizes, provides for archiving, and disseminates NASA's STI. The NASA STI Program provides access to the NASA Technical Report Server—Registered (NTRS Reg) and NASA Technical Report Server—Public (NTRS) thus providing one of the largest collections of aeronautical and space science STI in the world. Results are published in both non-NASA channels and by NASA in the NASA STI Report Series, which includes the following report types:

- TECHNICAL PUBLICATION. Reports of completed research or a major significant phase of research that present the results of NASA programs and include extensive data or theoretical analysis. Includes compilations of significant scientific and technical data and information deemed to be of continuing reference value. NASA counter-part of peer-reviewed formal professional papers, but has less stringent limitations on manuscript length and extent of graphic presentations.

- TECHNICAL MEMORANDUM. Scientific and technical findings that are preliminary or of specialized interest, e.g., "quick-release" reports, working papers, and bibliographies that contain minimal annotation. Does not contain extensive analysis.

- CONTRACTOR REPORT. Scientific and technical findings by NASA-sponsored contractors and grantees.

- CONFERENCE PUBLICATION. Collected papers from scientific and technical conferences, symposia, seminars, or other meetings sponsored or co-sponsored by NASA.

- SPECIAL PUBLICATION. Scientific, technical, or historical information from NASA programs, projects, and missions, often concerned with subjects having substantial public interest.

- TECHNICAL TRANSLATION. English-language translations of foreign scientific and technical material pertinent to NASA's mission.

For more information about the NASA STI program, see the following:

- Access the NASA STI program home page at http://www.sti.nasa.gov

- E-mail your question to help@sti.nasa.gov

- Fax your question to the NASA STI Information Desk at 757-864-6500

- Telephone the NASA STI Information Desk at 757-864-9658

- Write to:
  NASA STI Program
  Mail Stop 148
  NASA Langley Research Center
  Hampton, VA 23681-2199

NASA/TM—2017-219071

Airborne Hyperspectral Sensing of Harmful Algal Blooms in the Great Lakes Region: System Calibration and Validation

From Photons to Algae Information: The Processes In-Between

John Lekki
Glenn Research Center, Cleveland, Ohio

Robert Anderson
Glenn Research Center, Cleveland, Ohio

Dulcinea Avouris
Kent State University, Kent, Ohio

Richard Becker
University of Toledo, Toledo, Ohio

James Churnside
NOAA Earth System Research Lab, Boulder, Colorado

Michael Cline
University of Toledo, Toledo, Ohio

James Demers
Glenn Research Center, Cleveland, Ohio

George Leshkevich
NOAA Great Lakes Environmental Research Lab, Ann Arbor, Michigan

Larry Liou
Glenn Research Center, Cleveland, Ohio

Jeffrey Luvall
NASA Marshall Space Flight Center, Huntsville, Alabama

Joseph Ortiz
Kent State University, Kent, Ohio

Anthony Royce
Glenn Research Center, Cleveland, Ohio

Steve Ruberg
NOAA Great Lakes Environmental Research Lab, Ann Arbor, Michigan

Reid Sawtell
Michigan Technological Research Institute, Ann Arbor, Michigan

Michael Sayers
Michigan Technological Research Institute, Ann Arbor, Michigan

Stephen Schiller
South Dakota State University, Brookings, South Dakota

Robert Shuchman
Michigan Technological Research Institute, Ann Arbor, Michigan

Anita Simic
Bowling Green State University, Bowling Green, Ohio

Dack Stuart
University of Michigan, Ann Arbor, Michigan

Glenn Sullivan
Michigan Technological Research Institute, Ann Arbor, Michigan

Paul Tavernelli
Glenn Research Center, Cleveland, Ohio

Roger Tokars
Glenn Research Center, Cleveland, Ohio

Andrea Vander Woude
University of Michigan, Ann Arbor, Michigan

National Aeronautics and
Space Administration

Glenn Research Center
Cleveland, Ohio 44135

February 2017

Available from

NASA STI Program
Mail Stop 148
NASA Langley Research Center
Hampton, VA 23681-2199

National Technical Information Service
5285 Port Royal Road
Springfield, VA 22161
703-605-6000

This report is available in electronic form at http://www.sti.nasa.gov/ and http://ntrs.nasa.gov/

Contents

Airborne Hyperspectral Sensing of Harmful Algal Blooms in Great Lakes Region: System Calibration and Validation

From Photons to Algal Information: The Processes In-Between

John Lekki
National Aeronautics and Space Administration
Glenn Research Center
Cleveland, Ohio 44135

Robert Anderson
National Aeronautics and Space Administration
Glenn Research Center
Cleveland, Ohio 44135

Dulcinea Avouris
Kent State University
Kent, Ohio 44240

Richard Becker
University of Toledo
Toledo, Ohio 43606

James Churnside
NOAA Earth System Research Lab
Boulder, Colorado 80305

Michael Cline
University of Toledo
Toledo, Ohio 43606

James Demers
National Aeronautics and Space Administration
Glenn Research Center
Cleveland, Ohio 44135

George Leshkevich
NOAA Great Lakes Environmental Research Lab
Ann Arbor, Michigan 48108

Larry Liou
National Aeronautics and Space Administration
Glenn Research Center
Cleveland, Ohio 44135

Jeffrey Luvall
NASA Marshall Space Flight Center
Huntsville, Alabama 35812

Joseph Ortiz
Kent State University
Kent, Ohio 44240

Anthony Royce
National Aeronautics and Space Administration
Glenn Research Center
Cleveland, Ohio 44135

Steve Ruberg
NOAA Great Lakes Environmental Research Lab
Ann Arbor, Michigan 48108

Reid Sawtell
Michigan Technological Research Institute
Ann Arbor, Michigan 48105

Michael Sayers
Michigan Technological Research Institute
Ann Arbor, Michigan 48105

Stephen Schiller
South Dakota State University
Brookings, South Dakota 57007

Robert Shuchman
Michigan Technological Research Institute
Ann Arbor, Michigan 48105

Anita Simic
Bowling Green State University
Bowling Green, Ohio 43403

Dack Stuart
University of Michigan
Ann Arbor, Michigan 48108

Glenn Sullivan
Michigan Technological Research Institute
Ann Arbor, Michigan 48105

Paul Tavernelli
National Aeronautics and Space Administration
Glenn Research Center
Cleveland, Ohio 44135

Roger Tokars
NASA Glenn Research Center
Cleveland, Ohio 44135

Andrea Vander Woude
University of Michigan
Ann Arbor, Michigan 48108

Summary

Harmful algal blooms (HABs) in Lake Erie have been prominent in recent years. The bloom in 2014 reached a severe level causing the State of Ohio to declare a state of emergency. At that time NASA Glenn Research Center was requested by stakeholders to help monitor the blooms in Lake Erie.

Glenn conducted flights twice a week in August and September and assembled and distributed the HAB information to the shoreline water resource managers using its hyperspectral imaging sensor (in development since 2006), the S–3 Viking aircraft, and funding resources from the NASA Headquarters Earth Science Division.

Since then, the State of Ohio, National Oceanic and Atmospheric Administration (NOAA), and U.S. Environmental Protection Agency (EPA) have elevated their funding and activities for observing, monitoring, and addressing the root cause of HABs. Also, the communities and stakeholders have persistently requested NASA Glenn's participation in HAB observation. Abundant field campaigns and sample analyses have been funded by Ohio and NOAA, which provided a great opportunity for NASA to advance science and airborne hyperspectral remote sensing economically.

Capitalizing on this opportunity to advance the science of algal blooms and remote sensing, NASA Glenn conducted the Airborne Hyperspectral Observation of harmful algal blooms campaign in 2015 that was, in many respects, twice as large as the 2014 campaign. Focusing mostly on Lake Erie, but also including other small inland lakes and the Ohio River, the campaign was conducted in partnership with a large number of partners specializing in marine science and remote sensing.

Airborne hyperspectral observation of HABs holds promise to distinguish potential HABs from nuisance blooms, determine their concentrations, and delineate their movement in an augmented spatial and temporal resolution and under clouds—all of which are excellent complements to satellite observations.

Working with collaborators at several Ohio and Michigan institutions as well as one in South Dakota and one in Alabama, this effort was able to provide next-day georeferenced estimates of cyanobacteria and scum concentrations. Very prompt processing and analysis of the hyperspectral imagery is necessary for the information to be acted upon. For example, a next-day report of an overflight over the Ohio River indicated that a bloom could be present as far downstream as the Cincinnati intake, but the Ohio EPA had not received visual reports of a bloom that far downstream. Water samples were obtained at the Cincinnati water intake, based on the flight data, and detected microcystins in the source water. The flight data helped State and municipal authorities realize the potential extent of that bloom, and triggered response sampling, before the visual river-wide scums started forming.

The present document describes the process that was utilized to take raw remote sensing data and create information products; this includes system calibration and validation, efforts to correct atmospheric effects, and algorithms that produce the data products. Furthermore, successful research into improved algorithms for expanding the capability to delineate in water constituents is included. Finally, comparisons that show expected relationships between ground-based measurements and hyperspectral imager version 2 (HSI2) data results are presented, giving confidence in the remote sensing products.

1.0 Introduction

Harmful algal blooms (HABs) are a growing concern worldwide (Turpie et al., 2016; Bullerjahn et al., 2016). The Great Lakes provide drinking water and recreational opportunities for about 40 million people and are home to some of the most productive freshwater commercial and recreational fisheries in the world. HABs negatively impact all of these uses. Understanding bloom dynamics depends on accurate and frequent measurements of bloom type, size, and density. Accurate determinations of bloom extents and year-to-year variations help to identify factors that affect a bloom, including possible triggering events. These measurements are best made by remote sensing, and several advancements have been made in using satellite data to determine bloom biomass (Richardson, 1996; Sayers et al., 2016).

The susceptibility of the Great Lakes to HABs is of particular concern because the lakes are strategically located between the United States and Canada and because they supply drinking water for p. 2millions of people. Toxic algal blooms have been occurring more frequently throughout the world in recent years, and human health has been impacted by algal toxins for some time (Anderson, 2004; Backer and McGillicuddy, 2006; Falconer, 1999; Hallegraeff, 1993). Enhanced methods to improve monitoring are needed, particularly because there is the potential for HABs in the Great Lakes to increase in severity in response to climate change (Turpie et al., 2016; Ortiz, Schiller, and Luvall, 2015; Bullerjahn et al., 2016). The species Microcystis aeruginosa commonly produces the toxin microcystin. This toxin damages the liver in humans and wildlife and is a concern in drinking water and during recreational activity where blooms are present. Also, it may even accumulate in fish (Butler et al. 2009). Algal blooms can also result in hypoxic conditions which cause large fish kills. Summer blooms of the cyanobacterium Microcystis in Lake Erie produce levels of algal toxins that exceed limits set by the World Health Organization (e.g., Rinta-Kanto et al., 2005) and force municipal water utilities to spend up to $14,000/day in additional filtration costs to ensure a safe water supply. The Great Lakes provide one of the world's most productive freshwater fisheries, with the economic contribution of their commercial and recreational activities estimated to be at least $7 billion. Successfully identifying and mitigating the causes of blooms will support employment in the charter fishing, commercial fishing, and tourist industries.

In summer of 2014, as the NASA Glenn Research Center harmful algal bloom remote sensing team continued its small-scale research of applying the hyperspectral imaging instrument to monitor the HABs in waters, Lake Erie's algal bloom grew and intensified in late July to the point where a state of emergency was declared by Ohio in order to address the drinking water source problem for the 500,000 people in the Toledo area. This emergency prompted the Glenn Center Director to order the team to conduct biweekly flights using the hyperspectral instrument to help monitor the intensity and spread of the harmful algae in Lake Erie.

Responding, the project team adapted to conduct a high-priority and high-visibility flight mission performing twice weekly operational flights to monitor the algae growth in Lake Erie. Flight expenses were supported by the NASA Earth Science Division while Glenn engaged other government and academic team members and their assets such as watercraft and aircraft to jointly conduct a comprehensive air and ground campaign.

The flights generated algae bloom data that were provided to the Ohio water intake managers. As a result, the Ohio Environmental Protection Agency (Ohio EPA) and other shoreline water resource managers received algae bloom information supplied by the NASA Glenn team to help them make decisions impacting the public. These regional water resource managers wrote emails afterwards to express gratitude to NASA. Subsequent collaborations were formed, such as the 2015 Ohio/NASA task force on HABs. HAB information provided by remote sensing and water sampling helped provide for early warning to ensure proper water treatment and shutoff avoidance.

The 2014 emergency project inspired a more thoughtfully planned mission in 2015, which offered augmented benefits by partnering and capitalizing on surged interest and resource allocation on both Federal and regional levels.

In 2015, the National Oceanic and Atmospheric Administration (NOAA) and State of Ohio invested more in HAB monitoring and studies, and they partnered with NASA in using airborne hyperspectral method to monitor algal blooms. The Glenn project team was able to continue developing remote sensing methods for accurately monitoring the health-threatening HABs in the inland waters.

The partners for this research and monitoring activity in summer 2015 were NOAA, State of Ohio, U.S. EPA, Air Force Research Laboratory (AFRL), Kent State University (KSU), University of Toledo (UT), Michigan Technological University Research Institute (MTRI), South Dakota State University (SDSU), Bowling Green State University (BGSU), University of Cincinnati, Ohio State University (OSU), Ohio Aerospace Institute (OAI), University of Michigan Cooperative Institute for Limnology and Ecosystems Research (UofM CILER), and NASA Marshall Space Flight Center.

1.1 Hyperspectral Imaging System

Glenn's hyperspectral imaging concept was developed in fiscal year 2006 (FY06) and has been flown in three separate aircraft campaigns to study HABs with the NOAA Great Lakes Environmental Research Laboratory (GLERL) (Lekki et al., 2009). The hyperspectral imager (HSI2) is shown in Figure 1.1.

One key feature of the Glenn HSI2 is a modular design that permits mission flexibility and ease in upgrade. The front optic is designed as a standard C-mount mechanical interface, permitting front-optic swaps to modify the field-of-view (FOV), signal-to-noise ratio (SNR), and integration time. Also, the modular imager-mount allows the imager and final-imager lens to be inserted as a unit, enabling easy modification of image size and hence, spatial resolution. A list of the specifications of the imager is provided in Table 1.1.

The airborne HSI2 has been developed in-house at NASA Glenn Research Center. This pushbroom imager collects three-dimensional (3D) hyperspectral data in the 400 to 900 nm wavelength range, which is ideal for harmful algae identification. The spatial resolution can be adjusted by flying at different altitudes and speeds. The image swath can also be adjusted by changing the FOV lens from 32° to 12°.

Additional airborne instrumentation includes a spectroradiometer mounted inside the aircraft and directed above to collect downwelling irradiance from the Sun from 400 to 950 nm. Ground researchers use a similar instrument as this flies over in order to capture the difference in the irradiance caused by atmospheric affects. The final major instrument is an inertial navigation system (INS) to collect Global Positioning System (GPS) and attitude information. These data are used to georeference hyperspectral data.

Figure 1.1—Glenn hyperspectral imager.

TABLE 1.1.—TYPICAL SPECIFICATIONS FOR GLENN HSI2

Wavelength range, nm	400 to 900
Optical spectral resolution (full width half maximum, FWHM), nm	2.5
Spectral sampling resolution, nm	1
Optical throughput	f/2.0
Signal-to-noise ratio at 532 nm at 3.5 percent albedo (water)	1000:1
Digitization bit depth	14 bit
Spatial resolution perpendicular to travel direction (12 mm lens)	1 m at 0.45 km altitude
Maximum spatial resolution along travel direction (imaging rate limited)	1 m
Field of view (FOV)	12.4°
FOV can be changed by replacing front optic, which decreases perpendicular spatial resolution at 0.45 km altitude	258 m
Imaging rate	25 frames per sec
System mass	3.7 kg (excludes CPU)
Volume	12 by 15 by 18 cm
Power consumption	35 W

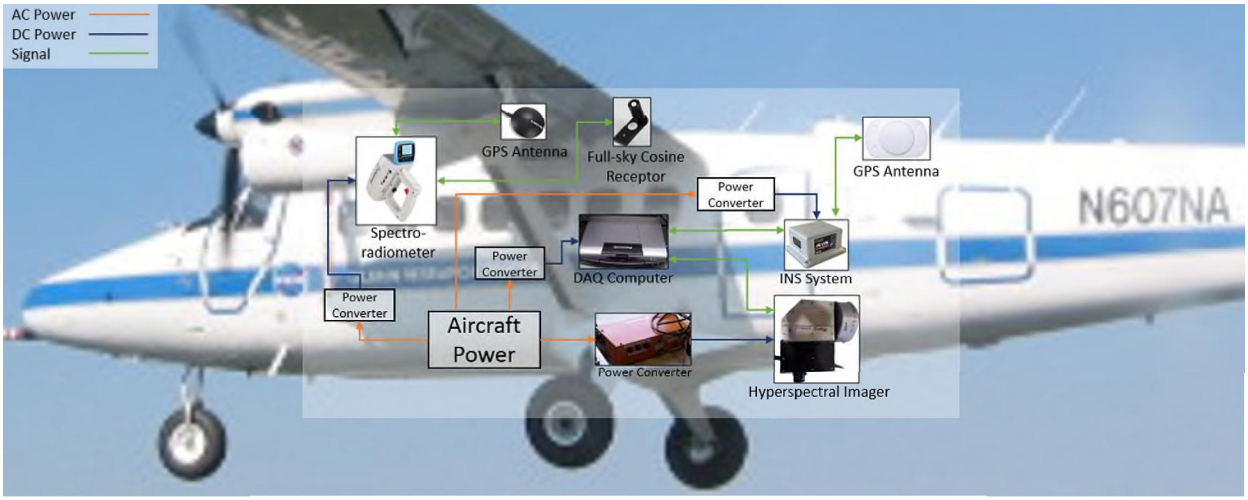

Figure 1.2.—Schematic of hyperspectral imaging system and Twin Otter aircraft.

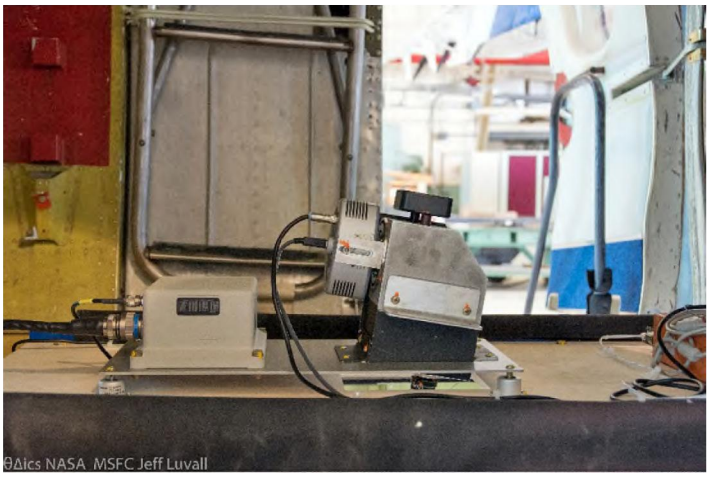

Figure 1.3.—Imager and inertial navigation system mounted in Twin Otter aircraft.

The HSI2 system was installed and operated on the Twin Otter aircraft (Fig. 1.2). The Twin Otter is a NASA aircraft operated out of the NASA Glenn Hangar. The Twin Otter is propeller driven and thus much slower than the jet-propelled S3 used in 2014. Because it can be flown slower, the ground footprint for each pixel is closer to a square, where it is longer in the direction of travel than it is orthogonal to the direction of travel. For the remounting of the instrument in the Twin Otter, the imaging system and the INS were attached to the same platform shown in Figure 1.3, which resulted in more stable and consistent data.

1.2 Data Processing and Handling Overview

Data processing is handled in a way that is timely, automated, and effective at turning raw collected data into something relevant to the end user, such as a researcher, municipal water treatment plant operator, or park department with affected beaches. During data collection, the HSI2 system collects pixel intensity counts that are stored in a matrix. The HSI2 operator may observe this matrix in real time as a "waterfall" image of the area being scanned in order to verify that the system is operating as expected. Data recorded during each flight is produced by two systems: the HSI2 control and acquisition computer and the spectroradiometer system. HSI2 data is recorded as multiple two-dimensional (2D) images where one dimension is spectral information and the other is spatial information. Spectroradiometer data are

recorded as downwelling irradiance spectra acquired two per minute. The postprocessing of data utilizes autonomous scripts. The scripts read in the data and convert the pixel intensities into radiance values as determined by a radiance calibration. The location of each pixel radiance is then assigned to a wavelength as determined by the wavelength calibration. These wavelengths make up the spectral axis of each 2D image. The spatial axis is along the optical imaging plane and must be georeferenced to a latitude and longitude location as projected onto the surface of the scanned area. Using the GPS and attitude information that is time tagged and matched with the imager, a georeferencing algorithm processes the data into the correct location. Known geographical locations are typically used along the ground to verify the algorithm accurately georeferences the imagery. The end product is a mapped data set that has a spectral profile for each location. The spectral profile must then be adjusted using downwelling irradiance measurements at both the aircraft and on the ground in order to compensate for atmospheric affects. Data processing work flow is depicted in the flowchart in Figure 1.4.

Data is processed to the following levels:

- Level 0: raw spectral and aircraft attitude data (time stamped) (file format: HDB)
- Level 1: spectral radiance, georeferenced, no atmospheric correction (HDF)
- Level 2: georeferenced data with atmospheric correction (HDF) (not a daily product)
- Level 3: Same as Level 2, but data spectrally binned to 5-nm resolution, which matches the other field instruments (HDF) (not a daily product)

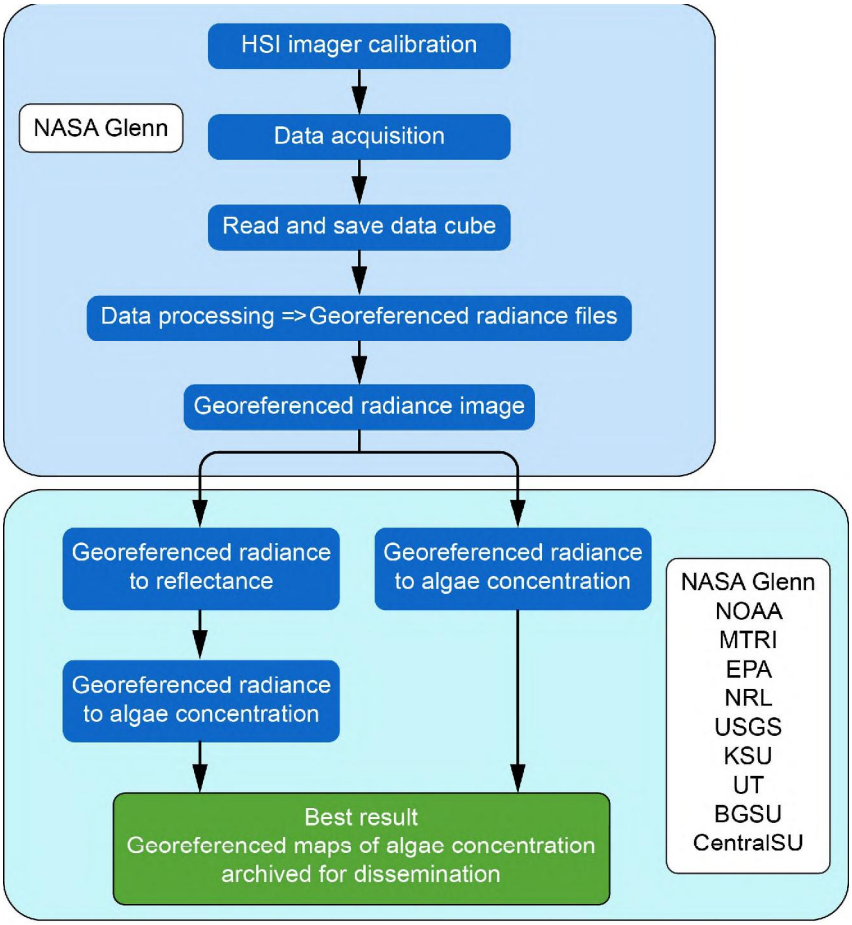

Figure 1.4.—Data processing flowchart.

Flight and ground data are transferred to and stored on the State of Ohio's enterprise data system for environmental data collection and processing. The system rides on the backbone of Ohio's research infrastructure. The operational characteristics of the system are

- The network utilizes OARNet connectivity, which is Ohio's high-speed network connecting all of Ohio's universities and colleges to centralized processing, storage, and administration services. This network also connects NASA and AFRL.
- Ohio's Supercomputing Center provides the storage and processing infrastructure backbone. The warehouse will consist of seven nodes with 4 TB storage, 16 GB RAM, and 3.7-GHz processors.

Upgrades to this system are currently being addressed. However, a backup option for data storage, sharing, and archiving has also been coordinated. This backup server location is at Miami University, Oxford, Ohio, and the coordinating organization is OhioView.

1.3 Hyperspectral Flight Data

Data recorded during each flight is produced by two systems: the HSI2 control and acquisition computer and the spectroradiometer system. In 2015, for each imaging flight over a point of interest, the raw output of the hyperspectral data acquisition computer is a binary file. Each file (sometimes referred to as a track) contains a number of hyperspectral image frames (data is in raw counts). These data files also contain a set of parameter values for each frame, including exposure time, sensor temperature, gain, GPS time, latitude, longitude, altitude, GPS fix type, orient tick, roll, pitch, and yaw. Of course, each frame also includes an image. The image size is 658 by 496 pixels. The 658-pixel dimension is the spectral dimension and the shorter dimension corresponds to a line of 496 pixels on the ground.

During flights in 2015, a set of irradiance spectra from an upward-looking spectroradiometer was acquired during every flight. The radiometer data is stored as sets of spectra acquired in 30-s time intervals, each with a time stamp and GPS coordinates among other ancillary data.

The HSI2 imaging system includes the imager, the INS, and an upward-looking spectroradiometer. The imager and the INS acquire data at 25 Hz and the radiometer at 0.033 Hz. The imager is not synchronized so we use the imager frame times as a basis and interpolate the INS and radiometer data to estimate data values corresponding to the imager frame times.

2.0 HSI2 Calibration and Data Preprocessing

The calibration of the Glenn HSI2 takes place in the Glenn Optical Laboratory. One of the tools of this this lab includes a National Institute of Standards and Technology (NIST) traceable Labsphere incandescent light source that is calibrated for a known radiance output as a function of wavelength. Another calibration tool is the mercury argon light source, which provides spectral peaks at known wavelengths and is used to calibrate the image pixels to specific wavelengths. Prior to flight, the wavelength associated with each of the 658-wavelength pixels must be determined. The viewing angle associated with each of the 496-line image pixels must also be measured so we can accurately project the line to the ground, and finally the conversion from image intensity (counts) to radiance must be measured. Once the data have been converted to radiance and georeferenced, it is transmitted to the Ohio Supercomputer Center where it is archived and is accessible to the entire research team.

2.1 Wavelength Calibration

To determine the wavelength associated with each pixel there are two options: (1) use a Hg-Ar calibration lamp or (2) use the solar "G" line and the oxygen absorption line as anchor wavelengths. To use the Hg-Ar calibration lamp, the imager is set on a table and the calibration lamp is moved back and forth in front of it so that all image lines are illuminated. In Figure 2.1 the black plot is the averaged data

from 200 frames of HSI2 data using the Hg-Ar lamp. The blue dots are wavelengths from a list of the wavelengths where significant peaks occur in the output of the Hg-Ar lamp. Using the pixel values from the data peaks and the wavelengths from the blue dots an equation for wavelength is derived as a function of pixel value: *Wavelength* = 0.989 × *pixel* + 320, where *pixel* values range from 0 to 657. The wavelength range in Figure 2.1 has been limited to range between 400 and 900 nm since the imager sensitivity falls off outside of that range.

2.1.1 Search for Wavelength Truth

For validation of the wavelength scale using HSI2 flight data spectra, two consistent wavelength anchors available at opposite ends of the range are used: the solar "G" line at 431 nm and the oxygen absorption line at 760 nm. Using the wavelength equation, the pixel values for the two anchors are found to be pixel 112 for 431 nm and pixel 445 for 760 nm.

However, there is a problem: The wavelength-versus-pixel relation is different in the flight data than it is in the laboratory using the Hg/Ar lamp. Figure 2.2 shows a typical raw data spectrum (solid black line) from the HSI2 instrument. The green lines are drawn where the anchor wavelengths should be based on the spectrum shape. Using the equation from the Hg-Ar calibration, the two anchor wavelengths (431 and 760 nm) are plotted in red. It would appear that the wavelength scale has shifted slightly. The current thinking is that this shift is a result of very slight mechanical shifts in the imager geometry due to changes in temperature as the aircraft moves up and down in the air column.

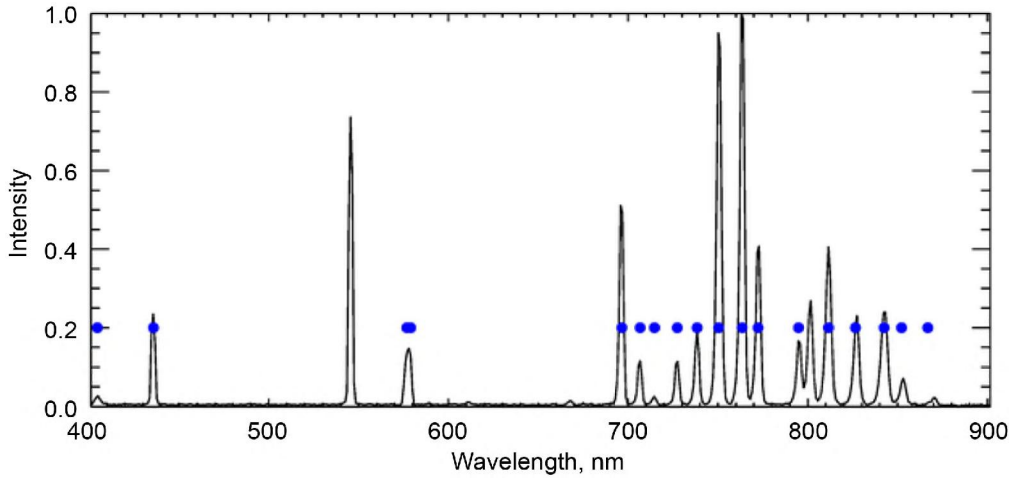

Figure 2.1.—Wavelength calibration.

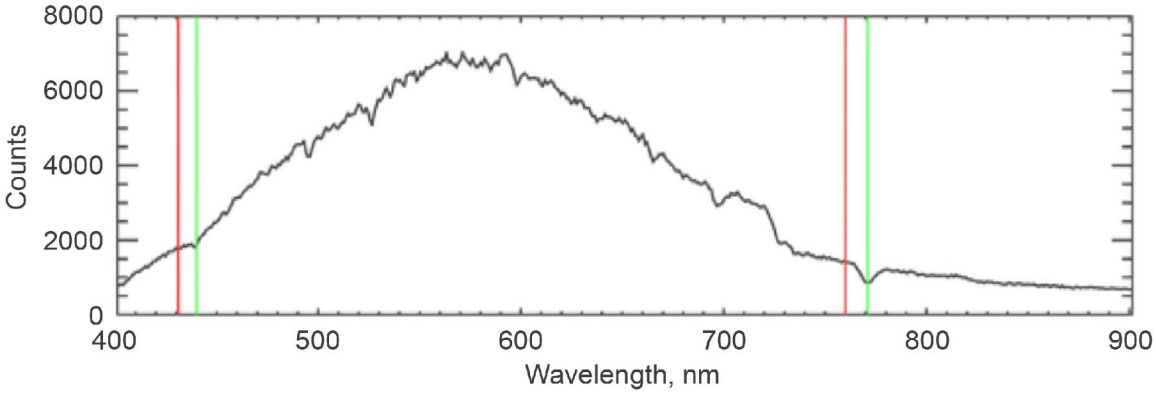

Figure 2.2.—Sample HSI2 spectrum. Red lines are anchor positions from equation *Wavelength* = 0.989 × *pixel* + 320; green lines are where anchors should be.

2.1.2 Wavelength Binning

The wavelength scale must be rebinned to reduce the size of the processed files and to satisfy requirements imposed by some HAB detection algorithms. The current pixel-to-pixel change in wavelength is 0.989 nm. Typically the wavelength is rebinned by a factor of 3, decreasing the resolution to 2.97 nm per pixel. The rebinning is done with the raw data before the radiance calibration has been applied.

Figures 2.3 and 2.4 show plots of the HSI2 calibration spectrum with the wavelength scale rebinned by factors of 3 and 5, respectively. As we decrease the spectral resolution, the peak locations become more difficult to determine.

2.2 HSI2 View Angle

The georeferencing process requires knowledge of the imager viewing angle. The viewing angle is defined as that angle relative to the imaging axis beyond which the image cuts off. For the imager described here, the view angle was determined by setting up the imager in the laboratory at some distance from a white background. The image was monitored by moving a dark object, such as an optical beam stop, back and forth in front of the imager. The location was recorded where the image cut off at the image axis's two extremes. Using trigonometry, the imager viewing angle can be calculated. The full view angle for the 2015 airborne campaign was determined to be 12.4°. The accuracy of georeferencing has been used as a validation of this view angle determination.

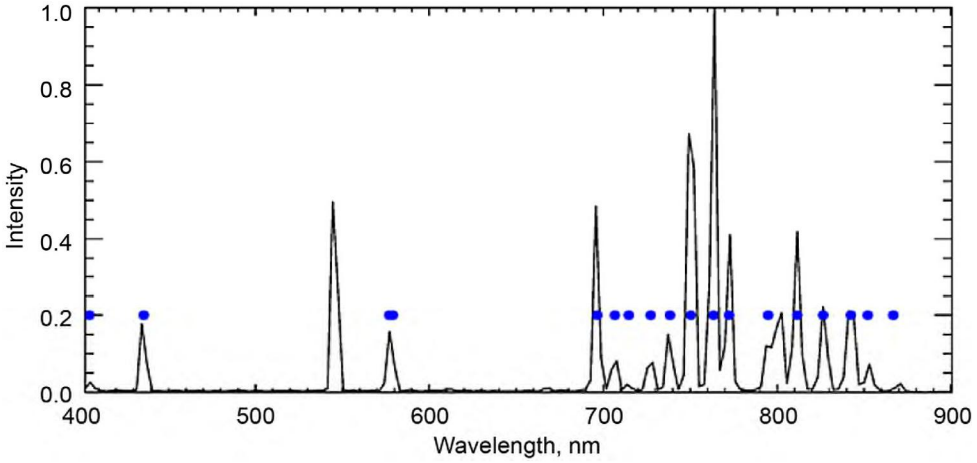

Figure 2.3.—Calibration spectrum rebinned by factor of 3.

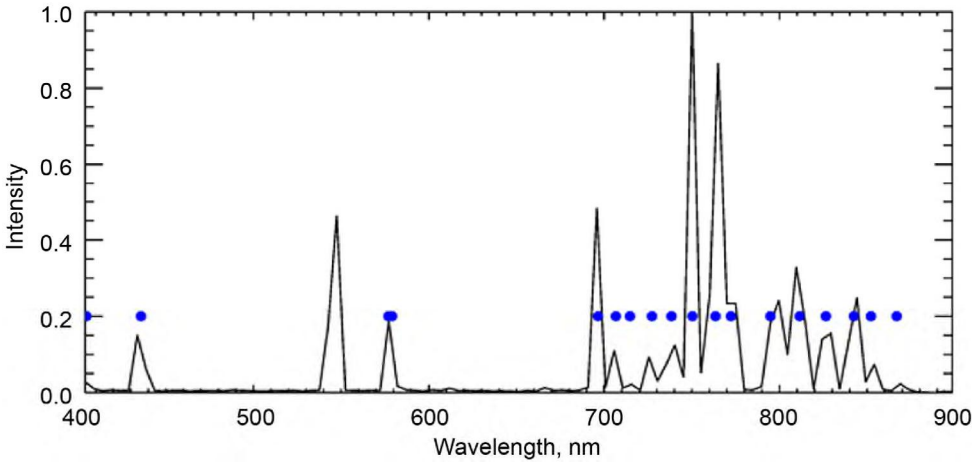

Figure 2.4.—Calibration spectrum rebinned by factor of 5.

2.3 Converting to Radiance

For the data from each track (flight segment over region of interest), laboratory calibration files were used to convert the raw counts in the image files to units of radiance ($W/m^2 \cdot sr \cdot nm$). In 2015 the calibration data was acquired using a recently rebuilt and recalibrated (with NIST traceability) LabSphere integrating sphere. With the integrating sphere illumination control set to produce a known radiance-versus-wavelength profile, a set of frames was acquired with the HSI2 system. Figure 2.5 is a surface plot of the radiance profile from the integrating sphere based on vendor-certified calibration data. Figure 2.6 shows a carpet plot of a single frame from the HSI2 imager of this radiance profile.

The goal is to derive an image that has units of radiance per image intensity count. This image is developed by dividing the known integrating sphere radiance profile by the HSI2 image, subtracting a dark current image from the HSI2 image before this operation. The plot in Figure 2.7 shows the radiance-per-count image. To convert data in an HSI2 track to radiance, each frame in the track must be multiplied by the radiance-per-count image shown in Figure 2.7.

When applying the radiance-per-count image, a perfect pixel-to-pixel match is assumed between the radiance-per-count image generated in the laboratory and the in-flight data image. This is frequently not the case with data acquired while airborne. Recall that the HSI2 images have two axes: the wavelength axis and the distance axis. There is evidence that a shift occurs in the airborne data along both axes and that the shift may be different for each axis. To correct this problem, the calibration image must be shifted before it is applied to the data, and to do that the optimum shift along these two axes must be determined. The solar "G" line and the O_2 absorption line can be used to determine the wavelength shift as discussed earlier (Sec. 2.1.1, Search for Wavelength Truth). The wavelength axis can be stretched and/or translated so that these two spectral features occur at the proper wavelengths in the data image.

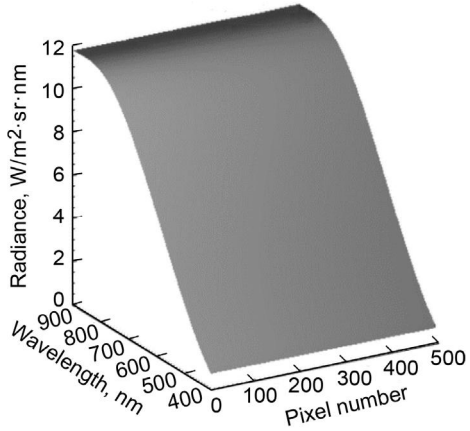

Figure 2.5.—Radiance profile from integrating sphere.

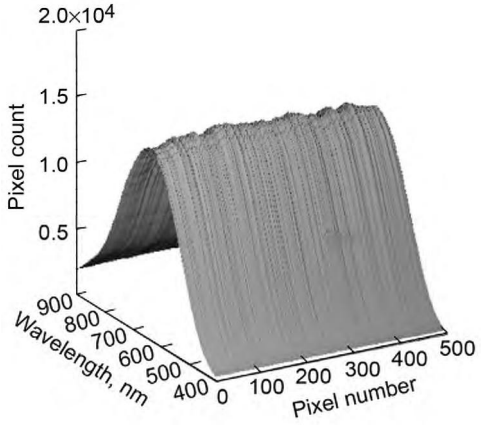

Figure 2.6.—Image from HSI2 of integrating sphere.

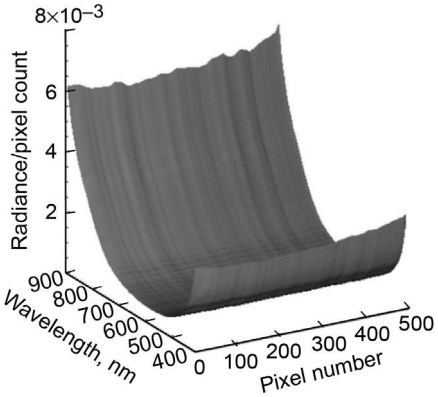

Figure 2.7.—Radiance- ($W/m^2 \cdot sr \cdot nm$) per-image pixel count.

When there is a shift along the distance axis the result is striping, caused by the optical system, that appear when the frames are stacked and the result is displayed. Figure 2.8 shows an example. This is data that includes Maumee Bay State Park (MBSP) beach near Toledo, Ohio, and the nearby inland lake. The image has been georeferenced, and for this image appropriate wavelength bands were chosen for the red, green, and blue image components. When a section of the image includes all water, the stripes are readily seen as in the right side of Figure 2.8.

If the radiance-per-count image is shifted slightly along the distance axis (vertical axis in Figs. 2.8 and 2.9) before applying it to the data, the striping is minimized. Figure 2.9 shows this same image where a shift has been applied. The stripes are not nearly so pronounced.

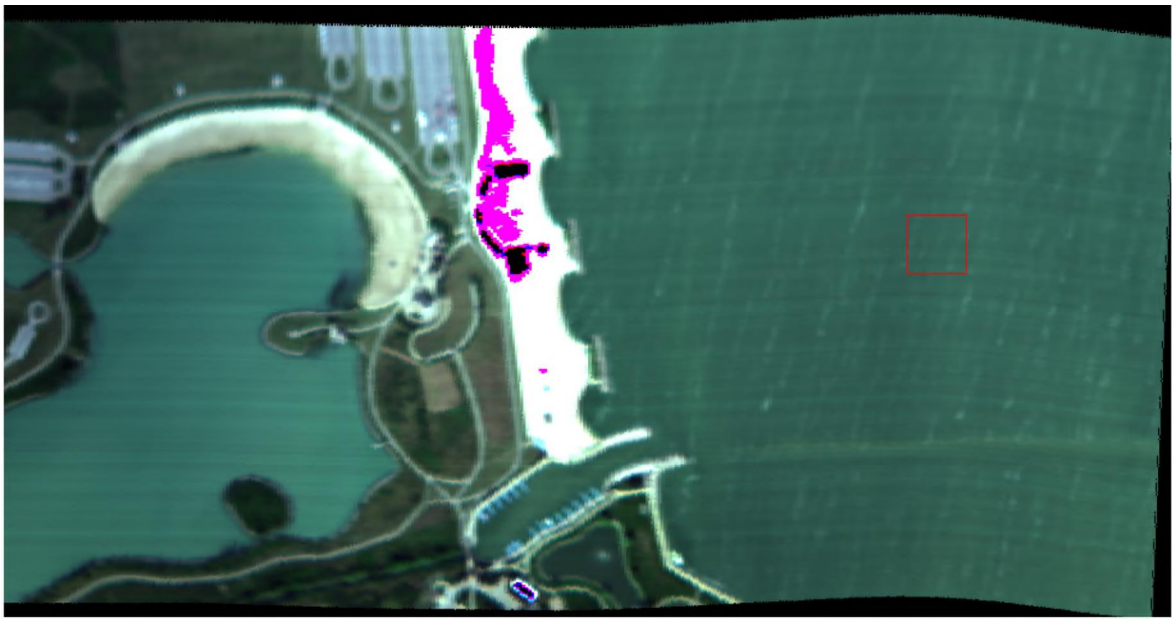

Figure 2.8.—Example hyperspectral image showing misregistration striping.

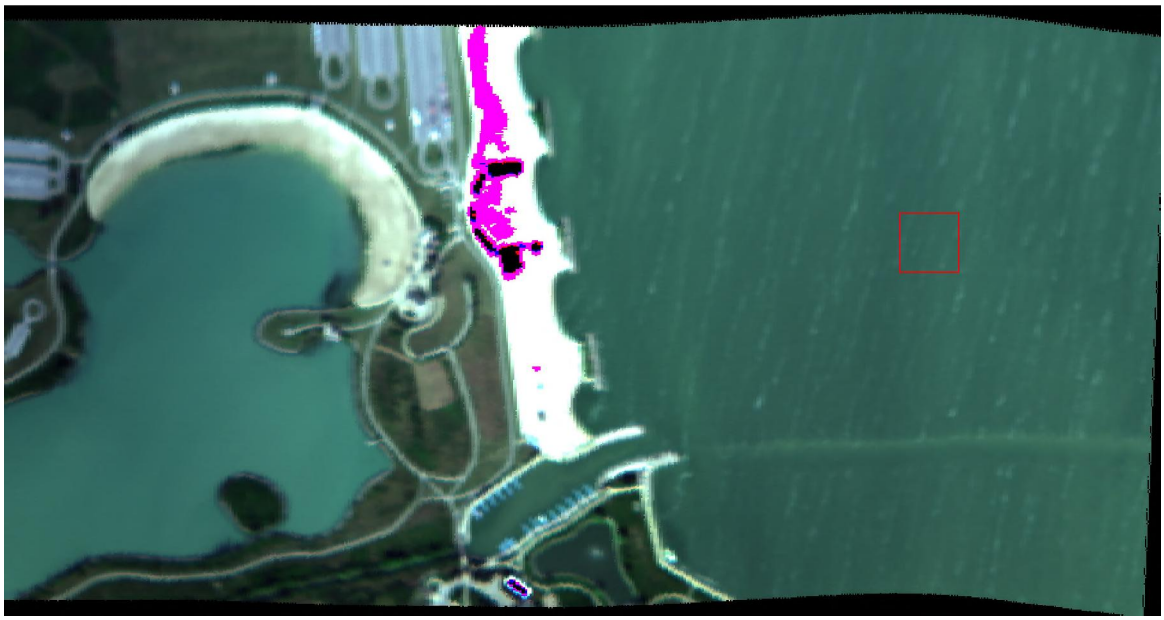

Figure 2.9.—Example hyperspectral image with corrected misregistration.

The challenge is to program the processing computer to figure out the optimum shift. If a segment of a track is over water across the whole track, a correlation process can determine the optimum shift. A cross-correlation is calculated between the data image and the shifted radiance-per-count image for various shift amounts. The optimum shift should be the shift that produces maximum cross-correlation. Unfortunately, this correlation technique only works well when the track is entirely over water.

How can the computer be programmed to find water? If the HSI2 is imaging water, the signal variation for that line will likely be much less than it would be if the line included land as well as water. Thus, one way to find those lines acquired over water is to look for lines with relatively low signal variation. A commonly used indicator of signal variability is the standard deviation. The standard deviation can be used to compute the standard deviation of the signal in a selected wavelength band for each image in an imaging track. To locate those image lines entirely over water, the software looks for the image lines resulting in the lowest standard deviation.

2.4 Georeferencing Process

Once the data has been converted to units of radiance with the optimum shifts applied, a set of GPS coordinates is computed for each pixel in the image track. For each frame in the track, a line is imaged on the surface of the Earth and the GPS coordinates are computed for each pixel in the line. It might be useful to think about the problem in reverse: Think of a line of 496 little lights whose beams are projected on the Earth surface as the plane overflies an area. The problem is to compute the GPS coordinates of the projected spots for each of the 496 pixels. This would be a relatively simple geometry problem if it could be assumed that the imager was always pointing down. Unfortunately the HSI2 unit is fixed to the airplane structure. So as the plane rolls (side to side), and pitches (nose up to nose down) and yaws (turns around a vertical axis), the HSI2 unit must follow.

Finding the GPS coordinates is thus essentially a ray-tracing process. The method used here attempts to trace a ray out from each pixel on the imager through the optical system and down to the surface.

2.4.1 Necessary Assumptions

In order to do this ray-tracing computation, some assumptions are made:

(1) Traveling out from the image sensor chip, the ray path to the front of the lens includes mirrors, a holographic grating, and then the lens. The rays are not followed through this maze, but are assumed to begin at the lens.

(2) A constant angle of view is assumed for the optical system. For the HSI2 system flown in 2015, the angle of view was measured in the lab to be 12.4°. The 496 imaging pixels are assumed to be spread linearly over this 12.4° angle. This amounts to an angle spacing between pixels of 0.025°.

(3) The above-ground-level elevation is also assumed to be constant. This is important because the GPS device provides altitude as altitude above sea level. To compute the actual distance to the surface from the aircraft, the ground elevation above sea level is subtracted from the GPS altitude. The constant elevation assumption is reasonable when flying over one of the Laurentian Great Lakes because the elevation is known and is essentially constant. The constant elevation assumption is violated when flying over land. There is currently no way of knowing the elevation before knowing the coordinates; the elevation information must be determined postflight. Thus, there is presently much more uncertainty in the geolocation over land.

With these assumptions and measurements of the image platform orientation, the coordinates of the imaged line on the surface can be computed. This georeferencing process was validated using known ground control points.

2.4.2 Projecting Imaging Line to Earth surface

An input geometry map (IGM) matrix must be generated to generate latitude and longitude values for each pixel in an HSI2 image. Starting with a pair of longitude latitude values for each image frame in the HSI2 image stack, the values are recorded by the HSI2 software and included with each image frame. As mentioned above, this process is essentially a ray-tracing operation.

Next follow a ray to the surface. As an example, choose the center pixel and assume that its ray is the same as the line along the imaging axis. Also assume that there is no roll, pitch, or yaw. This ray will hit the surface at the exact latitude and longitude being measured in the plane. Now suppose plane is rolled clockwise 2°. The projected spot will move to the left a distance equal to (altitude) × (tan2°). Combining the effects of roll with the effects of pitch and yaw yields a transformation matrix as follows: *Y*, *R*, and *P* are yaw, roll, and pitch, respectively:

$$M = \begin{bmatrix} \cos(Y)\cdot\cos(R) & -\cos(Y)\cdot\sin(R)\cdot\sin(P)-\sin(Y)\cdot\cos(P) & -\cos(Y)\cdot\sin(R)\cdot\cos(P)+\sin(Y)\cdot\sin(P) \\ \sin(Y)\cdot\cos(R) & -\sin(Y)\cdot\sin(R)\cdot\sin(P)+\cos(Y)\cdot\cos(P) & -\sin(Y)\cdot\sin(R)\cdot\cos(P)-\cos(Y)\cdot\sin(P) \\ \sin(R) & \cos(R)\cdot\sin(P) & \cos(R)\cdot\cos(P) \end{bmatrix}$$

It is assumed that the yaw value is degrees rotation clockwise from north (yaw = 0), that the nose-up angle from horizontal is positive pitch, and that roll measurement is positive clockwise from pilot view.

For each of the 496 pixels in the image line the view angle for that pixel and the above-ground distance as a starting point is used to iterate, using the transformation matrix, until intersecting the ground surface. This yields a distance north and distance east that is converted to a latitude and longitude increment to be added to the coordinates for that frame.

2.4.3 Georeferencing Using the Input Geometry Map

Since the plane may be pitching up and down and rolling during the data acquisition, it is very likely that the coordinates of pixels in one line image will overlap or sit on top of coordinates from another line image. Thus, the process of georeferencing of these images can be very complex. Fortunately, the software package used (IDL/ENVI, Exelis Visual Information Solutions. Inc.) provides this functionality. The georeferencing routine available computes a footprint using the envelope of all the GPS coordinates in the track. Then the software attempts to fill in the gaps with data pixels. To compute a radiance value for a pixel in a gap, the software looks for data pixels within a 7-pixel neighborhood around the gap pixel and sets the value of the gap pixel to the average of these neighborhood data pixels. For hyperspectral image pixels located on the same geographical location, the software uses a similar operation to determine the proper data level for that pixel.

2.4.4 Roll, Pitch, and Yaw Adjustments for Mounting Uncertainty

One other important assumption is that for each frame, there is an accurate measure of roll, pitch, and yaw at the instant of image acquisition. The 2015 campaign brought more confidence in the consistency of these parameter values.

The roll, pitch, and yaw angles are assumed to apply to the imaging axis. However, small adjustments to the roll, pitch, and yaw values are necessary to achieve optimum georeferencing results. These adjustments remain constant until the mounting configuration is changed.

Figure 2.10.—Hyperspectral image over Maumee Bay State Park, 2014. Copyright Google Earth.

2.4.5 Georeferencing Results

As described earlier, a longitude and latitude is generated for each pixel in a given track. These data are then used to produce a georeferenced data set. The software package used also provides a Google Earth Bridge functionality, which will create a ".kml" file that places the georeferenced image onto a satellite view of the Earth surface. Figure 2.10 is an example of "good" georeferencing from a track imaging the MBSP beach on September 17, 2014. The aqua line is the GPS track from the HSI2 INS system. The pseudo-color track is the georeferenced result. The side-to-side undulation results from correcting the track for the roll, pitch, and yaw values measured for this track. The color palette results from the choice of wavelength bands for the red, green, and blue contribution. Bands 146, 91, and 57 out of 170 (821, 660, and 560 nm, respectively) were used for this image. Water is blue and vegetation is red because vegetation reflects strongly in the near infrared (NIR).

2.5 Upward-Looking Spectroradiometer

During the 2015 HSI imaging campaign an ASD, Inc., FieldSpec® HandHeld 2 instrument was used to collect downwelling irradiance measurements in order to compute simple reflectance values from imager measurements. The spectroradiometer was mounted in the aircraft under a Plexiglas window because it was impractical to cut a suitable opening in the fuselage.

To determine the effect of the Plexiglas window on the radiometer measurements, irradiance measurements were collected outside the aircraft and then immediately inside the aircraft underneath the Plexiglas window. To avoid undesirable reflection errors, the aircraft was moved outside away from the hangar for this test. A hemispherical cosine collector was used on the instrument for these measurements.

Weather conditions were partly cloudy with mostly sun as shown in Figure 2.11. The ratio of the spectroradiometer measurement inside the aircraft to that outside is shown in Figure 2.12. Each dataset used to compute the ratio plotted in Figure 2.12 is an average of 20 spectroradiometer samples. Datasets were collected within 1 min of each other with a distance separation of about 7.4 m. Outside measurements were made so that the aircraft was beyond the viewing angle of the full-sky spectroradiometer measurement. The results show the transmission of the Plexiglas window for this particular sensor with this particular installation. The window in general reduces the irradiance measurement throughout the wavelength region of interest and attenuates almost completely below 400 nm.

Figure 2.11.—Sky image during radiometer test.

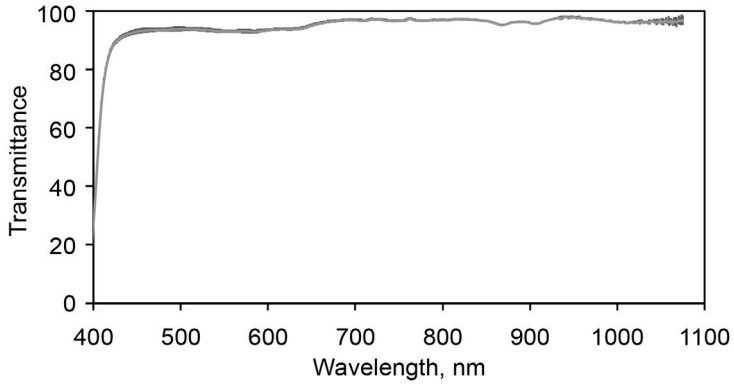

Figure 2.12.—Measured window transmittance showing effect of window on radiometer measurement.

2.6 At-Aircraft Reflectance

Reflectance measurements are desired for HABs assessment. A Cosine Receptor fore optic was attached to the upward-looking spectroradiometer by a fiber optic in order to directly measure the total full hemispherical solar irradiance. Figure 2.13 shows a comparison between the at-aircraft reflectance and the on-ground reflectance from the MBSP parking lot.

3.0 Atmospheric Correction

The atmospheric correction was determined from multiple comparisons of atmospheric corrections obtained using Tafkaa 6S, ATCOR 4 (ReSe Applications Schläpfer), and empirical line correction algorithms. Ryan et al. (2014) have previously shown that the atmosphere remover program ATREM (University of Colorado, 1999) corrections on orbital-based images performed well compared to on-water measurements made 2 days apart in a coastal ocean scenario, and we attempted to verify that these methods would work equally well in the sediment-rich waters of Lake Erie.

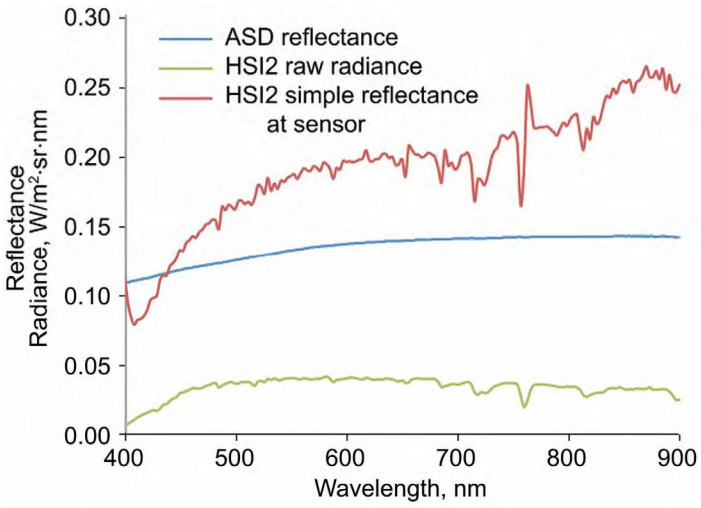

Figure 2.13.—HSI2 measurement of raw parking lot radiance over Maumee Bay State Park, compared with simultaneously acquired ground-measured reflectance from ASD, Inc., FieldSpec® 3 spectroradiometer (Aug. 11, 2015).

3.1 Atmospheric Correction Using the Empirical Line Method

When atmospherically correcting the remotely sensed HSI data, the most reliable method with the highest rate of success is the empirical line method (ELM). This entails the use of ground-target data in combination with the airborne HSI2 data. These corrections were done using the remote-sensing software ENVI. Two sample points were collected: one of the brightest spectra and one of the darkest. These ground target samples were obtained at MBSP, with the darkest samples taken on the black asphalt of the south parking lot, and the brightest samples taken on the white sand of the beach. As explained by Gao et al. (2009), this method involves using these bright and dark values to determine the gain and offset curves and then utilizing those curves in order to calculate the surface reflectance of the HSI2 data as a whole. This successfully eliminated many of the effects from atmospheric gasses affecting the relevant portion of the spectrum, including water vapor, carbon dioxide, and oxygen. Because of the use of phycocyanin's (the accessory pigment present in Mircrocystis cyanobacteria) specific spectral signature, it is crucial to remove this atmospheric noise because it tends to obscure these key spectral features in the wavelengths of interest.

The successful removal of atmospheric noise after applying the ELM is apparent when examining the reflectance spectra before and after the correction was applied. Figure 3.1 shows the successful correction of magnitude and shape at the park at the MBSP parking lot, and gives an indication in the lack of noise in the instrument. Figure 3.2 shows that previous to the atmospheric correction, characteristic peaks and troughs in the spectra appear smoothed and are indistinguishable. The spectral profile of the same site from the atmospherically corrected HSI2 image are also shown in those figures. From this comparison it is evident that atmospheric correction not only makes the characteristic peaks at 555 and 720 nm and troughs at 625 and 670 nm more distinguishable, but it also reduces the unwanted high reflectance in the UV, around 400 nm. This accurately resembles the reflectance commonly exhibited by water's surface (Morel, 1980) to a higher extent.

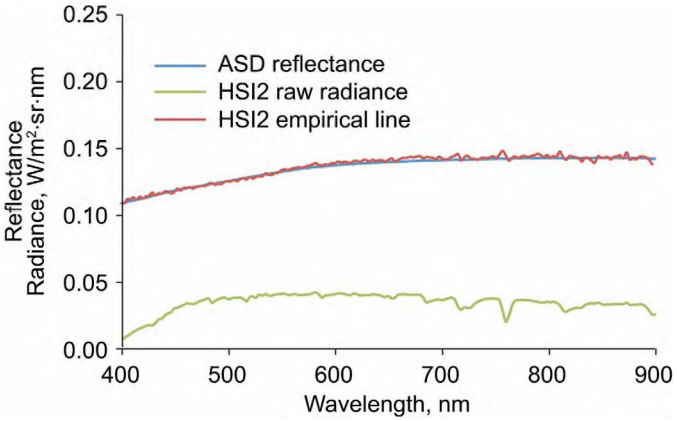

Figure 3.1.—Comparison of HSI2 raw parking lot radiance measured at ground height with the ASD, Inc., FieldSpec® 3 spectroradiometer and ELM-corrected HSI2 spectra of Maumee Bay State Park parking lot (Aug. 11, 2015).

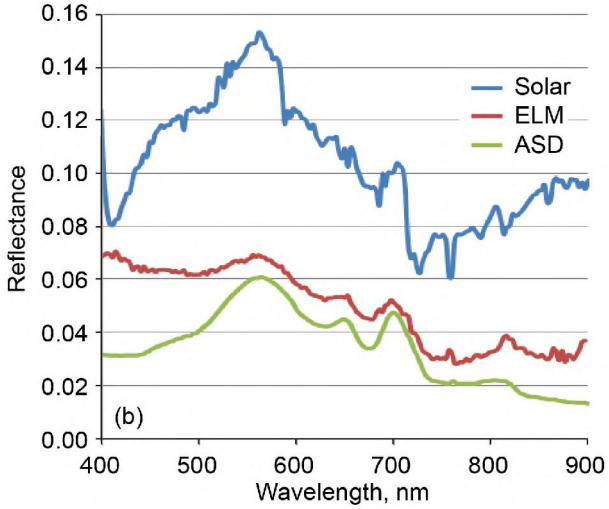

Figure 3.2.—Lake Erie reflectance, showing effect of correction on day with higher atmospheric contributions (site MB18 (see Fig. 3.5); Sept. 8, 2015), but not as homogeneous an atmosphere. Reflectance from HSI2 data calculated from downwelling irradiance at the sensor (Solar), HSI2 ELM-corrected data (ELM), and on-lake FieldSpec® 3 measurements (ASD) showing better agreement between ASD and ELM.

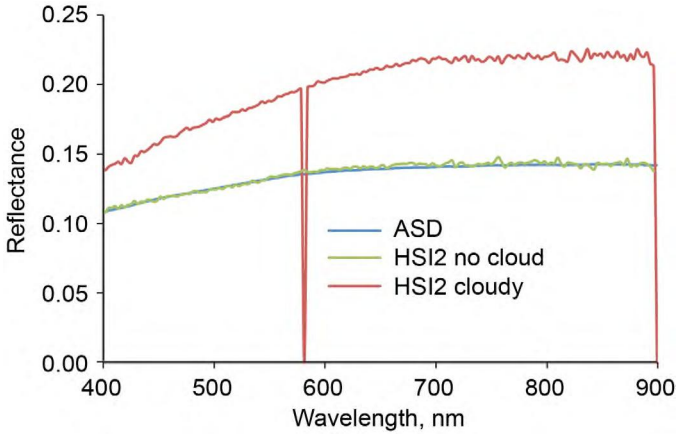

Figure 3.3.—Comparison of spectra from measured on the ground with the ASD spectroradiometer and ELM-corrected HSI2 data performed using cloud-shadowed pixels versus full sun pixels (Aug. 11, 2015). Data is of Maumee Bay State Park reference parking lot.

The primary caveat to using an empirical line method correction is that the method assumes atmospheric conditions are temporally and spatially shift invariant between the scene location recording the empirical line reflectance reference targets and the scene location containing the target or region of interest (ROI) under reflectance calibration. An example of this can be seen in misuse of empirical line correction. On one overflight of the MBSP parking lot on August 11, a portion of the reference target was under cloud cover, and a portion was under full sun (Fig. 3.3). When the correction is based on the target area in full sun, and reference in full sun, the correction is essentially perfect (see the blue and green lines in Fig. 3.1). However, when the correction is derived based on cloud covered area, it results in overcorrection of the spectral curve, not changing the overall shape, but changing the magnitude of the signal when compared with the at-ground measured reference data.

When this correction was applied across the board to locations across the lake, several trends were noted: (1) When compared to sensor simple reflectance, both the ELM and on-lake ASD-measured reflectances were lower in magnitude. This is as is expected and shows the sky path radiance between the surface and the aircraft contributing to the signal at the aircraft, even on a clear day; (2) ELM generally corrects a signal to match at-lake (ASD) measurements; and (3) there are exceptions in the ultraviolet (UV) range and in cases with large amounts of floating algal scum.

A typical set of ELM atmospherically corrected HSI2 data, collected August 17, 2015, are shown in Figure 3.4. These show the at aircraft simple reflectance, on-lake measured reflectance, and ELM corrected spectra. Of note is the removal of spectral calibration mismatch errors, and the correction in spectral shape and reflectance magnitude. There is an undercorrection in the UV, which still needs further assessment to determine the nature of error (probably due to atmospheric heterogeneity or water surface reflectance).

Figure 3.2 shows a case where data were collected on a day with light hazy cloud to full cloud cover. This comparison shows the corrected magnitude and shape, and diminished but not eliminated noise. In this case, UV undercorrection is more severe, probably due do variability in scattering.

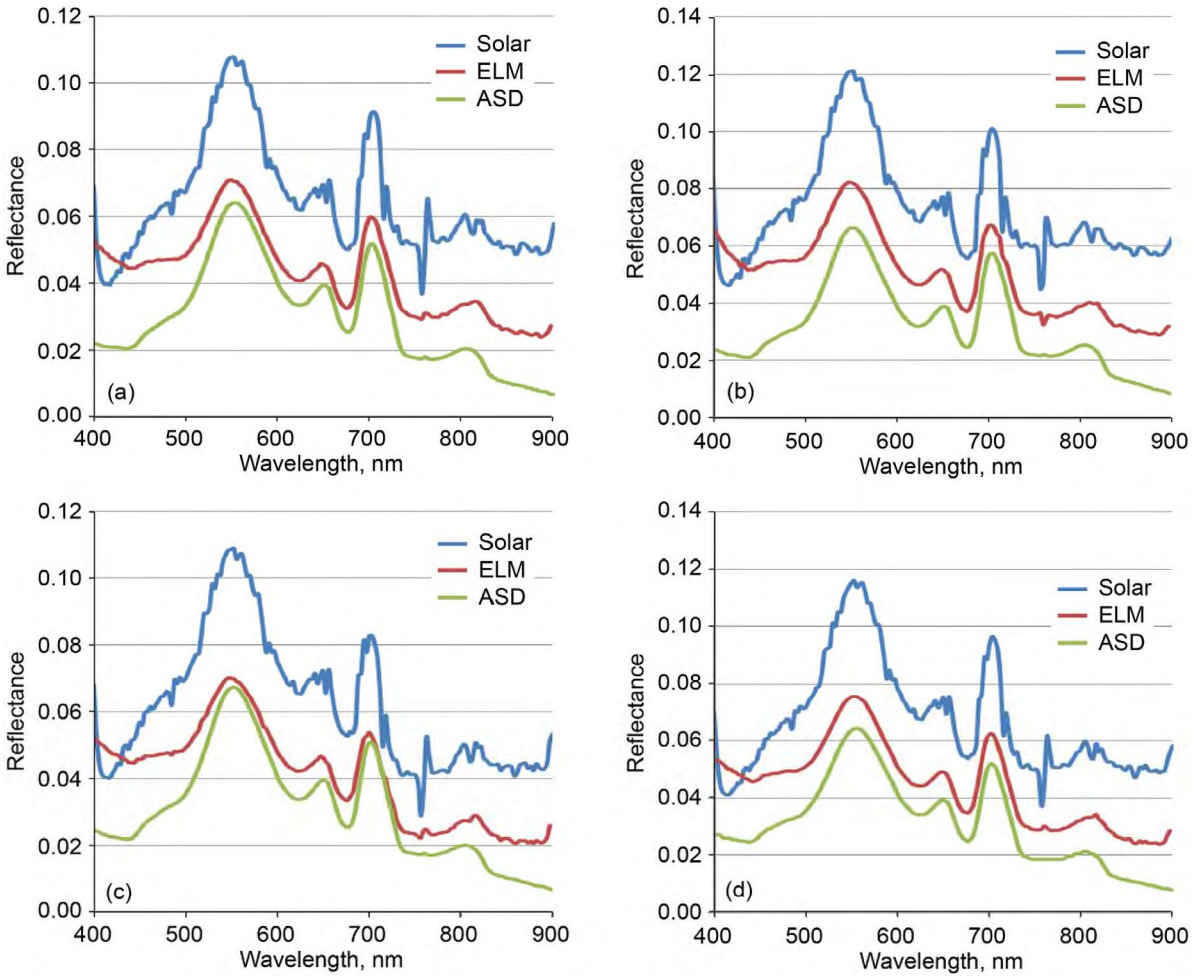

Figure 3.4.—Spectral comparisons with moderate-high algae abundance, but no surface scum and clear homogeneous atmosphere (Aug. 17, 2015). Reflectance from HSI2 data calculated by downwelling irradiance at the sensor (Solar), HSI2 ELM-corrected data, and on-lake ASD FieldSpec® 3 measurements, showing agreement between ASD and ELM correction. Figure 3.5 shows location of each site. (a) Site CRIB. (b) Site EW2. (c) Site EW3. (d) Site EW4.

Figure 3.5.—Study area of Lake Erie Western Basin. Image from ArcGIS (Environmental Systems Research Institute, Inc.).

Figure 3.6 shows spectra of Lake Erie with a high algal scum. In this case, the low reflectance in the visible is well corrected, but the significantly higher reflectance in the infrared (IR) is significantly underestimated. This may represent near-saturation response in the sensor in the NIR region. This may reflect variability in the density of the surface scum; a vessel in the water can both break up this scum and have it accumulate on one side based on wind movement of scum during sampling. On the same day with similar atmospheric conditions (mostly clear, light cirrus clouds), the correction in a lower reflectance non-scum area with a more uniform algae mixing (site 8M, Fig. 3.5) provided expected higher quality correction compared with the on-lake measured data.

Figure 3.7 shows reflectance spectra from a very clear, low humidity atmosphere in late fall, in which the ELM correction does not improve the at-sensor simple reflectance.

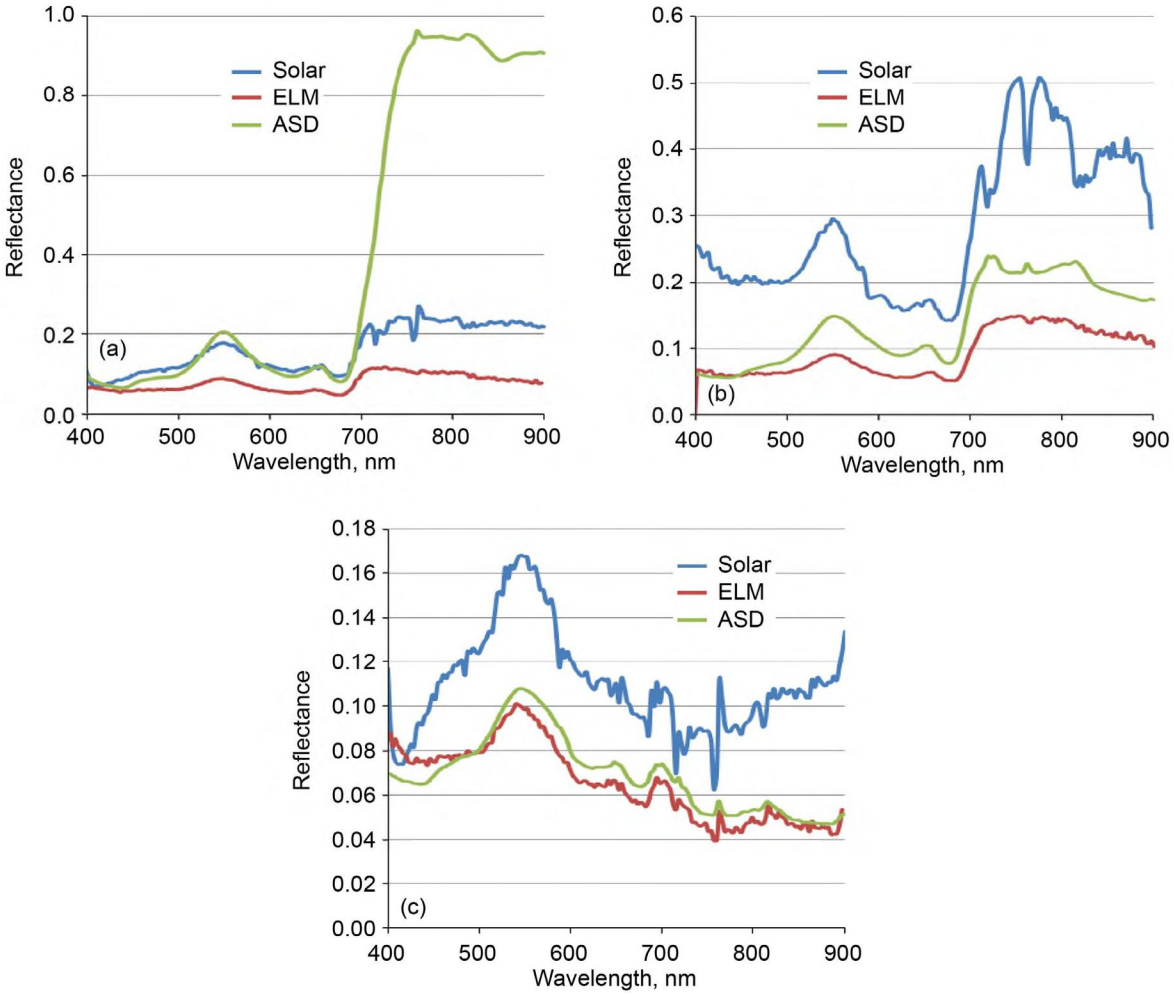

Figure 3.6.—Spectral comparison at locations with high surface algae scum (Aug. 10, 2015). Figure 3.5 shows location of each site. (a) CRIB. (b) Site 8M. (c) Site GR1.

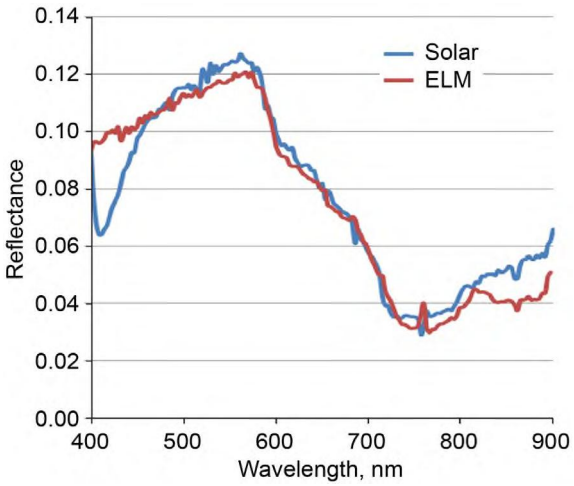

Figure 3.7.—Reflectance of Lake Erie (site GR1 (see Fig. 3.5); Oct. 19, 2015) with minimal atmospheric contribution and low algae abundance. Comparison of HSI2 and ELM-corrected HSI2 spectra. No on-lake data were aquired because of lake conditions.

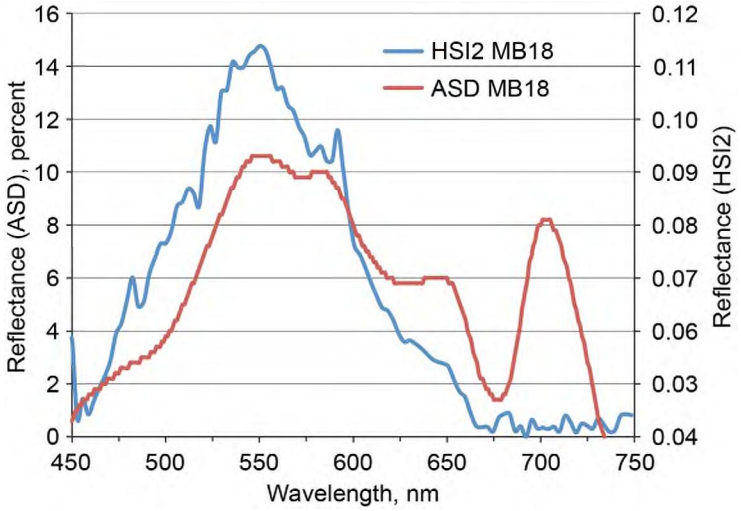

Figure 3.8.—Comparison of ASD reflectance measured on the ground and 6SV-corrected HSI2 spectra at sampling location MB18 (see Fig. 3.5).

3.2 Atmospheric Processing Using 6SV

The 6SV atmosphere processing algorithm, as implemented in the geospatial data management and analysis software suite GRASS GIS 7.0.3 (https://grass.osgeo.org/), was utilized to correct the HSI2 image from summers of 2014 and 2015. Aircraft elevation, orientation, look angle, and heading as well as time of acquisition were taken from ephemeris provided in Glenn image header information. Atmosphere properties were estimated based on airport meteorology and visibility measurements at Toledo Executive Airport, in Wood County, Ohio.

An example 6SV-corrected spectrum and corresponding on-lake ASD spectrum are shown in in Figure 3.8. Note the overall correct shape, with preservation of dual peak at 550 and 600 nm, and the cyanobacteria absorption shoulder at 620 nm. However the string chlorophyll related reflectance at 720 nm is overcorrected and masked out. This does not provide acceptable correction for chlorophyll-a (chl-a) retrieval.

3.3 Mirror-Based Empirical Line Atmospheric Correction Research

During the summer of 2015, the NASA Glenn Research Center HSI2 airborne sensor was used to obtain remote sensing imagery of the CyanoHAB algal blooms in the Western Basin of Lake Erie. South Dakota State University (SDSU) supported these airborne collections by providing ground validation data collections and in-scene reference targets for atmospheric corrections of the image data, deriving upwelling reflectance spectra of the water surface. The effort is to provide a methodology giving broad-based support to all data users participating in the Lake Erie study. The main collaboration thus far in this effort has been with Joe Ortiz at the water quality laboratory of Kent State University for his analysis using visible derivative spectroscopy of the corrected hyperspectral data. The image analysis was successful in deriving optical estimates of algal composition and toxin concentration from scenes that included the SDSU reference targets.

The innovative mirror-based atmospheric corrections approach applied to this study makes use of subpixel spherical convex mirror targets designed for water deployment in providing in-scene reflectance references. Placing a single mirror target in the recorded sensor image and collecting coincident ship-based measurements of water surface reflectance and the atmospheric diffuse-to-global ratio provides the information necessary for a two-point ELM reflectance calibration, allowing direct conversion of image pixel values (radiance or digital number (DN)) to at-surface water reflectance over the sensor field-of-view

(FOV). Coincident sensor performance and atmospheric validation data were also collected by aircraft, with multiple mirror targets deployed on a parking lot, along with nearby shore-based solar radiometry measurements.

The ELM is an approach for deriving surface reflectance measurements in a remote sensing image directly from the at-sensor image radiance or DN values using in-scene radiometric targets of known reflectance. The analysis requires at least two targets of high and low reflectance for deriving the linear transformation coefficients converting the at-sensor sensor image response to reflectance-removing atmospheric effects without the need for the sensor to have absolute radiometric calibration. The sensor performance requirements are only that the sensor response for all detectors are stable over the time the image is collected and that it is linear. Typically large-area targets are used, such as ground calibration tarpaulins, pseudo-invariant sites, or any natural extended uniform surface in which the reflectance is known from ground validation measurements. In this study the innovation was the application of mirror-based reference targets that can easily be deployed on the water surface under normal field conditions. As described in Section 3.1, the application of the ELM method requires the assumption that the atmospheric conditions are spatially and temporally invariant between the locations of the reflectance references and the target or ROI under reflectance calibration. By being able to deploy an ELM reflectance reference (mirror array) directly at the water location under study in the same HSI2 scene improves the reflectance calibration results under heterogeneous sky conditions compared to relying on ELM references located a large distance away and recorded in a HSI2 scene over a large time difference.

3.3.1 Description of the Mirror Target Design

The basic mirror target design developed for deployment on the water surface for imaging by the NASA Glenn HSI2 airborne sensor during the 2015 Lake Erie study is shown in Figure 3.9. The target consists of sixteen 10.5–in.-diameter convex mirror domes laid out in a 4 by 4 array. The target size is about 1 m^2 with mirrors having a radius of curvature R_c = 7 in. (0.18 m). The angular width of the mirror surface is 80°, reflecting a near-hemispherical view of the sky with a sky fraction parameter f = 0.83. The mirrors are second-surface acrylic mirrors and are mounted in an aluminum frame, keeping the total target weight less than 25 lb. When deployed on the water, the frame is mounted on a tube float for setting the target adrift from the boat. The target was designed to produce a high-reflectance reference supporting the in-scene ELM calibration. Based on a MODTRAN analysis, the at-sensor integrated radiance, $DN_m(\lambda)$ was designed to be 5 to 10 times brighter than the water surface at-sensor radiance to maximize the signal-to-noise ratio (SNR), but also to avoid detector saturation, taking into consideration that the point target mirror signal is spread out over multiple pixels by the sensor motion and optical point spread function (PSF). The predicted radiance for the target along with the water surface is presented in Figure 3.10, assuming a native pixel instantaneous FOV of 1.3 m consistent with the HSI2 sensor flying at about 10,000 ft. altitude.

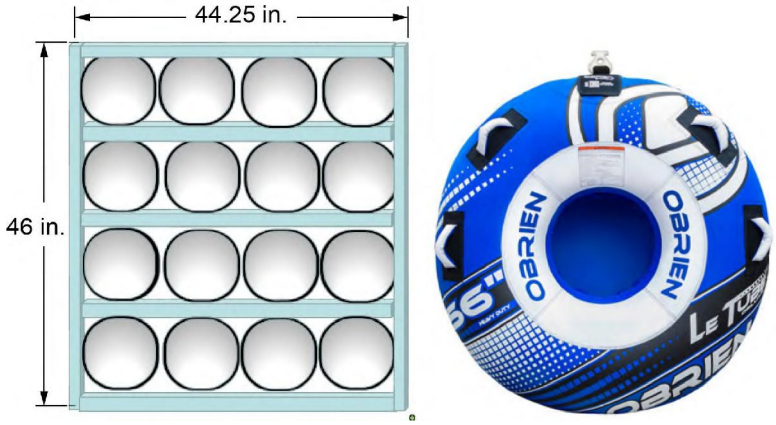

Figure 3.9.—On-water mirror target design with mirror array (left) and floatation (right).

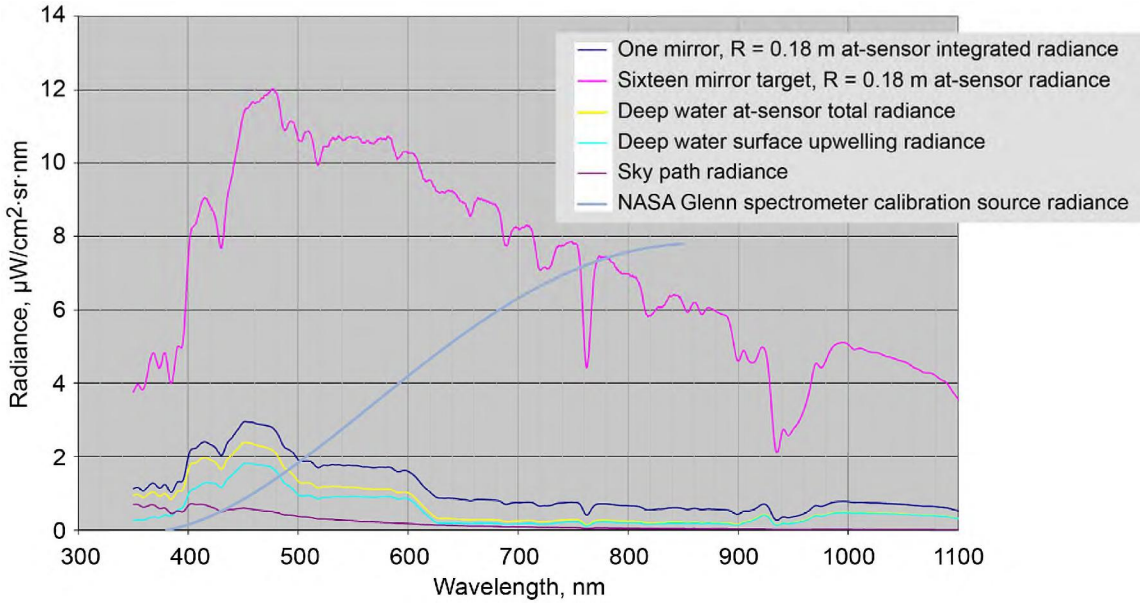

Figure 3.10.—Predicted radiance for one mirror, a 16-mirror array, sky path radiance, and the NASA Glenn calibration source.

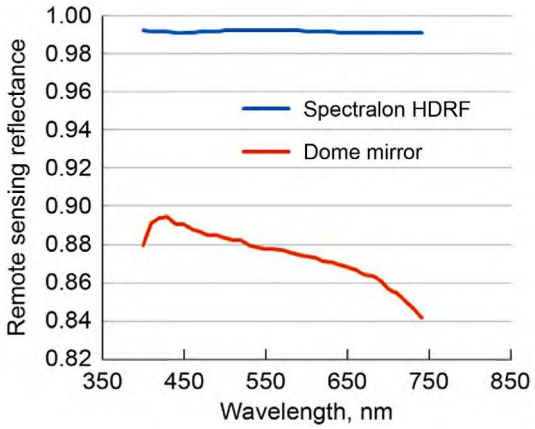

Figure 3.11.—Remote sensing reflectance of the dome mirror and the Spectralon hemispherical directional reflectance factor (HDRF).

The mirror specular reflectance spectrum presented in Figure 3.11 was measured by Joseph Ortiz at KSU with a laboratory reflectometer. It is important to recognize that the mirror reflectance does not change with the tilt of the panel when deployed on the water. Since the mirrors are spherical there is no foreshortening effect of the reflectance and no bidirectional reflectance factor (BRF) variations compared to those from flat reflectance panels. As long as the virtual image of the Sun is visible by the overflying sensor, the reflectance remains constant. Thus, the mirror target can bob around in the water under typical surface wave conditions, and the reflectance will remain constant. The mirrors are cleaned before deployment and elevated above the water sufficiently by the float to keep the surface dry. A fully operational mirror target prototype deployed in Sandusky Bay, Lake Erie, Ohio, is pictured in Figure 3.12.

Figure 3.12.—Pictures of the 16 mirror array (left), it floating in the water near the boat (center), and the floating mirror target as deployed away from the boat during overflight.

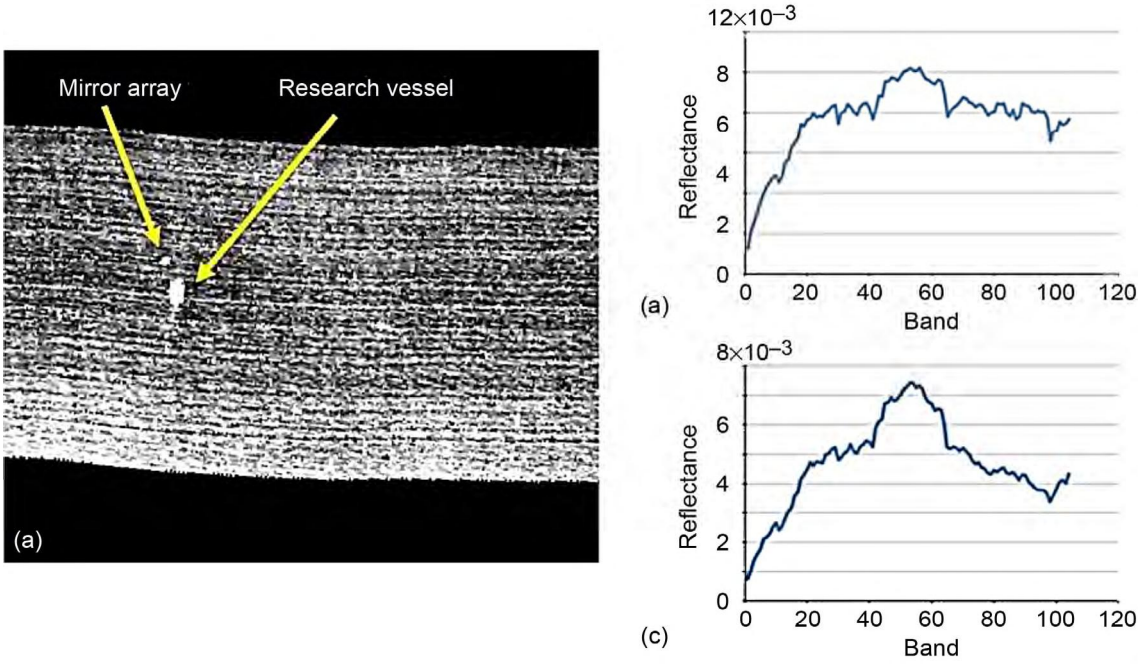

Figure 3.13.—Application of the mirror-based, empirical line method reflectance calibration. (a) Identification of the mirror target and research vessel in NASA HSI2 Swath 091815 at sample location in Sandusky Bay. (b) Average, uncorrected mirror radiance calculated from the mirror pixels in the scene. (c) Average radiance from 2000 lake pixels surrounding the mirror target and research vessel.

Figure 3.13 shows an HSI2 image of the mirror array deployed behind a boat. The spectral response of the water and the mirror target are also given. The mirror target (Fig. 3.13(b)) is much brighter than the surrounding water (Fig. 3.13(c)), but not saturated, providing the high-reflectance reference for the ELM reflectance calibration. The ratio of the lake pixels divided by the mirror pixels yields the uncorrected lake reflectance, which is used with near-coincident, lake surface reflectance measured with an ASD, Inc., FieldSpec® HandHeld 2 relative to a Spectralon calibration plate (Calibrated Diffuse Reflectance Target, Labsphere, Inc.) to determine the mirror gain function.

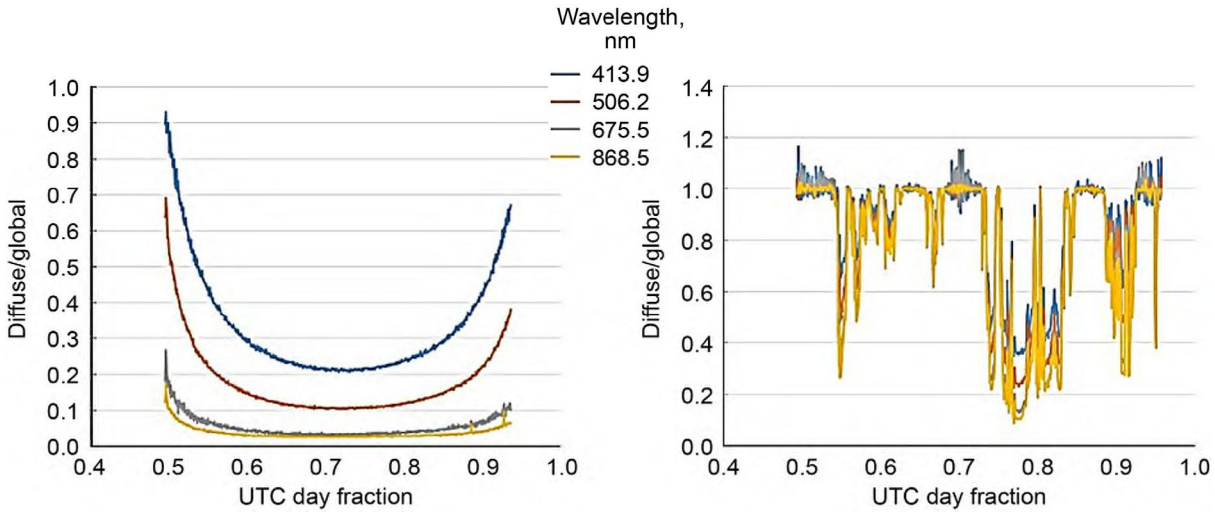

Figure 3.14.—Downwelling irradiance on horizontal surface at Sandusky Water Treatment Plant. Diffuse-to-global ratio in terms of Coordinated Universal Time (UTC) day fraction (a) Clear day (Sept. 21, 2015). (b) Cloudy day (Sept. 18, 2015).

3.3.2 Validation Data

A seven-multispectral-channel solar radiometer was deployed at Sandusky Water Treatment and the OSU Stone Laboratory to provide measurements of total downwelling, diffuse sky, and direct solar irradiance as ground validation data. Analysis provides total atmospheric transmittance, aerosol optical depth, and the diffuse-to-global irradiance ratio for radiative transfer modeling to be used in validating the image reflectance calibration. The Sandusky radiometer measurements provided a continuous collection from August 9 to September 21, 2015. Measurements at the Stone Laboratory were limited to August 12 to 20 because of equipment problems. Example data for the measured diffuse-to-global ratio on a clear day and a cloudy day are shown for comparison in Figure 3.14.

Important additional validation data for evaluating the mirror target and sensor performance was collected on August 11, 2015, with the targets deployed on a beach-side parking lot at the Maumee Regional Park. Eleven transects of the test site were flown to record the mirror target response at different altitudes. Figure 3.15 shows the target test location from 8500 ft. These data sets are being analyzed in the SDSU image processing laboratory to assess the sensor image quality performance and validate the mirror-based ELM process.

3.3.3 Development of Theoretical and Empirical Mirror-Based Atmospheric Correction for NASA Glenn Hyperspectral Imager

Working with collaborators Stephen Schiller (SDSU) and Jeff Luvall (NASA Marshall) and using additional funding from the Ohio Department of Higher Education, Ortiz (KSU) has developed and implemented an empirical mirror-based atmospheric correction and vicarious reflectance calibration method for the NASA Glenn HSI2. While Schiller and Luvall are the leads on the theoretical atmospheric correction method—described in the beginning of Section 3.3—Ortiz has taken the lead to develop an empirical mirror-based reflectance calibration that can be used to convert HSI2 radiance to remote sensing reflectance. This is a necessary preprocessing step required to extract information about algal composition from the visible portion of the HSI2 hyperspectral images. As an integral part of these two methods, arrays of convex mirrors disperse the specular reflectance of solar irradiance over a wider field of regard than would be the case with a flat mirror, thus decreasing the potential for sensor saturation. The convex mirrors reflect sunlight that is downwelling to the surface of the Earth back up to the HSI2 sensor while it is flying over in the NASA Twin Otter aircraft (Fig. 3.16). In this way, the HSI2 radiometer functions as a solar spectroradiometer by using some of its pixels to measure the direct solar irradiance reflected by the mirrors. This subset of pixels is then used to calibrate the sensor to radiance or reflectance

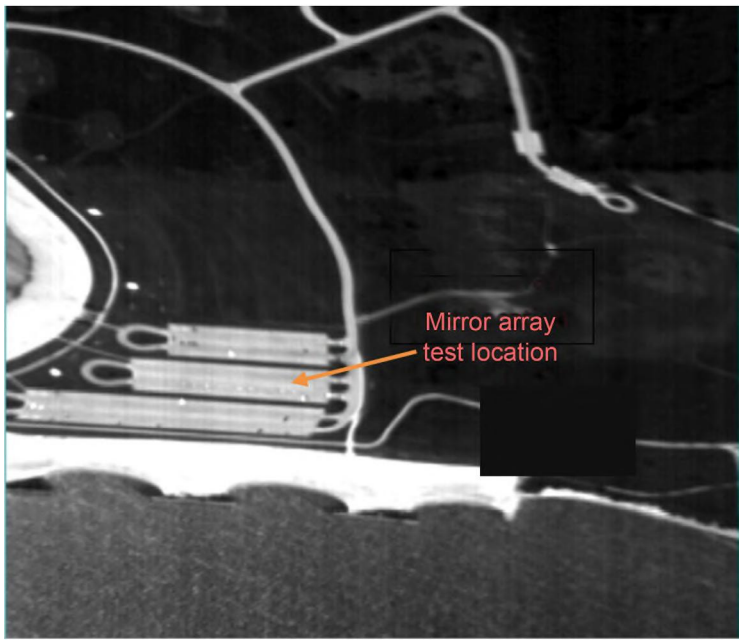

Figure 3.15.—Visual confirmation of calibration targets obtained from HSI2 swath imagery.

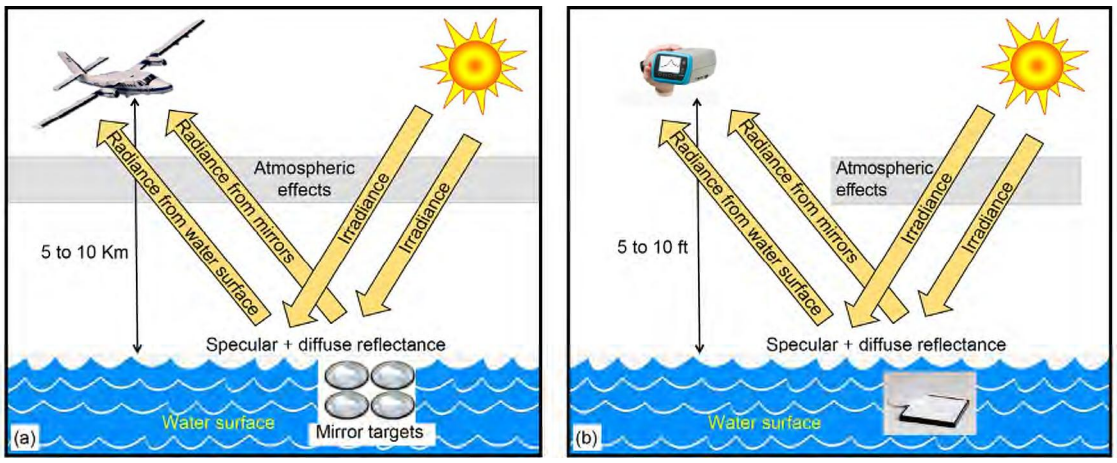

Figure 3.16.—Measurement geometry. (a) Between NASA Glenn HSI2, lake surface, and floating mirror calibration target. (b) Between the ASD, Inc., FieldSpec® HandHeld 2 (HH2), lake surface, and Spectralon calibration surface (Calibrated Diffuse Reflectance Target, Labsphere, Inc.). Spectralon plate was deployed on deck of research vessel. ASD FieldSpec® HH2 was held out over side of vessel using ~1. 6-m boom.

in essentially the same way that an ASD FieldSpec® instrument can be calibrated against solar irradiance using a Spectralon plate, provided that we can determine the gain function for the mirror is known. This is an advantageous approach because it allows atmospheric effects to be removed easily through an empirical correction method.

The mirror gain function can be determined by comparison of the reflectance ratio between the lake and mirror pixels observed using the HSI2 (Fig. 3.16(a)) against coincident or near coincident reflectance measurements of the lake surface measured relative to a Spectralon calibration plate using an ASD FieldSpec® HH2 (Fig 3.16(b)). Then the mirror gain function to normalize the downwelling radiance pixels is measured by the HSI2 to percent reflectance.

The mirror targets were deployed in Sandusky Bay and the Central Basin Coastal Transect as floating platforms deployed and recovered from the Ohio Department of Natural Resources (ODNR), USGS, or Ohio Sea Grant vessel as part of weekly sampling trips during coincident NASA overflights (see Fig. 3.13). A mirror target was also provided to collaborators at UT and affixed to the cabin roof of the UT sampling vessel as part of their weekly sampling trips during coincident NASA overflights. Two mirror arrays were laid out at Stone Laboratory and at the Sandusky Water Treatment Plant during the coincident NASA overflights. These two land-based mirror arrays were placed at locations where shadowband radiometers were deployed for continuous measurement of downwelling irradiance and atmospheric absorption properties during the course of a month-long deployment using separate funds from NASA (see Section 3.3.1). These devices were intercalibrated at MBSP during an extensive NASA overflight that allows consistent measurements between the two shadowband radiometers, the KSU spectroradiometers, and the UT spectroradiometer. Collaborators at NASA MSFC and SDSU are assisting in the development of a theoretical atmospheric correction using these data and the mirror systems.

As a demonstration of the empirical mirror-based correction approach, Figure 3.17 plots radiance measurements for mirror pixels ($n = 4$) and lake pixels ($n = 2000$) extracted from a NASA HSI2 scene collected on September 18, 2015, at ODNR Station SND1 in Sandusky Bay. The effective radiance of the mirror pixels is decreased in amplitude relative to a flat surface specular reflective signal because of the light ray dispersion resulting from the convex curvature of the mirror, which allows the signal to be measured by the HSI2 without saturating the detector. The ratio of the two radiance curves in Figure 3.17 can be used to calculate an uncorrected coincident estimate of the surface reflectance measured from the scene (Fig. 3.18). This is extremely beneficial because the measurements of the downwelling and upwelling light are coincident and obtained from the same sensor, the HSI2, measured over the entire observed two-way pathlength from the Sun to the sensor. As a result, this ratio removes the atmospheric transmittance effects from the HSI2 data. The uncorrected reflectance ratio from the HSI2 can then be compared with a white-referenced measurement of lake surface reflectance, relative to a Spectralon calibration plate, obtained from coincident or near-coincident ASD FieldSpec® HH2 spectroradiometer data obtained from the same location (Fig. 3.18). The offset in amplitude between these measurements arises from the convex mirrors. The mirror signal is corrected by comparing the radiance ratio of the water surface and that of the mirror pixels as measured with the HSI2 using near-coincident field observations of the remote sensing reflectance of the water surface at the same location obtained from the ASD FieldSpec® HH2. This provides us with an empirical estimate of the mirror gain function (Fig. 3.19).

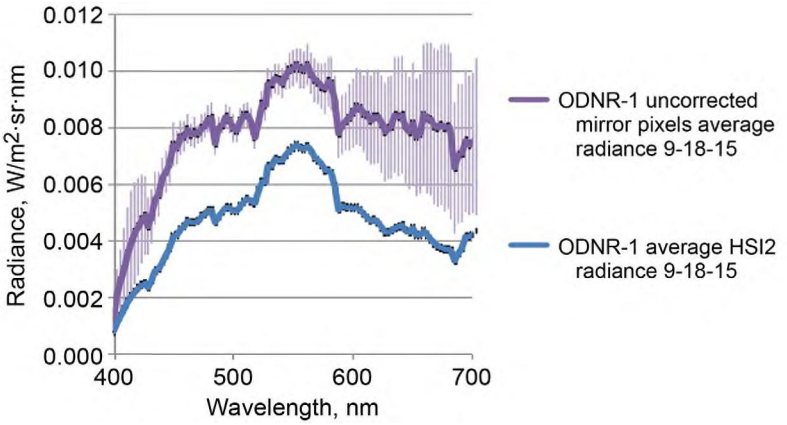

Figure 3.17.—Comparison of radiance measured September18, 2015, from mirror pixels and surface of sample location in western Lake Erie. Magnitude of mirror pixel effective radiance is defined by convex shape and number of mirrors in array.

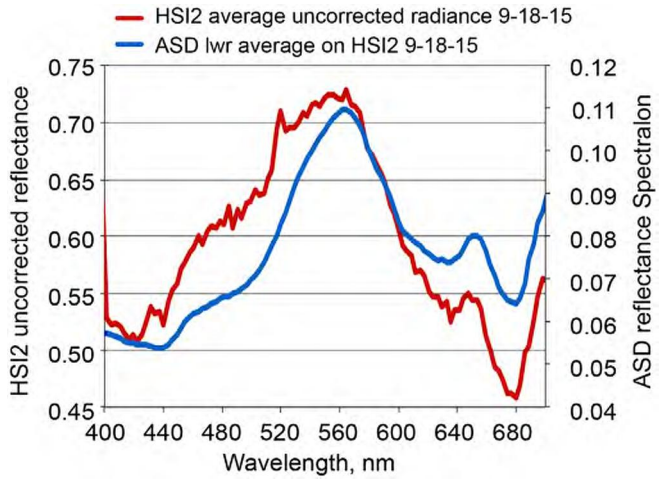

Figure 3.18.—Comparison of uncorrected reflectance ratio from NASA HSI2 (Fig. 3.17) against Spectralon white-referenced measurements of surface reflectance obtained September 18, 2015, using the ASD, Inc., FieldSpec® HandHeld 2 spectroradiometer.

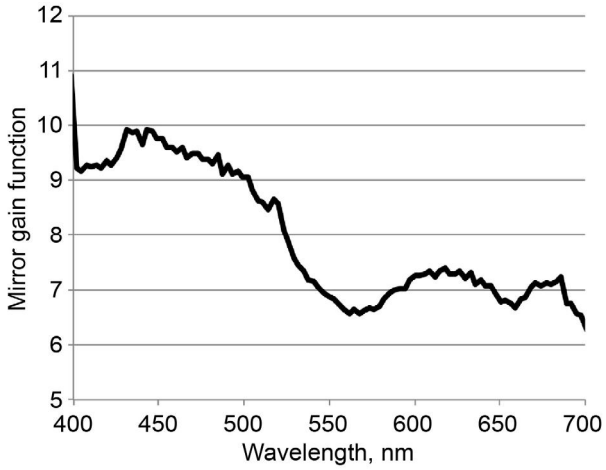

Figure 3.19.—Mirror gain function, based on the ratio of data in Figure 3.18.

The resulting corrected reflectance spectra (Fig. 3.20) obtained from the HSI2 removes atmospheric transmittance effects because the lake and mirror pixels are measured at the same time through identical atmospheric conditions, and the ratio of reflectance values in the mirror gain function also has no atmospheric transmittance effect present. An added bonus to this approach is that it rescales the reflectance values of the HSI2 to Spectralon-based reflectance using the mirror gain transfer function (Fig. 3.20). These vicariously calibrated, atmospheric-corrected reflectance data allow the spectral decomposition of the NASA HSI2 images using the KSU varimax-rotated, principal component analysis method described in Section 5.0.

Because the mirror transfer function used to obtain the HSI2-corrected reflectance values constrain the result to match the ASD FieldSpec® HH2 measurements, the precision of the method can be estimated from the result, but not the accuracy. Additional independent data must be employed to validate the accuracy of the mirror gain function and resulting reflectance measurements. In essence, all of the available degrees of freedom have been used to generate the correction factor. The accuracy of measurements is validated with independent measurements of the radiance measured from the Spectralon calibration plate using additional radiance measurements of the lake surface obtained with the ASD FieldSpec® HH2 at the same field site. These measurements are near coincident with the measurements

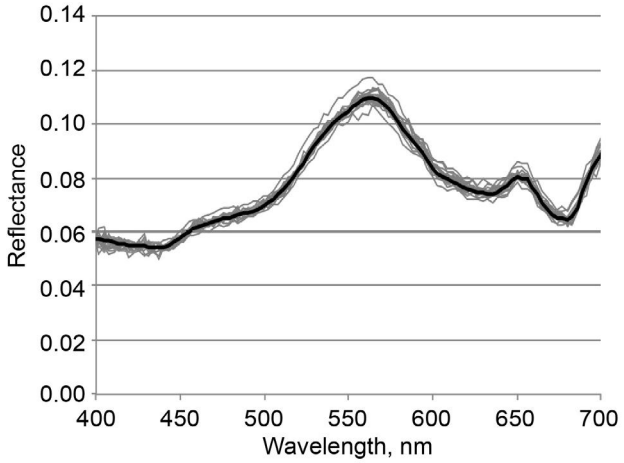

Figure 3.20.—Example empirical mirror-corrected reflectance measurements from HSI2 pixels to document range of uncertainty in method.

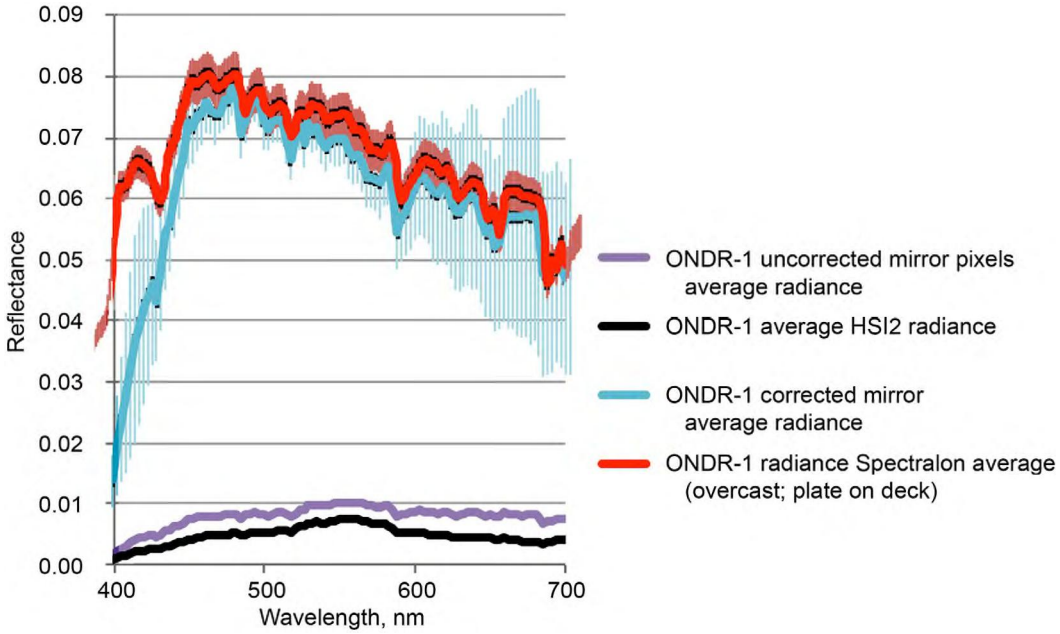

Figure 3.21.—Validation test of empirical mirror-based calibration. Shown are (1) radiance from uncorrected mirror pixels,(2) observed radiance from lake surface measured with HSI2, (3) radiance from Spectralon plate (and 1-sigma error in light red) measured with ASD, Inc., Fieldspec® HandHeld 2 spectroradiometer, and (4) Corrected radiance (and 1-sigma error) from HSI2 using empirical mirror-based calibration method.

used during the mirror calibration process. This final validation step provides a stringent test of the approach by quantifying the ability to extract absolute radiance values from the pixels that have been corrected using the empirical mirror gain function.

The results of this final validation test of the empirical mirror-based reflectance calibration method document that the method is working extremely well for most of the visible range of reflectance values (Fig. 3.21). The corrected values for the radiance of the upwelling light transmitted to the HSI2 detector from the convex mirrors agrees within 1-σ errors from 430 to 700 nm. In addition, the fine-scale structure of the radiance curve over this spectral range matches extremely well between the two independent estimates of the radiance obtained from the corrected mirror pixels measured with the HSI2 and the Spectralon-calibrated ASD FieldSpec® HH2.

It is important to point out that it is not possible to calculate a mirror gain function by taking the ratio of the HSI2-measured mirror pixels and an adjacently placed Spectralon plate, measured using an ASD Fieldspec® HH2 spectroradiometer. The reason for this is that the two instruments are calibrated to radiance using different methods, and their individual instrument response functions are not identical because of differences in electronics and optics. Using the mirrors to eliminate the detector response function of the HSI2 and making use of the ratio of reflectance values from each instrument allows this problem to be resolved.

3.3.4 Next Steps…

Potential sources of the discrepancies between the HSI2 and the Spectralon-calibrated ASD FieldSpec® HH2 spectroradiometer measurements of radiance from 400 to 430 nm have been identified, and solutions are provided:

(1) ***Lack of complete coincidence of the various data sets***—Variations in lighting properties and atmospheric aerosol effects between the various data used for the correction may explain some of the discrepancy, but the quality of the fit throughout the rest of the spectrum suggests that this is not likely the major source of error. To confirm this, additional reflectance calibration experiments need to be conducted with multiple instrument working in unison.

(2) ***Mature mirror-based empirical line method to better account for path radiance effects***—The mirror-based ELM gain function transforms the at-sensor HSI2-measured effective mirror radiance to an equivalent at-surface Spectrolon radiance as a multiplicative scale factor across the sensor dynamic range. Figure 3.21 provides validation of this transformation by comparing the gain-function-corrected mirror average radiance (blue line) with an actual coincident Spectralon average radiance recorded at the boat with the ASD spectroradiaometer. The figure shows good agreement, but with an offset that grows large below 430 nm. This is the result of the mirror gain function used in this report that corrects for atmospheric transmittance but does not fully correct for the additive path radiance between the aircraft and the water surface. A more mature mirror-based ELM algorithm that better accounts for the atmospheric path radiance will be demonstrated in further analyses.

(3) ***Radiance calibration or detector response of the HSI2***—The Labsphere calibration light source for the HSI2 does not have very high counts on the blue end of the visible spectrum, which could contribute to the observed offset in the corrected radiance measurements. The offset can arise because the gain coefficients, used to flat-field the HSI2 images, are assumed to be on an absolute scale that may have a significant bias at the low radiance UV/blue wavelength (see source radiance in Fig. 3.10). Adding a second light source with more light on the UV/blue end of the visible spectrum could increase the SNR in that part of the spectrum and help to decrease the calibration offset. The response of the HSI2 detector in the UV/blue end of the visible spectrum is presently unknown, but should be tested to determine if that might contribute to the issue.

4.0 Algorithms and Data Products

During the 2015 season, the data products provided to decision makers were the “quicklook” products that used the CI (cyanobacteria index) algorithm, described in detail in Section 4.2. Besides these products, a number of other algorithms were tested. Results from the tests of these products are included here. Finally, a new product, the varimax-rotated principal component analysis decomposition method, is being researched that has potential to provide more water constituent information. In all these cases the products were primarily tested in comparison to in situ water samples and surface optical measurements.

4.1 Field Data: Ground and Water Surface Measurements

Obtaining ground and water surface measurements and water samples in coordination with the flights is of utmost importance. The field data was needed to aid in radiometric calibration of the HSI2 as well as verify the remote sensing derived HABs products. This activity was coordinated by NASA Glenn and performed by partners external to NASA. The surface measurements allow Glenn to anchor its hyperspectral data to yield information regarding the algal composition, and in exchange, the field partners can extrapolate their single-point measurements to larger areas of interest using the flight data.

Coordination with our partners for the summer campaign was ongoing to create needed air and ground coverage. Our partners include NOAA GLERL, MTRI, UT, and KSU. Also participating on the ground are South Dakota State University and NASA MSFC for radiometric calibration and atmospheric corrections of the Glenn HSI2 using the mirror-based empirical line method.

NOAA GLERL provided a major portion of field support by means of its routine water sampling via watercraft and stationary platforms in the Western Basin of Lake Erie. MTRI and UT covered the Western Basin at alternate points of interest. KSU covered Sandusky Bay.

Measurements were taken using the ASD spectroradiometer, Secchi disk, and FluoroProbe (bbe Moldaenke GmbH), and water samples were collected for select parameters such as temperature, specific conductance, dissolved oxygen, color dissolved organic matter, sediment levels, phycocyanin chlorophyll fluorescence, nutrient levels, and Microcystis cell counts. The processing of water samples is time consuming and is still being completed. See Appendix A for details of field sampling methods.

The summaries of each partner's field collections are found in Appendix A. These include inputs from UT, MTRI, and KSU. The rest of this section of the report will focus on how well the data products and algorithms compare to the in situ data obtained.

4.2 Quicklook Products

The Quicklook products were generated in near real time (next day start of business) from radiometrically and geometrically corrected NASA Glenn airborne hyperspectral imagery. The Quicklook products include maps of subsurface and surface scum HAB occurrence. These Quicklook data products allowed for a significant improvement in the observational reporting from what was possible in 2014. A summary of the 2014 field activity and reporting are shown in Appendix B.

Once the data from overflight of the HSI2 instrument have been acquired, processing of the data from raw input to useful products begins (Fig. 4.1). NASA handles the initial preprocessing of the data, producing output that is geolocated and calibrated in the form of ENVI band-interleaved files containing at-sensor radiance rasters for each track as well as single-point-averaged at-sensor irradiance for each track. These data files are then compressed and uploaded to the MTRI Single File Transfer Protocol (SFTP) server, typically early morning on the day following the aircraft overflight.

Once the data have been uploaded to the SFTP, MTRI can initiate a semi-automatic processing routing that will download all of the compressed files and process them to produce output products. For each track file that is extracted, the routine reads wavelengths from the radiance raster images and divides every pixel by the corresponding irradiance from the point file. The result is at-sensor reflectance rasters for only the wavelengths used to compute output products. At this point, if desired, the vicarious calibration correction factor can be applied to produce an estimate of surface reflectance, but to date the majority of output data products have been produced using at-sensor reflectance.

4.2.1 HSI Empirical Line Correction for Generation of Quicklook HAB Products

"Vicarious calibration" refers to techniques that make use of natural or artificial sites for postlaunch calibration of sensors. This is a key step in the evaluation and improvement of HSI data products as it demonstrates how close to reality the HSI2 sensor is getting and allows the remaining error to be accounted for.

The first step in vicarious calibration is identifying a natural or artificial site for comparison. The HSI team and collaborators have chosen the MBSP parking lot as a suitable location for several reasons. The first is that the site is located along the immediate shoreline of Lake Erie and is in close proximity to points of interest such as the Toledo Water Intake, which means it does not impose an undue burden on flight planning and navigation. Second, the parking lot has a consistent and well characterized spectral response across both time and space (Fig. 4.2). Third, the parking lot is a relatively large feature that can be easily identified in HSI2 imagery at any operational elevation (Fig. 4.3).

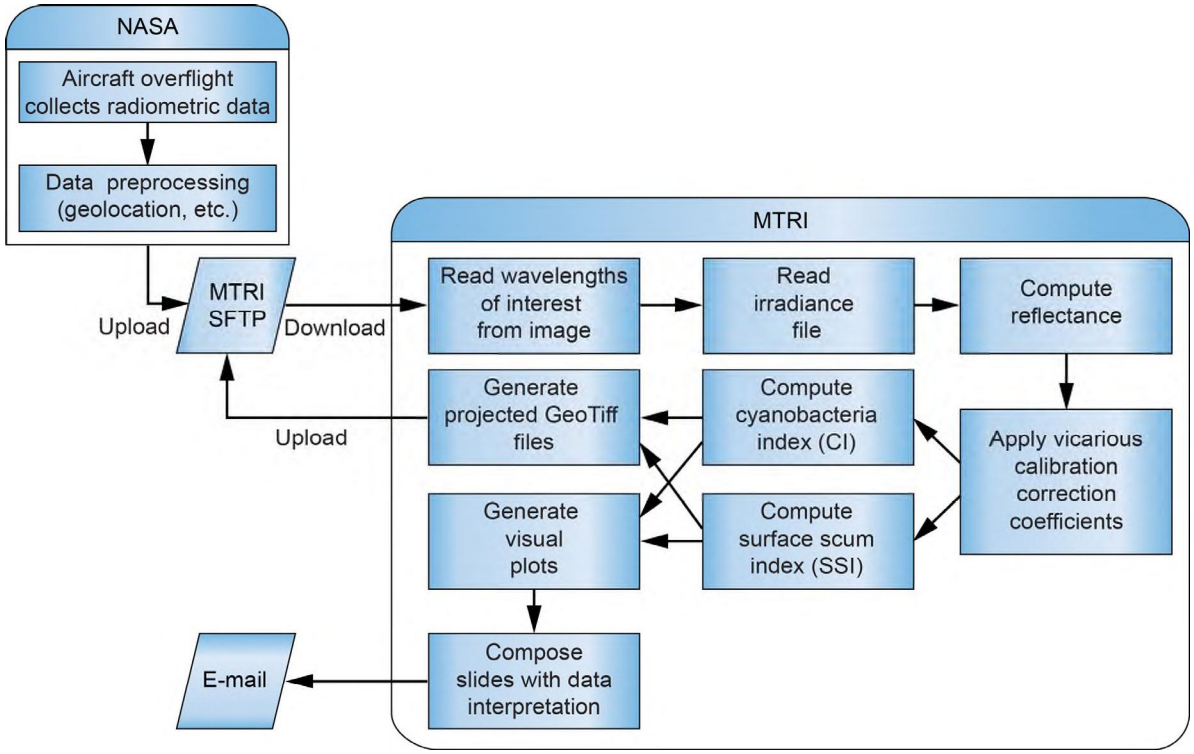

Figure 4.1.—NASA HSI2 data Quicklook processing procedure. MTRI is Michigan Technological Research Institute, and SFTP is Single File Transfer Protocol.

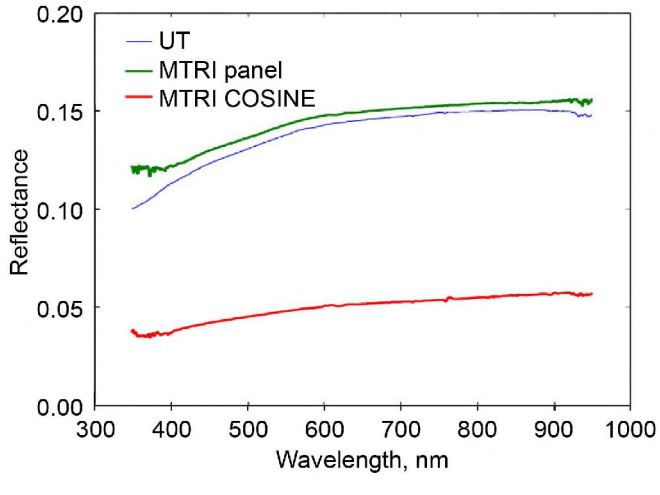

Figure 4.2.—Maumee Bay State Park parking lot reflectance.

Figure 4.3.—Maumee Bay State Park parking lot. Image from ArcGIS (Environmental Systems Research Institute, Inc.).

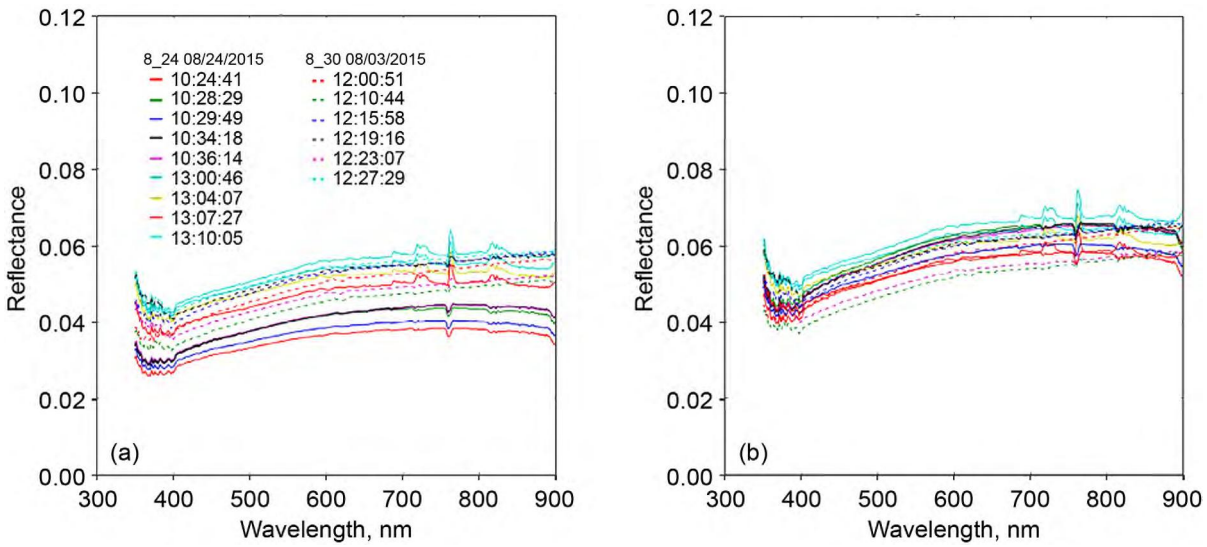

Figure 4.4.—Maumee Bay State Park in situ reflectance. (a) Before time correction. (b) After time correction.

Once a site has been located, the next step is to collect data with both the instrument to be calibrated (HSI2) as well as sensors that are known to be well calibrated (field ASD measurements). Optimally, such measurements will be collected at the same time over multiple time periods to establish statistical credibility, but it is possible with a single measurement from each device. It is important that measurements include both radiance and irradiance so that reflectance can be calculated, otherwise even small differences in illumination will contaminate the results. Another consideration is that ground measurements should consider the effects of solar angle on the diffuse illumination component of radiance if a cosine receptor is used to measure irradiance. When using a Spectralon panel, mirror, or other known reflector to estimate irradiance, the effect of the diffuse term will cancel out when computing reflectance. The cosine receptor does not include this term, whereas the radiance measurement does, and will therefore remain in the computed reflectance if not accounted for. The effect is readily apparent (Fig. 4.4(a)) in the split between the 10:30 and 13:00 measurements from the MTRI ASD on August 24 (Fig. 4.4), which the time correction removes.

With the reflectance calculations for both the calibrated instrument and the instrument to be calibrated available, the next step is to calculate the correction factor, which is a wavelength-dependent scalar that relates the two reflectance measurements. Alternatively, if multiple points are available, a more sophisticated equation may be substituted, such as a scalar and offset. The correction factor equation will encapsulate the measurement differences between the two sensors, including all sources of measurement error, and can be used to convert measurements from one instrument into the other. Of obvious interest is converting the uncertain sensor to match the well-calibrated instrument (see correction factor curves, Fig. 4.5). The wavelength-specific correction factors are calculated by

$$C(\lambda) = \frac{Cal_{\mathrm{Ref}}(\lambda)}{Uncal_{\mathrm{Ref}}(\lambda)}$$

$$Cal_{\mathrm{Ref}}(\lambda) = C(\lambda) * Uncal_{\mathrm{Ref}}(\lambda)$$

where C is a correction coefficient, λ is wavelength, Cal_{Ref} is calibrated reflectance, and $Uncal_{\mathrm{Ref}}$ is uncalibrated reflectance.

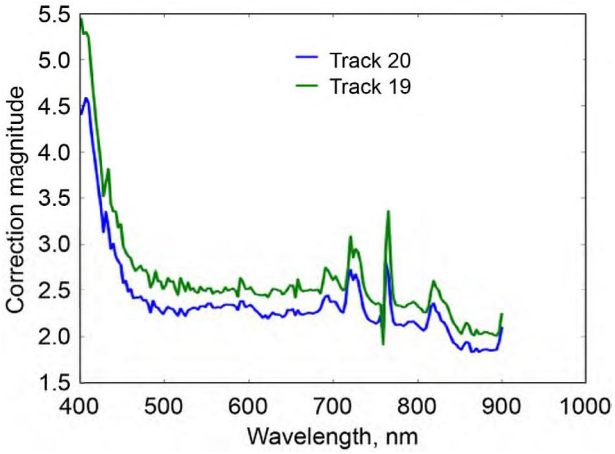

Figure 4.5.—Wavelength-specific correction coefficients derived from comparing to in situ reflectance for two NASA HSI2 tracks.

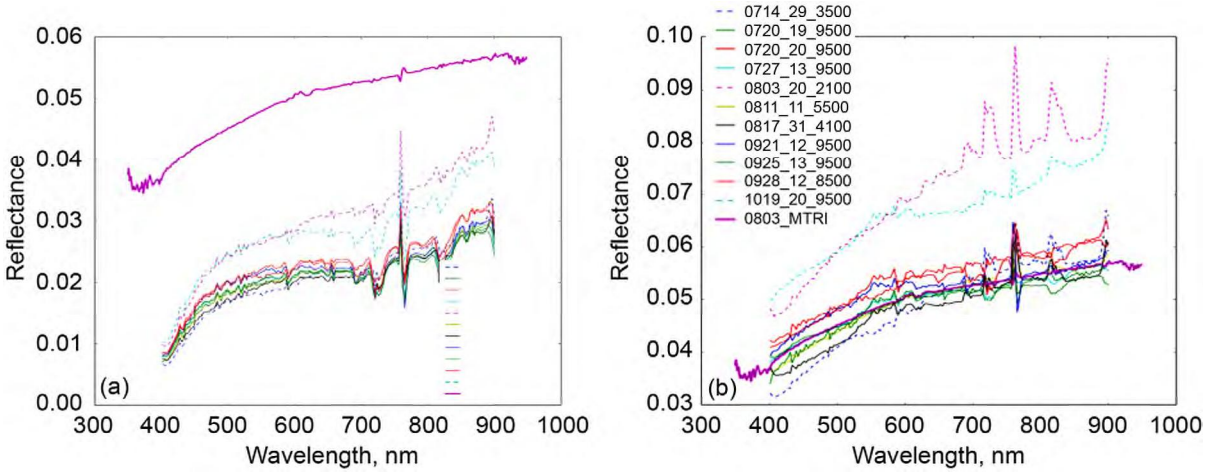

Figure 4.6.—NASA HSI2 parking lot reflectance. Note in situ reflectance is shown (labeled 0803_MTRI) in both panels. (a) Uncorrected. (b) Corrected.

In Figure 4.6(a), the parking lot as observed by the HSI2 sensor is relatively constant across images; the remaining differences are likely atmospheric or time of day effects. This suggests that a single correction factor would be useful even on days for which it was not recomputed, as demonstrated by the corrected signals clustering around the observed MTRI ASD spectra (Fig. 4.6(b)). The two anomalous dates are both flagged as cloudy (dashed line), which could be explained by clouds periodically shadowing the irradiance measurements, which were averaged across the entire track, leading to a higher than normal reflectance measurement. Previously it was believed that the correction factor would serve as a method of atmospheric correction; however, further analysis suggests the effect of atmosphere is either minimal or located primarily below 2000 ft. Each of the parking lot spectra is labeled according to the flight altitude of the aircraft, and no readily observable pattern between altitude and reflectance is evident. This suggests that the correction factor is compensating for some other source of error that dwarfs anything the atmosphere is inducing in the measurement.

To further analyze the effectiveness of the correction factor, grass and beach spectra from MBSP were measured for comparison between the ASD measurements and HSI2 data (Figs. 4.7(a) and (b)). The highest quality ASD data were selected, which resulted in same-day imagery from HSI being unavailable, but the results are intriguing nonetheless considering all of the HSI2 spectra are from the same image (Sept. 25, Track 13). Spectra from the beach obtained on August 3 from the ASD shows strong agreement with the HSI2 after correction in the low blue bands but falls short as the wavelength increases. Spectra of grass near the parking lot collected by the ASD on August 24 show an even more interesting pattern, in which the blue and green wavelengths are too low, wavelengths near 700 match almost perfectly, and longer wavelengths are then too low. The image in Figure 4.7(c) was collected from MTRI field collect site HABS 3A on the same day as the HSI2 imagery. In a radical departure from the other samples, the uncorrected spectra show strong agreement with the ASD measurement, whereas the corrected spectra are much higher in magnitude. Together these suggest a possible sensor gain error with brighter target observations since the correction factor overcorrects low signals and undercorrects bright signals. Further characterization and removal of this error should vastly improve the quality of the HSI2 imagery.

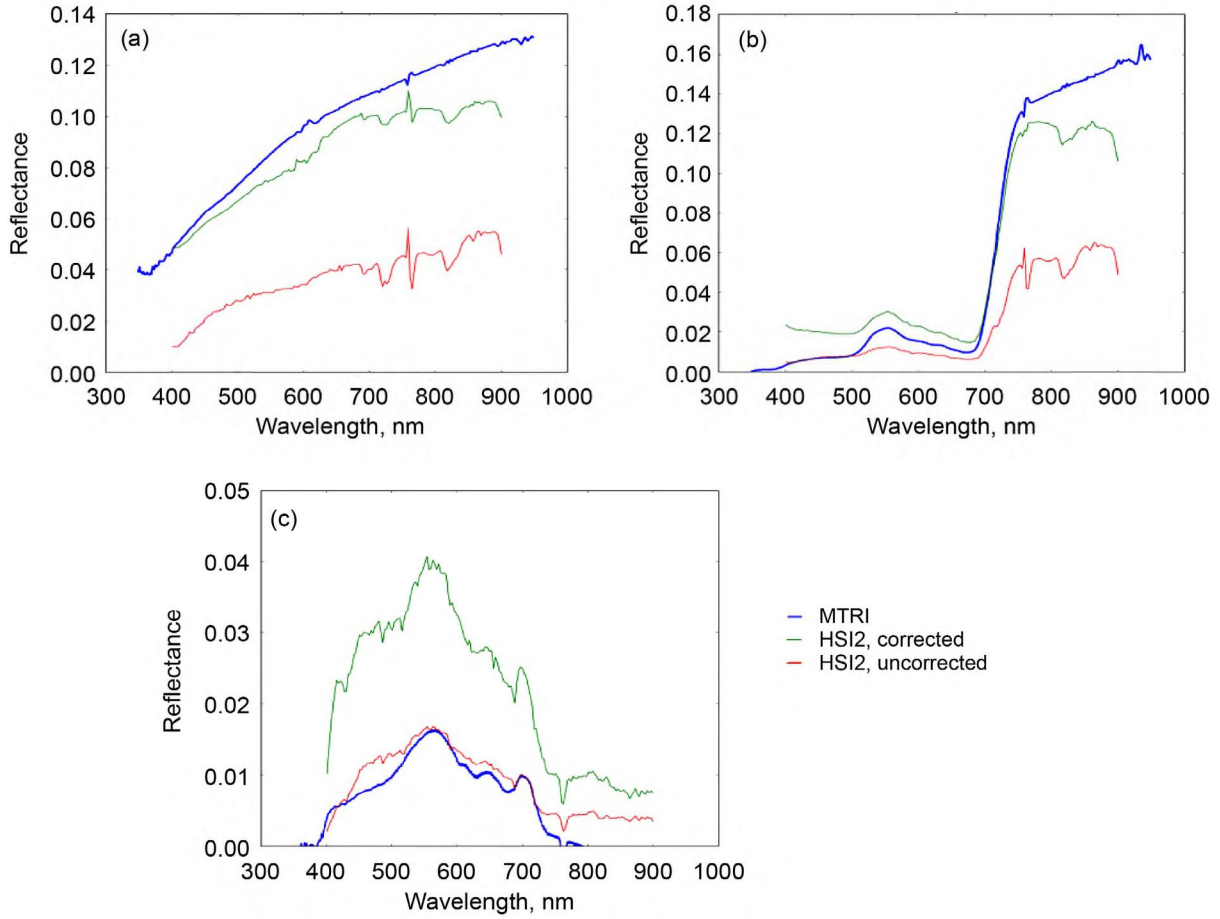

Figure 4.7.—NASA HSI2 corrected and uncorrected reflectance spectra (Sept. 25, 2015) compared with Michigan Technological Research Institute (MTRI) ASD spectra (Aug. 8, 2015). (a) Beach sand. (b) Grass. (c) Water.

4.2.2 CI and SSI output products

MTRI has thus far produced two primary output products: the cyanobacteria index (CI) and surface scum index (SSI). The CI algorithm looks for a specific spectral feature that indicates cyanobacteria presence: an increase in reflectance in a narrow region around 680 nm. It does so by comparing the reference wavelength reflectance to the reflectances on either side of the reference that should appear outside the spectral feature. Examples of these data products are shown in Figure 4.8.

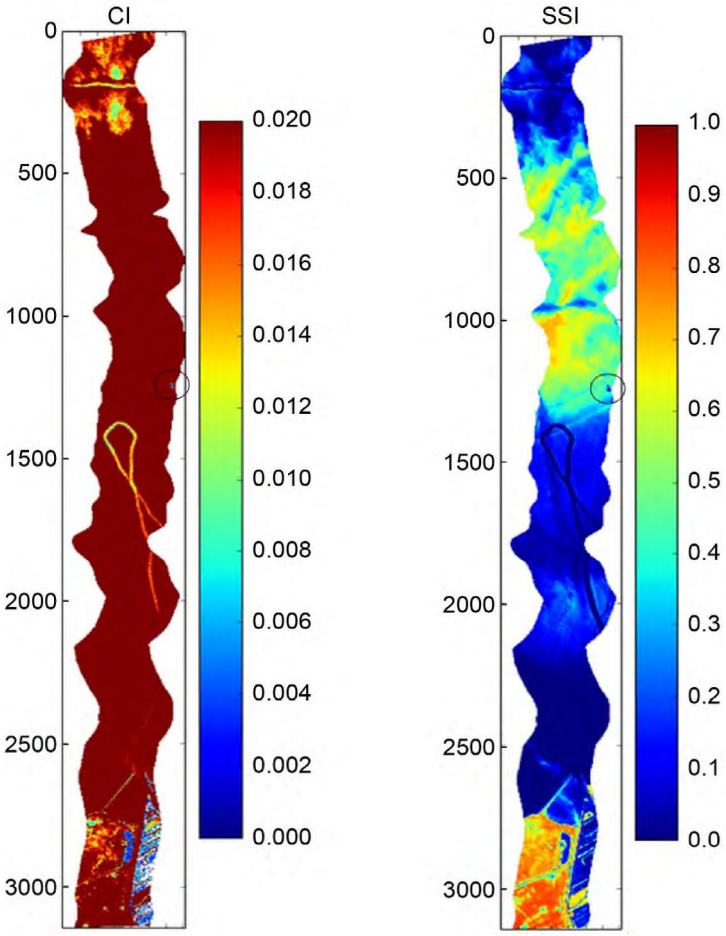

Figure 4.8.—NASA HSI2 tracks from August 10, 2015, near the Toledo water intake, shown by black circles on each track (see Fig. 3.5 station location “CRIB"), processed with cyanobacteria index (CI) and surface scum index (SSI). Note the land area at the bottom of each track (lines >2500, left-hand grid of each track).

The CI is calculated from the spectral shape (SS) as

$$SS_{(679)} = R(679) - R(664) - \left[R(709) - R(664)\right] \times \left(\frac{679 - 664}{709 - 664}\right)$$

$$CI = -SS_{(679)}$$

where

$R(664)$ = reflectance (664 nm)
$R(679)$ = reflectance (679 nm)
$R(709)$ = reflectance (709 nm)

as described in Stumpf et al. (2012). This relative value enumerates the level and presence of cyanobacterial activity. The more positive the value, the more activity is present in that area. The contrary is true for negative values, which indicate a lack of cyanobacterial activity.

The SSI (Sayers et al., 2016) is a normalized-difference-vegetation-index- (NDVI-) style calculation in which any positive response is indicative of surface scum. NDVI calculations distinguish vegetation from other signals by the strong response in the near-infrared (NIR) wavelengths. Since water readily absorbs NIR light, the algorithm can easily distinguish surface scum from subsurface blooms: subsurface chlorophyll will appear nonvegetative to an NDVI calculation.

The SSI is calculated as

$$SSI = \left[\frac{\left(R(858) - R(667)\right)}{\left(R(858) + R(667)\right)}\right] > 0$$

where

R(667) = reflectance (667 nm)
R(858) = reflectance (858 nm)

Next, the processing routine generated visual plots for both data products. The CI is set on a logarithmic scale ranging from 0.0001 to 0.02, and the SSI is set on a linear scale from 0 to 1. Both products have values less than 0 clipped for easy distinction between very low values and values that indicate no response. The plots are automatically saved as image files for inclusion in reports. The actual data values are also output as GeoTiff files with the rotation applied from the ENVI header files for use with other mapping software such as ArcMap (esri) or QGIS (Creative Commons).

Once the processing procedure has finished, typically approximately 60 min depending on the volume of data from the overflight, the MTRI team prepares a Quicklook observations report. The goal of the presentation is to leverage MTRI's image interpretation expertise and familiarity with the algorithm computations to provide a summary of the overflight findings. The report aims to cover points of interest, such as overflights of water intakes, as well as other interesting algal bloom features present in the imagery, while also noting land or cloud features that might be misinterpreted as blooms. The report concludes with a summary of the team's findings and is then delivered by e-mail to interested parties. Full completion of the process, from initial download of data from NASA to completion of the report, was typically done by close of business the same day NASA finished uploading data.

So far, processing has focused on verifying the integrity of the HSI2 data, as well as processing output of a few select robust algorithms that are relatively unaffected by at-sensor atmospheric interference. Future work will include atmospheric correction through the vicarious calibration procedure as part of standard processing (rather than experimental only), as well as a suite of more complex algorithms that cannot function without such correction, such as the color-producing agent algorithm (CPA-A) (Shuchman et al., 2013) or other chlorophyll retrieval algorithms. There is also a strong desire to include land and cloud masking to improve interpretability of data products.

4.3 NASA HSI2 Quicklook Product Examples

NASA Glenn and MTRI worked closely to produce HSI2 Quicklook products the day after flight for the rapid dissemination of information to interested stakeholders. Surface scum and CI images were produced for every recorded flight over Lake Erie, Harsha Lake, and the Ohio River. Figure 4.9 is an example of the standard MTRI Quicklook products produced the day after flight. The left track is processed with the CI and the right track is processed with the SSI. Note the small-scale resolvable features (i.e., ship wakes) in both products. Figure 4.10 shows a series of tracks over Harsha Lake, OH, processed with the CI. The images show very little indication of cyanobacteria in the main lake; however, higher concentration HAB "plumes" can be seen in the very southern area of the lake. The NASA HSI2 system provides the ability to "mow-the-lawn" to provide synoptic analysis of smaller lakes and/or rivers. Figure 4.9 shows the standard CI product for three tracks made over the Ohio River on September 3, 2015. The track paths are shown on the left panel. Note the visible HAB streaks found in all three tracks. This example shows the enhanced utility of the HSI2 system to provide critical HAB presence data for small targets (i.e., rivers) that are not readily observed from operational polar orbiting satellite systems.

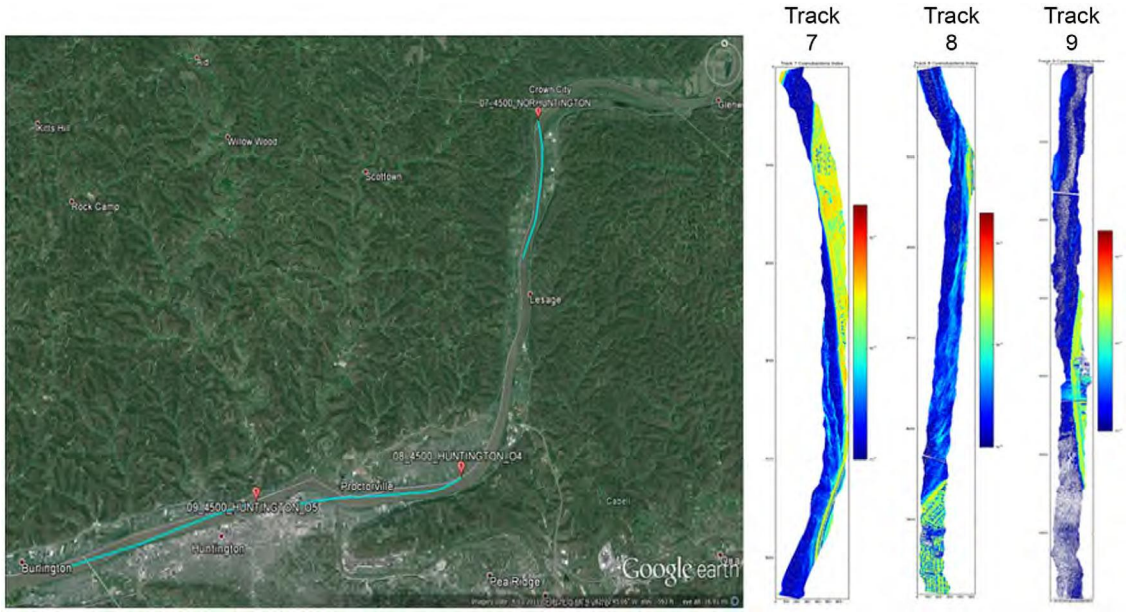

Figure 4.9.—NASA HSI2 tracks processed with cyanobacteria index over Ohio River (Sept. 3, 2015). Copyright Google Earth.

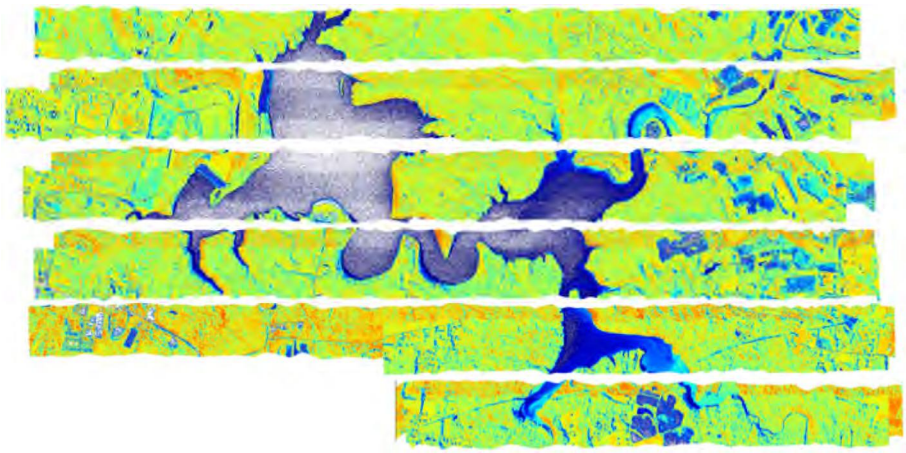

Figure 4.10.—NASA HSI2 tracks processed with cyanobacteria index over Harsha Lake.

4.4 HSI2 Quicklook HAB Products Compared With MODIS HAB Products

There are several operational HAB products derived for Lake Erie using daily MODIS (Moderate Resolution Imaging Spectroradiometer) imagery (i.e., Wynne, 2015; Becker et al., 2009; Sayers et al., 2016). Although these products are useful for tracking long-term annual HAB extent trends, they are not particularly robust with respect to observing detailed spatial patterns because of the 1-km spatial resolution. The satellite products are also rendered unusable in the presence of clouds. Figure 4.11 depicts the MODIS true-color image recorded on August 10, 2015. Note that almost the entire area of the Western Basin of Lake Erie is covered by clouds. Overlaid on the cloud image are the HSI2 tracks flown on the same day processed with the CI. Tracks with more green pixels indicate higher CI values and thus more HAB presence. The ability of the HSI2 to record data under the clouds can provide water-intake managers important information that may not be available through operational satellite monitoring.

The airborne-derived hyperpectral data products are most useful when they augment the products currently made available from satellite imagery, such as the bloom map in Figure 4.12. Multispectral satellite data is the only way to observe the extent of algal blooms over time while hyperspectral airborne imagery can provide higher detailed snapshots of particular locations that provide better differentiation between HABs and nuisance blooms. Here the extent of the bloom is covered in the satellite imagery while the NASA HSI2 CI image shows much more detail with respect to HAB location and intensity around Toledo water intake system than MODIS-based product does. The HSI2 data was obtained in number of flight lines in the bloom area to help get more understanding as to whether the bloom was a potential HAB or instead was a nuisance algal bloom. Figure 4.13 shows that the flight lines were modified to accommodate different bloom locations for that particular day. These transects of the bloom helped to supplement what is already available from multispectral satellite data.

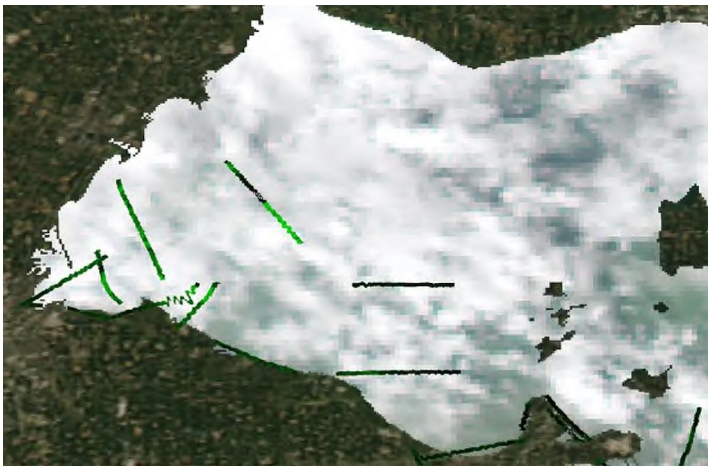

Figure 4.11.—NASA HSI2 tracks processed with cyanobacteria index overlaid on same-day MODIS (Moderate Resolution Imaging Spectroradiometer) true-color image.

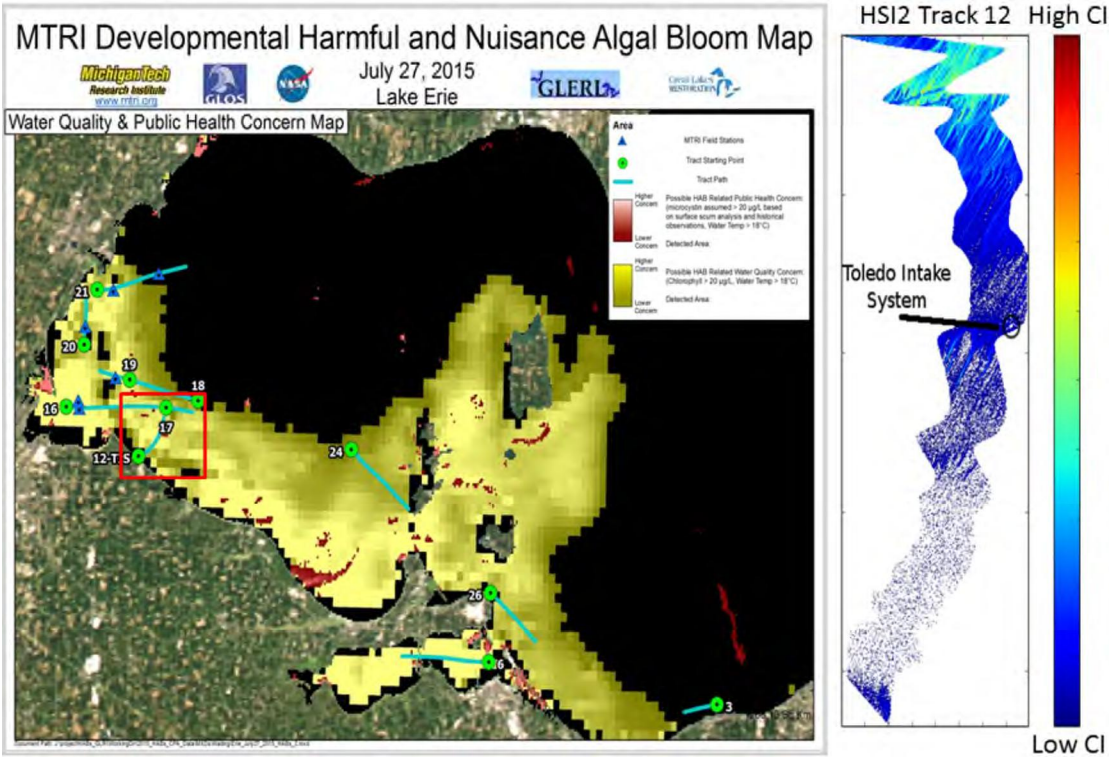

Figure 4.12.—NASA HSI2 tracks overlaid on Michigan Technological Research Institute (MTRI) MODIS (Moderate Resolution Imaging Spectroradiometer) harmful algal bloom (HAB) mapping product (July 27, 2015). HSI2Track 12 is shown in right panel, and its location is highlighted by red box in the left panel.

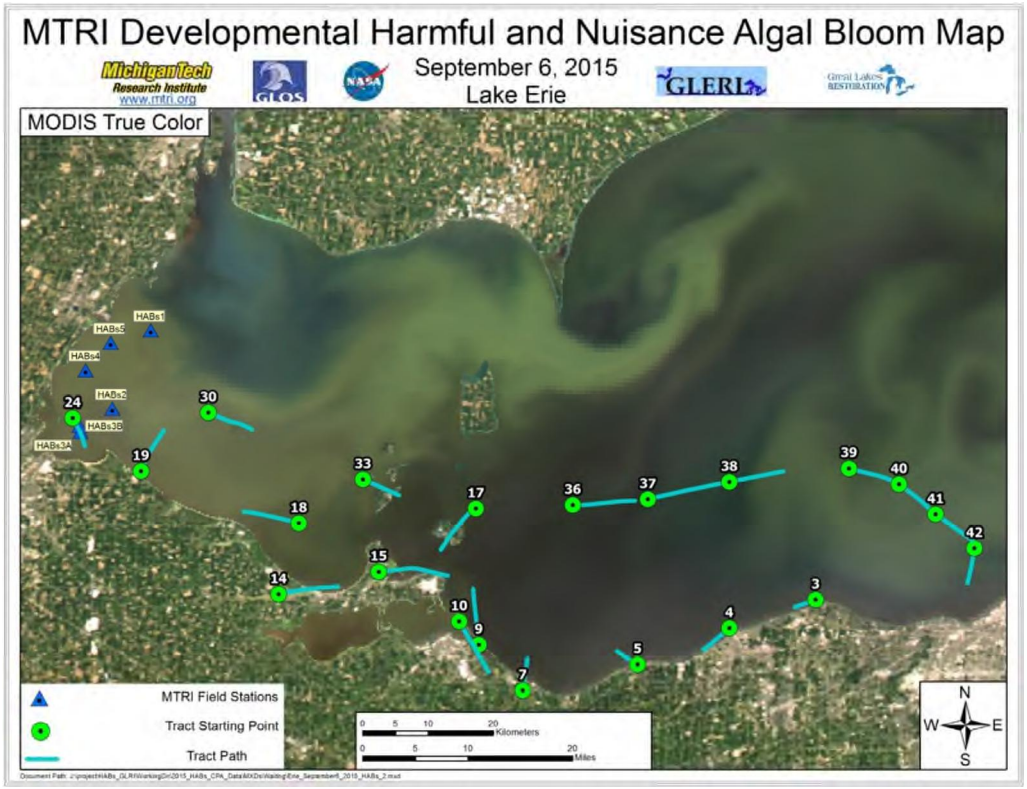

Figure 4.13.—NASA HSI2 tracks overlaid on MODIS (Moderate Resolution Imaging Spectroradiometer) true-color image (Sept. 6, 2015).

4.5 Comparison of HSI2-Derived Data Products and In Situ Measurements—MTRI

To assess the ability of the NASA HSI2 system to provide quality HAB- and chlorophyll-a-derived products, several established algorithms were applied to the HSI2 imagery and compared to coincident (same-day) in situ observations made by MTRI in 2015: The CI and Simis phycocyanin (PC) ratio were the HAB-specific algorithms used as well as the ocean color indexes, OC4E and OC3M (O'Reilly et al., 1998, and O' Reilly, 2000), and maximum chlorophyll-a index (MCI) algorithms for total chlorophyll-a.

NASA HSI2 CI values were compared to in situ fluorometric measurements of the cyanobacteria (blue-green algae) pigment phycocyanin concentrations in the Western Basin of Lake Erie (Fig. 4.14). Cyanobacteria measurements were made using a bbe fluoroprobe lowered and raised through the water column to generate depth profiles of algal abundance. The fluoroprobe measurements were averaged to 1-m increments with the upper meter being used for comparison with the HSI data. Matchups between HSI and in situ data were made where both datasets were recorded on the same day. A strong relationship between fluoroprobe cyanobacteria chlorophyll-a and HSI CI is evident for the 16 available matchups (coefficient of determination $R^2 = 0.84$).

NASA HSI2-derived OC3M and OC4E algorithm values were compared with in situ fluorometric measurements of total chlorophyll-a concentrations in the Western Basin of Lake Erie (Fig. 4.15). Field sampling and matchup comparison methods were the same as described for CI evaluation. Both OC3M and OC4E algorithms produced derived chlorophyll-a values that were approximately 5 times less than the in situ data, indicating little sensitivity to chlorophyll-a values in the range (5 to 70 μg/L) of those observed in the flights over the Lake Erie Western Basin. This is an expected result since the OC family of algorithms were designed for Case I waters (Morel and Prieur 1977) of the open ocean. They have been shown to provide somewhat reasonable estimates for chlorophyll-a concentration in certain areas of the Great Lakes and may be useful in characterizing less turbid water as part of a water quality algorithm framework for case II waters in future missions.

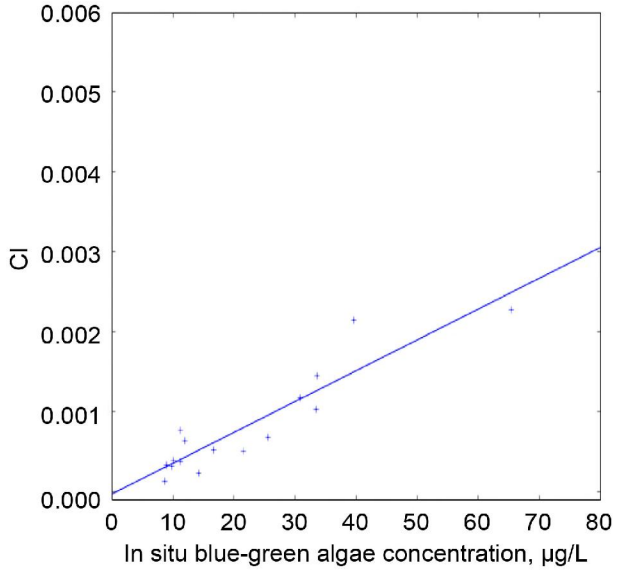

Figure 4.14.—Comparison of HSI2-derived cyanobacteria index (CI) values and in situ fluoroprobe cyanobacteria (blue-green algae) chlorophyll-a concentrations.

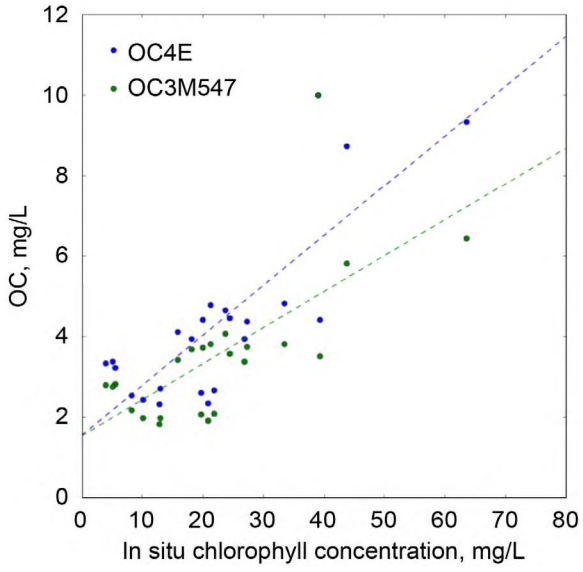

Figure 4.15.—Comparison of HSI2-derived ocean color OC4E and OC3M values and in situ total chlorophyll-a concentrations.

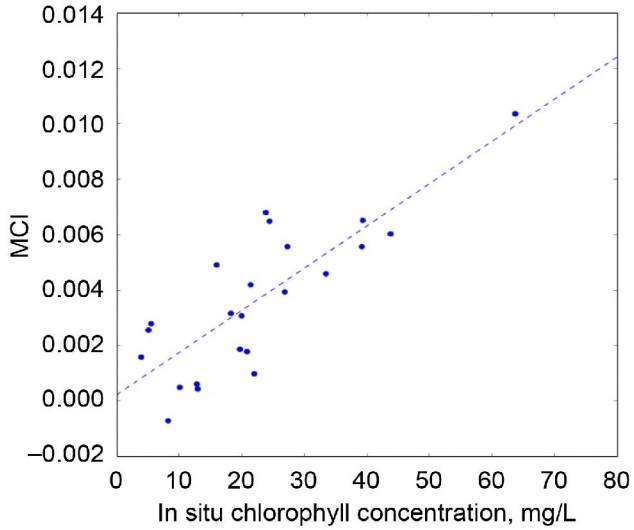

Figure 4.16.—Comparison of HSI2-derived maximum chlorophyll-a index (MCI) values and in situ fluoroprobe total chlorophyll concentrations.

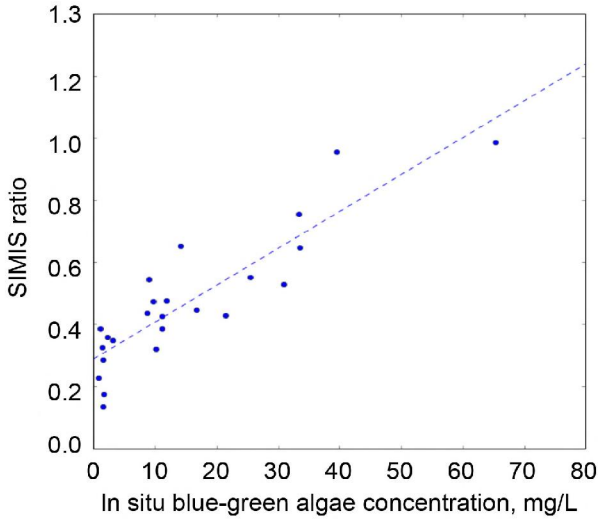

Figure 4.17.—Comparison of HSI2-derived Simis phycocyanin ratios and in situ fluoroprobe cyanobacteria (blue-green algae) chlorophyll-a concentrations.

NASA HSI2-derived MCI values were compared to in situ fluorometric measurements of total chlorophyll-a [chl-a] concentrations in Western Basin of Lake Erie (Fig. 4.16). Field sampling and matchup comparison methods were the same as described for the CI evaluation. A fairly strong linear relationship exists between HSI2 MCI and in situ chlorophyll-a ($R^2 = 0.66$). MCI may be a useful indicator for large quantities of total chlorophyll-a concentration, particularly when HABs are not the primary focus of characterization (i.e., diatom blooms, dinoflagellates, etc…).

NASA HSI2-derived phycocyanin absorption ratio (709 nm/620 nm) values (based on Simis, Peters, and Gons, 2005) were compared to in situ fluorometric measurements of cyanobacteria chlorophyll-a concentration in the Western Basin of Lake Erie (Fig. 4.17). Field sampling and matchup comparison methods were the same as described for the CI evaluation. A strong linear relationship exists between HSI Simis ratio and in situ cyanobacteria values ($R^2 = 0.78$).

4.5.1 Remote Sensing of Cyanobacteria and Chlorophyll-a: The Simis and Randolph Method

In addition to the Quicklook data that was provided, a number of additional algorithms were tested but not provided as Quicklook data. The algorithms developed by Simis and further developed by Randolph were employed in order to quantify the concentration of the pigment phycocyanin (Randolph et al. 2008, Simis, Peters, and Gons, 2005). Backscatter was found using Randolph's equation and the backscatter result was then utilized in the equations provided by Simis. Randolph's values for the constants defined in Table 4.1 were also used, as they proved to be more useful to our purposes than those suggested by Simis. These values were derived from a number of other works including those of Astoreca et al. (2006), Gons et al. (1999), and Gordon et al. (1988). Certain constants were used in these calculations as well, including the absorption by water at various wavelengths (Buiteveld, Hakvoort, and Donze 1994).

The value of the specific absorption coefficient of phycocyanin at 620 nm·m^{-1} ($a^*_{PC}(620)$) was derived by dividing the absorption of phycocyanin at 620 nm by the measured concentration of blue-green algae from a water sample. However, since these data were only available at the seven sampling sites, these seven values were averaged and the resulting value was then used as the $a^*_{PC}(620)$ value for all calculations.

The workflow of equations from both Simis and Randolph is exhibited in Equations (1) through (4) in Table 4.2.

TABLE 4.1.—CONSTANTS AND COEFFICIENTS USED IN THE SIMIS ALGORITHM

Constant	Definition	Value
$a_w(620)$	Absorption coefficient of water at 620 nm, m^{-1}	0.281
$a_w(665)$	Absorption coefficient of water at 665 nm, m^{-1}	0.401
$a_w(709)$	Absorption coefficient of water at 709 nm, m^{-1}	0.727
$a_w(778)$	Absorption coefficient of water at 778 nm, m^{-1}	2.71
γ	Correction factor for $a(665)$	0.68
δ	Correction factor for $a(620)$	0.84
ε	Conversion factor used to relate absorbences by chl-a at 665 and 620 nm	0.24
α	Correction factor for surface refraction	0.60
γ'	Experimental factor	0.082
$a^*_{PC}(620)$	Specific absorption coefficient of phycocyanin at 620 nm (m^{-1})	0.03408752

TABLE 4.2.—EQUATIONS USED IN SIMIS AND RANDOLPH METHOD TO CALCULATE ABSORPTION COEFFICIENT OF PHYCOCYANIN

	Equation[a]	Source
(1)	$b_b = \left[a_w(778)\cdot\alpha\cdot R(778)\right]\cdot\left[\gamma' - \alpha\cdot R(778)\right]^{-1}$	Randolph et al. (2008)
(2)	$a_{chl}(665) = \left(\left\{\frac{R(709)}{R(665)}\cdot\left[a_w(709)+b_b\right]\right\} - b_b - a_w(665)\right)\cdot\gamma^{-1}$	Simis et al. (2005)
(3)	$a_{PC}(620) = \left(\left\{\frac{R(709)}{R(620)}\cdot\left[a_w(709)+b_b\right]\right\} - b_b - a_w 620\right)\cdot\delta^{-1} - \left[\varepsilon\cdot a_{chl}(665)\right]$	Simis et al. (2005)
(4)	$[PC] = \frac{a_{PC}(620)}{a^*_{PC}(620)}$	Simis et al. (2005)
(5)	$SS_{(681)} = R(681) - R(665) - \left[R(709) - R(665)\right]\cdot\left(\frac{681-665}{709-665}\right)$	Wynne et al. (2010)
(6)	$CI = -SS_{(681)}$	Wynne et al. (2010)

[a]b_b is total backscatter coefficient
a_w(xxx) is absorption coefficient of water at specified wavelength
α is correction factor for surface refraction
R(xxx) is reflectivity at specified wavelength
γ' is experimental factor
$a_{chl}(665)$ is absorption coefficient of chlorophyll-a at 665 nm·m^{-1}
γ is correction factor for $a(665)$
$a_{PC}(620)$ is absorption coefficient of phycocyanin at 620 nm·m^{-1}
ε is conversion factor used to relate absorbencies by chl-a at 665 and 620 nm
$a^*_{PC}(620)$ is specific absorption coefficient of phycocyanin at 620 nm·m^{-1}
$[PC]$ is concentration of phycocyanin
$SS_{(681)}$ is spectral shape at 681 nm
CI is cyanobacteria index

4.5.2 Accuracy Testing of Simis Algorithm Using Ground Reference Data

In order to test the accuracy of the Simis and Randolph equations, the calculations were carried out site-by-site using the ground reference data collected using the ASD spectroradiometer and the same set of constants and coefficients defined in Table 4.1. This provided an evaluation of the cyanobacteria concentration method where the input optical data were unaffected by any imperfections in the atmospheric correction technique. Such corrections were not necessary for data collected at ground level.

The regression analysis of this method provides promising results. When plotting the measured concentration of blue-green algae against the derived concentration of phycocyanin at each site, there is a moderately strong linear trend. This is supported by the R^2 value of 0.7683, as seen in Figure 4.18 and reported in Table 4.3. This indicates that when atmospheric interference and correction are not taken into account, the algorithms provided by Simis (and improved upon by Randolph) generate a useful result.

The result from the ENVI calculations of the Simis and Randolph algorithms yielded a result that was less promising than the results provided by the ground reference data. As reported in Figure 4.18 and Table 4.3, an R^2 value of 0.7683 indicates a weaker correlation between the derived phycocyanin concentrations and the concentrations of blue-green algae measured at each site than other methods. This was most likely related to sensitivity to errors in the atmospheric correction. Overall it is evident that Simis's algorithm is not as applicable as other methods assessed for the analysis of imagery in the optically complex Western Basin.

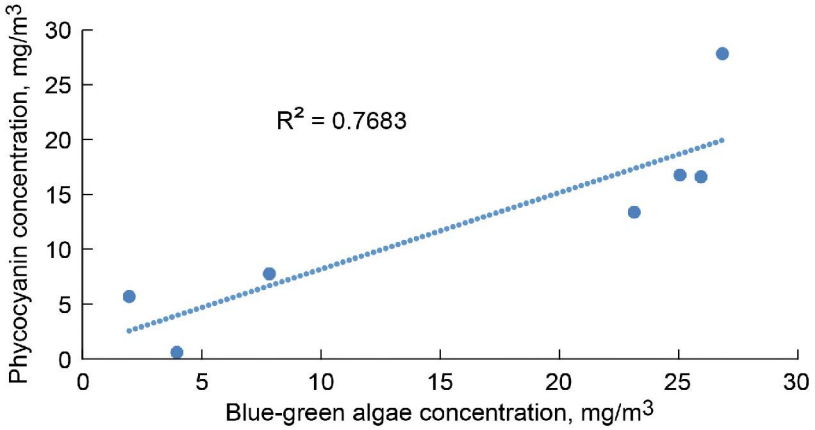

Figure 4.18.—Comparison of Simis phycocyanin concentrations derived from ASD measurements and fluoroprobe blue-green algae concentrations (expressed as mg/m^3 chl-a) from column-integrated lake samples.

TABLE 4.3.—COEFFICIENT OF DETERMINATION R^2 VALUES FOR COMPARING SIMIS-ALGORITHM-DERIVED PHYCOCYANIN CONCENTRATION AND CYANOBACTERIA INDEX (CI) WITH FLUOROPROBE-MEASURED BLUE-GREEN ALGAE ABUNDANCE

Method	R^2 value
Simis et al. (2005) using ground reference data	0.7683
Wynne et al. (2010) using ground reference data	0.9326
Wynne et al. (2010) using remotely sensed data	0.7981

4.6 Comparison of HSI2-Derived Data Products and In situ Measurements—UT

Researchers from the University of Toledo likewise evaluated the performance of multiple cyanobacteria products utilizing similar approaches with their own ground data to obtain independent results. They performed independent calculations using the same set of algorithms and compared their results to their in situ measurements.

4.6.1 Accuracy Testing of Wynne Method Using Ground Reference Data

As previously discussed, the work of Wynne et al. (2008, 2010) can be used for the calculation of the amount cyanobacterial abundance, enumerated as the cyanobacteria index, CI. This is particularly useful because unlike the algorithm proposed by Simis, it is highly resistant to imperfections in the atmospheric correction as well as negative radiance readings that commonly occur as a result of these corrections. Although the Wynne method does not explicitly calculate microcystin levels and also has the potential for sensitivity towards other highly productive algal blooms, it does utilize algorithmic parameters that focus on the spectral characteristics specific to microcystin. This includes the use of a shape algorithm centered around 681 nm where the spectral signature of microcystin exhibits a characteristic curvature due to its high absorbency at this wavelength. Further, the use of the reflectance at 709 nm in the calculation of spectral shape is also useful in targeting the algorithm towards the identification of microcystin, as a strong reflectance in this wavelength is indicative of that specific cyanobacterium. This method was carried out using Equations (5) and (6) in Table 4.2.

When applied to the ground reference data collected by the ASD spectroradiometer, it is evident that a moderately strong correlation exists between the measured concentration of blue-green algae and the calculated CI. The strength of this correlation is indicated by an R^2 value of 0.93, which indicates that this method shows the potential to consistently deliver an accurate index of the level of cyanobacterial activity occurring in Lake Erie's Western Basin. The regression analysis used for this validation is shown in Figure 4.19. A correlation is presented, as CI is calculated in cell count, and the fluoroprobeconcentrations are in pigment concentration units.

4.6.2 Accuracy Testing of the Wynne Method Using Remotely Sensed Imagery

As indicated in Figure 4.20, the same algorithm provided a moderately strong correlation between the measured concentration of blue-green algae and the CI calculated for the same geographic points from the HSI2 imagery. The R^2 value of 0.798 is indicative of this correlation. When comparing relationships between HSI2-derived CI values and fluoroprobe data from MTRI and UT sampling, some differences in relationships are noted. UT fluoroprobe data were obtained from samples drawn from an integrated full water column, and MTRI fluoroprobe analyses are conducted on top-meter samples. The HSI-derived CI has a very similar correlation between both measures of CI, but with a different linear coefficient due to the difference in comparison property (whole column vs. top meter). This is a notable result as there is a large uncertainty about how much the near-surface samples represent the entire water column when estimating biomass. Future work should be done using a combination of vertical profile samples and integrated samples to determine the significance of their relationship.

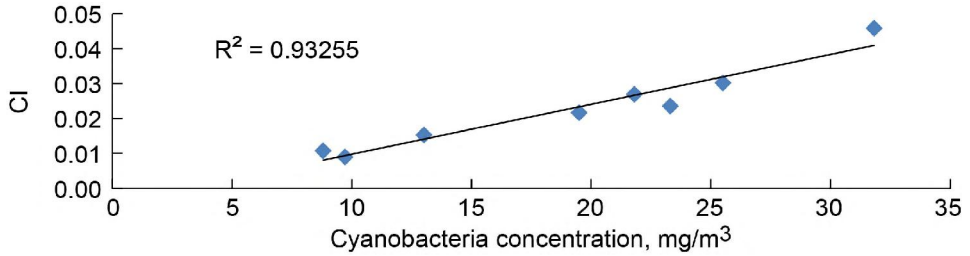

Figure 4.19.—Cyanobacteria index (CI) values derived from ASD spectroradiometer measurements versus fluoroprobe cyanobacteria concentrations from column-integrated lake samples taken August 10 and September 8, 2015.

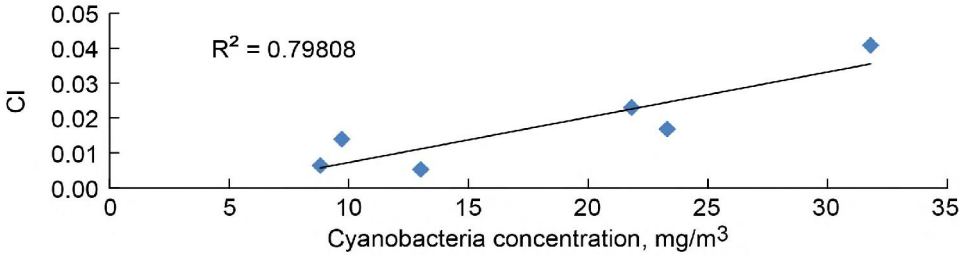

Figure 4.20.—Comparison of cyanobacteria index (CI) values derived from HSI2 measurements with fluoroprobe cyanobacteria concentrations from column-integrated lake samples taken August 10 and September 8, 2015.

Both the Simis and Randolph method and the Wynne method worked well in returning a proxy for the amount of HAB activity in a location from the ground level. For the Simis and Randolph method, this proxy was expressed in terms of phycocyanin concentration, whereas Wynne's method provided a cyanobacterial activity index. Wynne et al. (2010) does argue that the CI can be related to Microcystis cell concentration with CI of 0.001 (1/sr) = 100,000 cells/mL. Stumpf et al. (2012) corroborates that result. No correction is needed for ASD optical measurements made at the lake level, so data were unaffected by atmospheric effects. For this level of data, both methods proved to be robust. However, when atmospheric corrections and then the respective algorithms were applied to the HSI2 imagery, the Simis and Randoph technique was found to be no longer as accurate. The Wynne method, on the other hand, was wholly unaffected by any error that may have been introduced to the HSI2 imagery data via the atmospheric correction.

Although Simis's equation calculates phycocyanin concentration that may seem more applicable as a proxy of the amount of microcystin, the accuracy of the method when applied to atmospherically corrected images simply does not hold up. It is too affected by the correction-induced errors and loses much of its validity. Although Wynne's equation does not necessarily calculate the concentration of phycocyanin or microcystin directly, the cyanobacterial index CI proves to be a useful tool for the measure of HAB activity in Lake Erie's Western Basin, and potentially case II waters in general.

For comparison with another atmospherically corrected dataset, the empirical line method (ELM) correction was applied to the Hyperspectral Imager for the Coastal Ocean (HICO) imagery. HICO is an imaging spectrometer on the International Space Station that was active from 2009 to 2014 (Oregon State University, 2009). The HICO sensor provided a regular stream of data on the lake's surface, but at a coarser spatial resolution than the HSI2 airborne data. HICO data are collected at a 5.7-nm spectral resolution over 87 bands ranging over the wavelengths of 380 through 960 nm (Oregon State University, 2009). An ELM-corrected airborne HSI2 image set was then be used to correct the HICO satellite imagery. The ELM is once again employed; however, instead of using light and dark areas from MBSP, the seven Western Basin locations sampled that day were used (Fig. 3.5). For this study, these correction points have been defined by spectral libraries composed of the spectral averages taken at each site that were obtained from the HSI2 images. These averages are of a 1- by 1-pixel resolution. In the cases where the sampling location and the HSI2 imagery did not overlap because of variations in flight path by the airborne instrument, a point as close to the sampling site as possible within the HSI2 image is used with at least a 10-pixel distance from the edge of the HSI2 image. These points were applied to the HICO image as correction factors using the Empirical Line Compute Factors function in ENVI, thus providing an atmospherically corrected HICO satellite image for Lake Erie's Western Basin. From this, CI were derived for HICO-derived imagery, and similar correlation was achieved with the CI as those from the HSI2 data (Fig. 4.21).

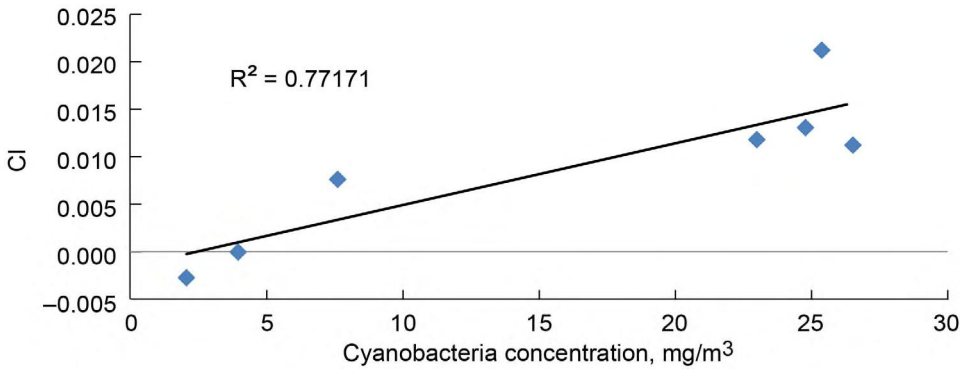

Figure 4.21.—Correlation of cyanobacteria index (CI) calculated from HICO data compared to fluoroprobe cyanobateria concentrations from water samples taken August 15, 2014.

4.7 Summary of Results from Simis, Randolph and Wynne Methods

A combination of ground-reference, airborne, and satellite data over Lake Erie's Western Basin were used to test ATCOR4, 6SV, and ELM atmospheric correction methods of HSI2 imager data. Following the selection of the best method, abundances of chlorophyll-a (chl-a), the blue-green algae pigment phycocyanin, and cyanobacteria from hyperspectral imagery were estimated with algorithms derived by Simis, Peters, and Gons (2005), Randolph (2008), and Wynne (2010). This provides insight into the amounts of various algae types, most notably being Microcystis, as indicated by phycocyanin. Two research teams utilized separate computations, approaches and in situ measurements to obtain similar conclusions.

Based on tested application of ATCOR4 and 6S, the ELM was found to produce the best results. The ELM was applied to the airborne HSI2 imagery, using the ground-reference data at MBSP as correction points.

Although the algorithms published by Simis and Randolph provided acceptable results at ground-level correction ($R^2 = 0.7683$), they were not reproducible from flight data. Wynne's approach, however, provided reliable results for both ground-level ($R^2 = 0.7784$) and HSI2 ($R^2 = 0.7794$) imagery, and was less affected by atmospheric factors. This is relevant because determining a robust atmospheric correction and HAB quantification technique will increase the efficiency of the analysis of HSI2 data.

5.0 Varimax-Rotated Principal Component Analysis (VPCA) Decomposition Method

5.1 VPCA Application to MODIS Data

Collaborator, J. Ortiz (KSU) has developed a method using visible derivative spectroscopy to separate the contribution of cyanobacteria, algae, suspended sediment, and colored dissolved organic matter (CDOM) from visible remote sensing images (Ortiz et al., 2013; Ali et al., 2016; Ali and Ortiz, 2014; Ali et al., 2014a). This approach differs from traditional band ratio methods (Witter et al., 2009; Ali, Witter, and Ortiz, 2014a and 2014b) in that all of the spectral information available with the visible part of the spectrum is employed. Derivative spectroscopy isolates the diffuse component of the reflectance signal, which carries the signature of the in-water constituents from the specular component, which does not (Ortiz et al., 2013). The correlation matrix of the derivative spectra is then decomposed using varimax-rotated, principal component analysis (VPCA), yielding orthogonal components that partition the relative contribution of the in-water constituents in space and time. There are several outputs from the method. The variance explained provides a measure of the total amount of variance in the image hypercube that is captured by the decomposition. The communality represents the amount of information explained on a band-by-band basis. The spectral shapes or component loadings vary as a function of wavelength and can be used to identify the constituents when compared with independent spectral

libraries. Finally, the method provides spatial patterns, images of component scores that show the geographic distribution of each constituent (Ortiz et al., 2013).

High-resolution spectra from an ASD, Inc., LabSpec® Pro Full Resolution (FR) spectrometer can be used to identify the composition of the particulates extracted from water samples collected at the field sites (Fig. 5.1). To see how noncontinuous, multispectral sensors with band gaps alter the continuous hyperspectral signal, the hyperspectral signal is averaged to the multispectral resolution of sensors such as MODIS. This approach demonstrates that the signals extracted from MODIS can be matched to the resampled hyperspectral signals with $R \geq \pm 0.90$ depending on the components or mixtures of components present. Multispectral images can thus be reprocessed and interpreted using the high-resolution data from field or aerial hyperspectral sensors to guide image interpretation (Fig. 5.2). This approach will be useful to optimize information from existing assets such as MODIS, allowing more information to be extracted than can be done using traditional band ratio methods.

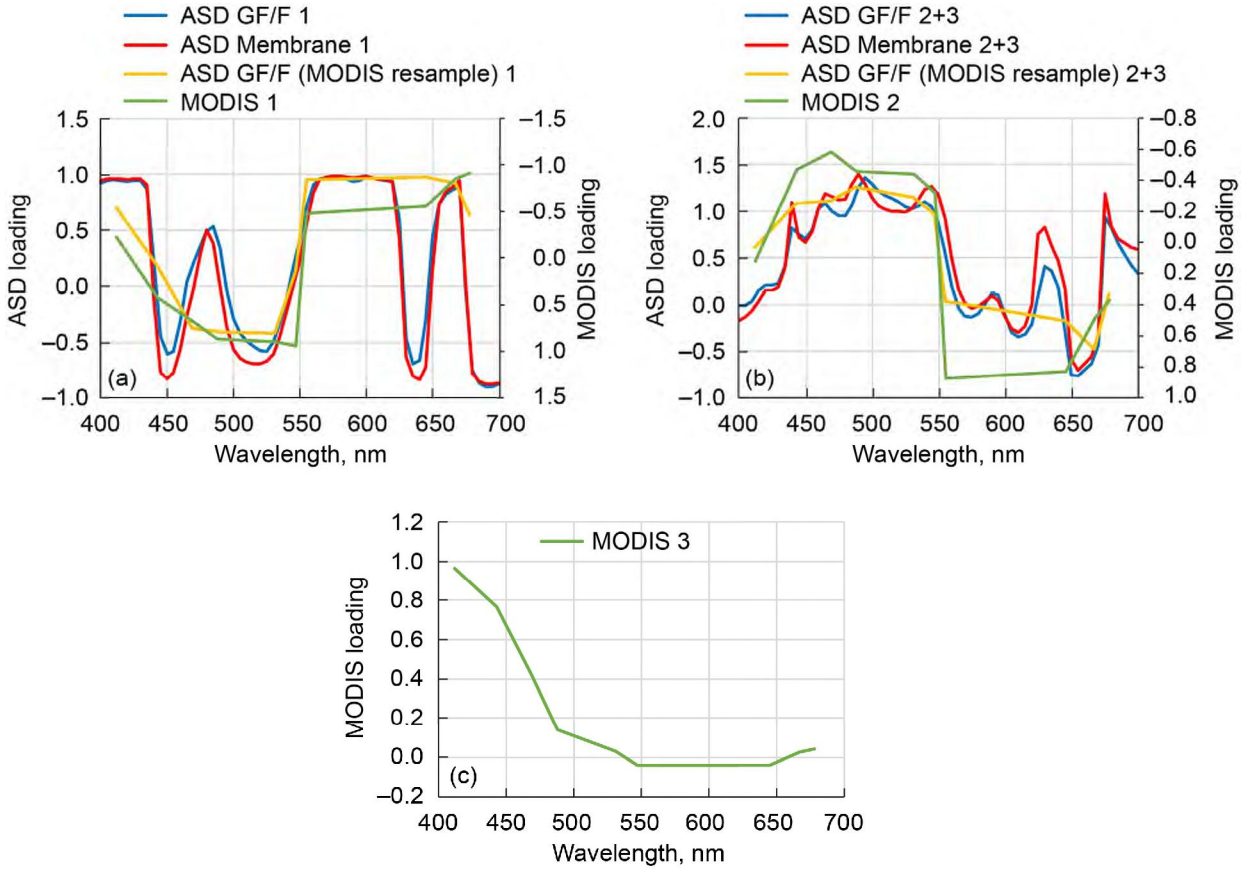

Figure 5.1.—Varimax-rotated principal component analysis (VPCA) spectral shapes extracted from filtered water samples (GF/F: glass fiber filter; Membrane: membrane filters) measured on ASD Labspec Pro FR Spectrometer system (Avouris et al., 2015) are plotted at full resolution and MODIS resolution for comparison with VPCA components extracted from MODIS (Moderate Resolution Imaging Spectroradiometer) image of Western Basin. Left vertical axes for ASD hyperspectral components; right vertical axes for MODIS components; except for MODIS VPCA 3. (a) Comparison of components related to HAB conditions. (b) Comparison of components related to non-HAB conditions. (c) Component related to colored dissolved organic matter.

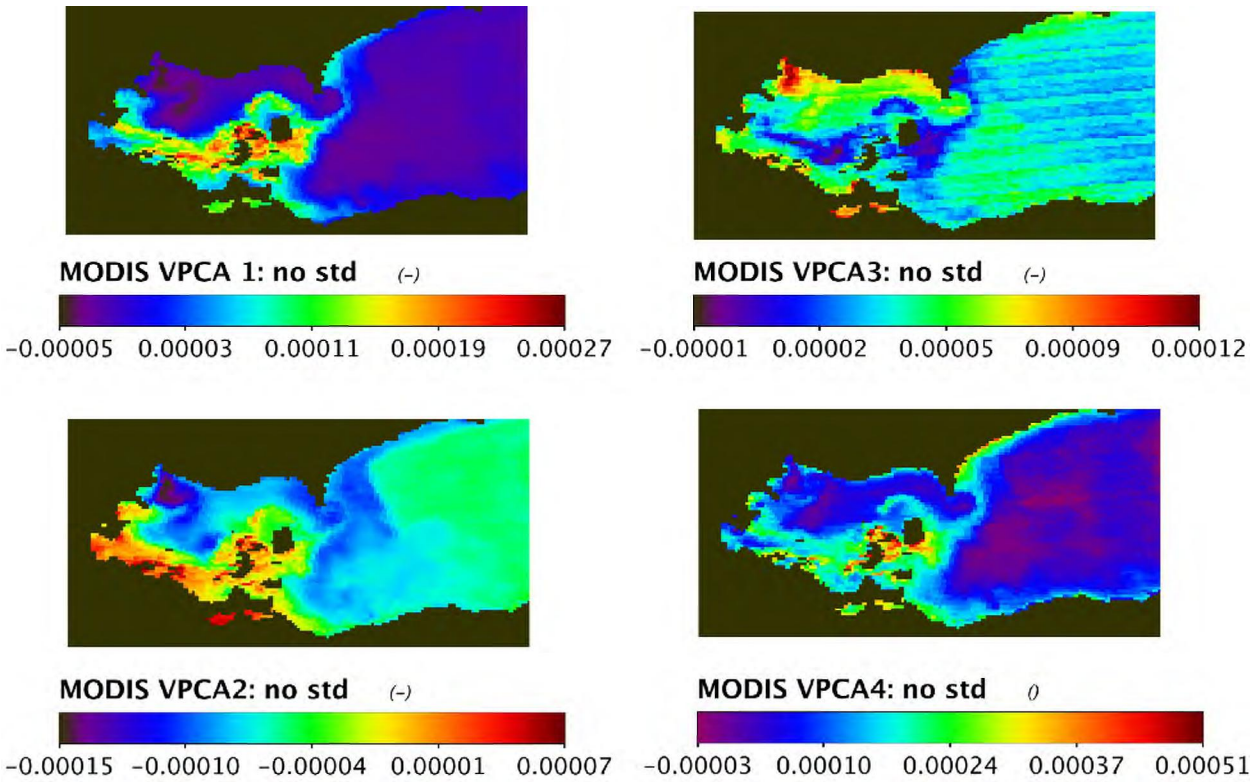

Figure 5.2.—Varimax-rotated principal component analysis (VPCA) decomposition of MODIS (Moderate Resolution Imaging Spectroradiometer) images of the Western Basin of Lake Erie (July 28, 2015).

The VPCA method is applied to MODIS images from July and September to illustrate the utility of the method, and present data from a July image as an example (Fig. 5.2). Cloud and land masking is based on SeaDAS Ocean Color products. The results document that four components can be extracted from MODIS, although the fourth component accounts for <1 percent of the variance in the image. The leading components measure the cyanobacterial abundance and look similar to the NOAA CI values published from the same-day MODIS data. The leading component shows plumes of cyanobacteria emanating from Maumee Bay and Sandusky Bay and flowing toward the Central Basin. The leading MODIS component patterns and resampled hyperspectral loading are correlated with $R = -0.90$. The second component is a mixture of algal and suspended sediment based on comparison with ASD FieldSpec® HH2 measurements. This combined component correlates with the corresponding MODIS component with $R = -0.92$. The second component has high concentrations (reds) along the southern coast of the Western Basin and Sandusky Bay. Intermediate-level values (yellows) are found in the Central Basin. The algal signal associated with this component is largely associated with eukaryotic diatoms and green algae, although some prokaryotic cyanobacteria is identified based on the presence of a phycocyanin peak, which is visible in the full-resolution spectrum (see Fig. 5.1).

The third component carries the CDOM signal. Notice that it is possible to view the CDOM-rich plumes emanating from the various rivers that feed into the Western Basin of Lake Erie. There is a scanline bias present in the third component, which arises from the MODIS blue reflectance bands. The leading three components account for approximately 98 percent of the variance in the Western Basin. They reflect orthogonal or independent measures of the variability within the image. The fourth component is minor, accounting for on the order of 0.5 percent of the variance in the image. This fourth component likely represents another mixture of minor algae and sediment present in the scene. The origin of this last component is an active area of research.

5.2 Application of KSU VPCA Decomposition to HSI2 Data

Joseph Ortiz (KSU) and his doctoral student, Dulci Avouris, using ENVI/IDL have now applied a varimax-rotated, principal component analysis decomposition to reflectance data from two of the 2015 HSI2 mirror-bearing swaths from Sandusky Stations and one swath in the Western Basin processed by MTRI using their blacktop-based vicarious calibration method. The empirical mirror-based reflectance calibration method the KSU group has developed in collaboration with Schiller and Luvall is described in section 3.3. This has enabled an initial comparison of the empirical mirror reflectance calibration method and MTRI's vicarious blacktop calibration method, although a more complete comparison must be conducted using data from the same swaths. The KSU spectral decomposition method works with ASD LabSpec® Pro FR, ASD FieldSpec® HH2, Landsat, MODIS and HSI2 data at this time (Avouris et al., 2015; Szell, Turner, and Ortiz, 2015). Thus far a leading component has been extracted from the HSI2 data that can be related to the CyanoHAB-forming bacteria. The results from the two different reflectance calibration methods compare favorably for the leading component (see Fig. 5.3). Work is still being done to determine the signals contained in the trailing components extracted from the HSI2 data. The current method of decomposition is conducted entirely in ENV/IDL using the 3D hypercube.

This is a major advance for the KSU methodology and represents the first time that the KSU VPCA analysis method has been coded up for use in ENVI/IDL. This advance increases the flexibility with which the method can be applied across sensor platforms. To verify the results of the analysis, two different test data sets (one image from MODIS and a data set composed of ASD FieldSpe HH2 spectra) is used to determine if the results from the analysis obtained with ENVI/IDL are consistent with the VPCA decomposition that we have previously employed using the IBM statistical analysis program SPSS with much smaller field-collected data sets. Results document that identical solutions are obtained using these two data sets when the data is preprocessed and postprocessed in the same way. Using SPSS was a viable option for the field data sets, which represent files that are orders of magnitude smaller than the HSI2 data sets. The visible portions of the HSI2 data sets being working with are on the order of 20 GB of data per swath. The ability to apply the VPCA solution using ENVI/IDL provides much greater flexibility in terms of remote sensing image analysis.

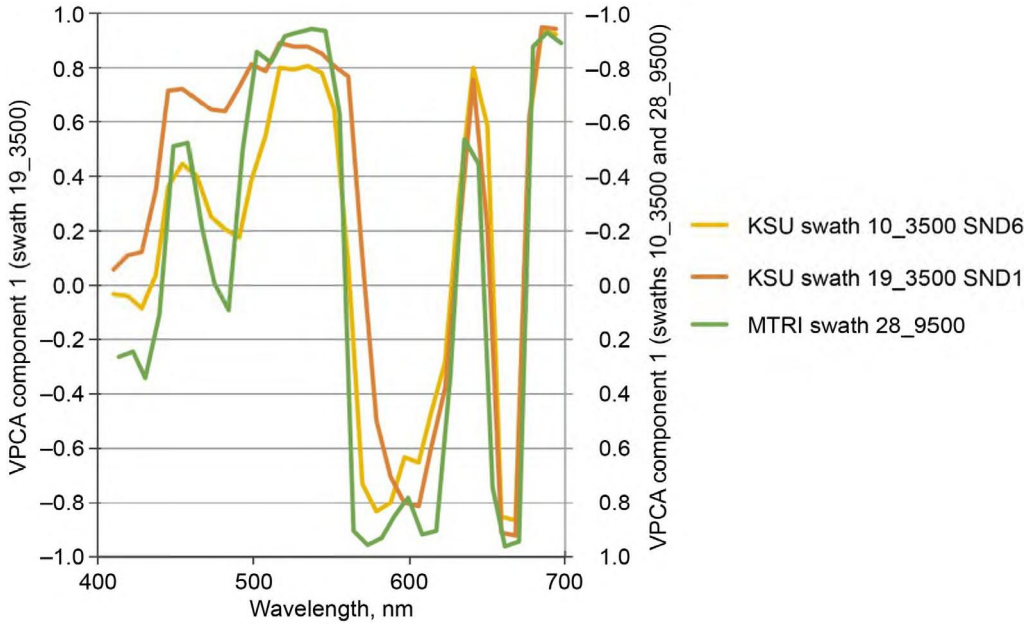

Figure 5.3.—The leading varimax-rotated principal component analysis (VPCA) component-loading pattern extracted from three HSI2 swaths: (1) Swath 10_3500 at Kent State University (KSU) station SND6 collected on September 18, 2015, (2) Swath 19_3500 at KSU station SND1 collected on September 18, 2015, and (3) Swath 28_9500 collected in the Western Basin on July 20, 2015.

The steps in the analysis of the 2015 HSI2 data for each HSI2 are listed in Table 5.1 and described in this section. The uncorrected reflectance ratio obtained from the lake radiance and mirror radiance must be corrected for the dispersion of light by the convex mirror. This is achieved by dividing the uncorrected HSI2 reflectance spectra by the observed surface reflectance ratio measured relative to that of a white Spectralon plate using an ASD Fieldspec® HH2 (interpolated to the native spectral resolution of the HSI2 sensor) operated at the same location. This yields an empirical mirror gain function. Example reflectance values from selected bands in the SND1 and SND6 swaths are plotted in Figures 5.4 and 5.5.

TABLE 5.1.—MIRROR–BASED REFLECTANCE CALIBRATION ANALYSIS STEPS

(1) Obtain the subset of the swaths that include overflights with ground-based measurements conducted by the KSU team on either the Sandusky transect or the Central Basin Coastal Zone Transect.
(2) Identify the location of the research vessel and floating mirror target in the swath.
(3) Extract and average the pixels associated with the mirror target and lake pixels near the mirror target.
(4) Calculate an uncorrected lake surface reflectance from the ratio of the HSI2 lake radiance to the uncorrected mirror radiance as measured by the HSI2.
(5) Obtain a mirror gain function for the HSI2 by dividing the uncorrected reflectance measured by the HSI2 using Spectralon-referenced field measurements obtained from coincident field data collected from the same station.
(6) Use the mirror gain function to correct the radiance or reflectance measurements from the swath.

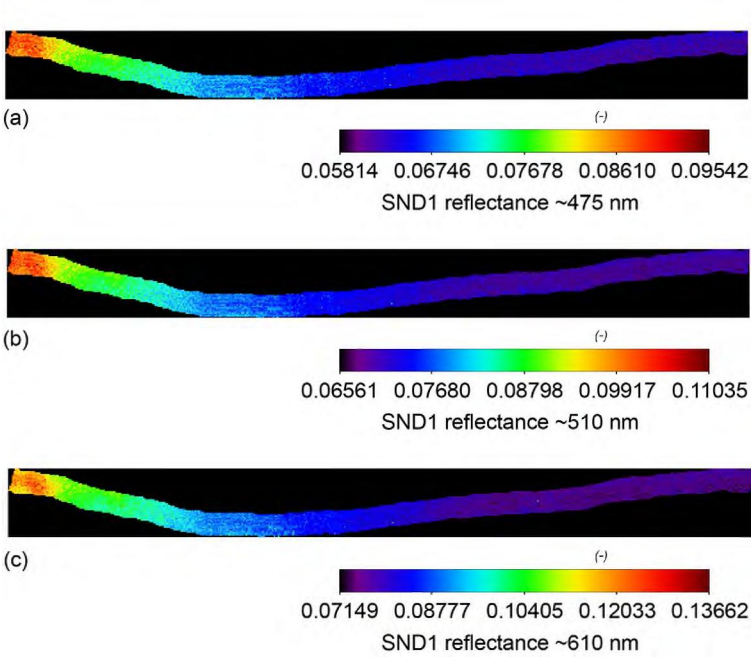

Figure 5.4.—HSI2 reflectance values from selected bands in swath SND1 on September 18, 2015, from Sandusky Bay. (a) Band 8, ~475 nm. (b) Band 12, ~510 nm. (c) Band 28, ~650 nm.

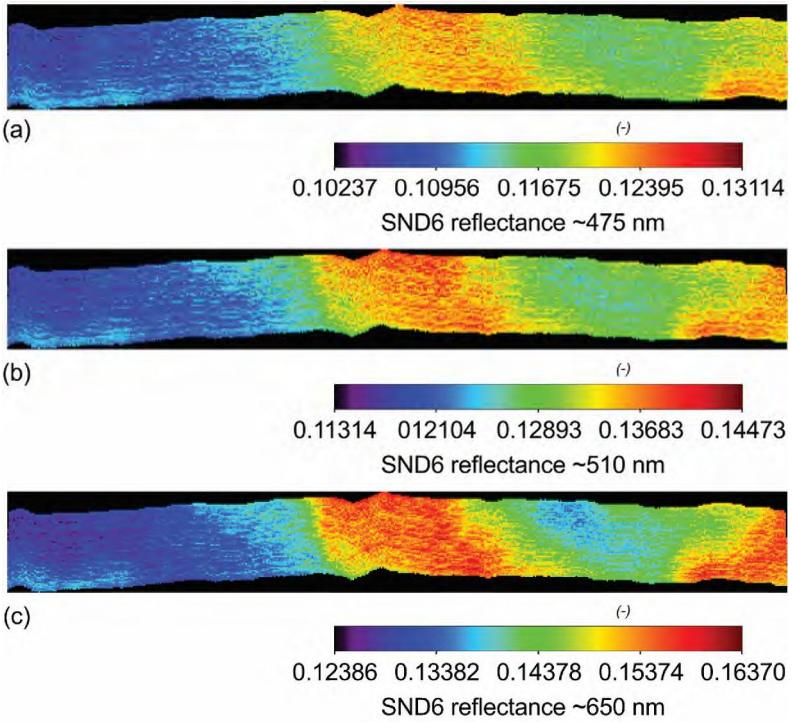

Figure 5.5.—HSI2 reflectance values from selected bands in swath SND6 on September 18, 2015, from Sandusky Bay. (a) Band 8, ~475 nm. (b) Band 12, ~510 nm. (c) Band 28, ~650 nm.

For analysis of the HSI2 swaths from SND1 and SND6, we extract the visible part of the radiance spectrum from the swath and calculate reflectance, which calibrates the HSI2 to reflectance derived from an ASD white Spectralon plate. Example reflectance spectra are plotted in Figure 5.6(a) and (b). To increase the signal-to-noise ratio (SNR), each three adjacent bands are averaged and assigned the wavelength of the central band (Fig. 5.6(c) and (d)). The band-averaged visible reflectance spectra are then converted to first derivative spectra (Fig. 5.6(e) and (f)). The correlation matrix based on these first derivative spectra is then decomposed using the PCA algorithm from ENVI/IDL. The resulting PCA component loadings are then imported to IDL to be further rotated using a varimax-rotation algorithm. The leading VPCA component scores are then plotted using ENVI (Figs. 5.7 and 5.8).

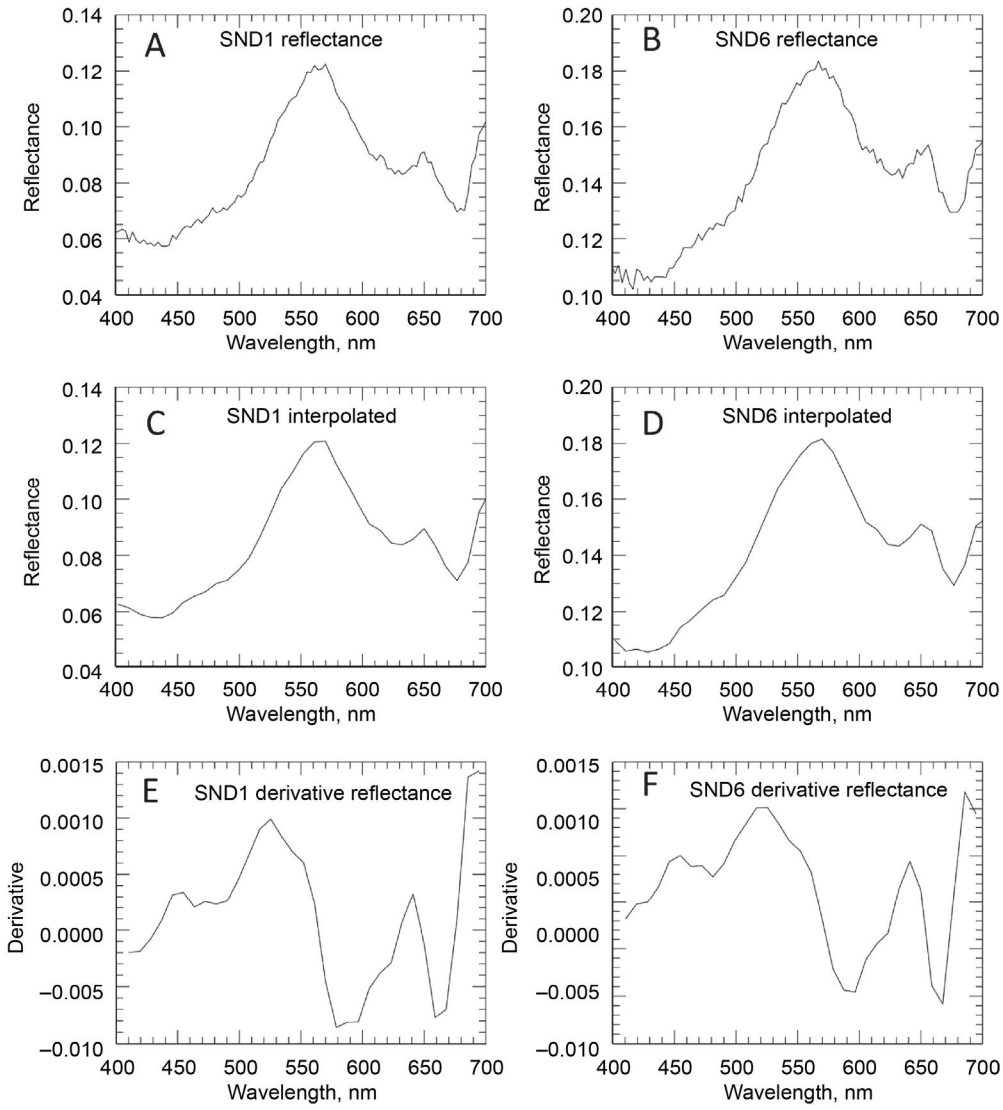

Figure 5.6.—Example spectra extracted from HSI2 swaths SND1 on September 18, 2015, and SND6 documenting preprocessing steps in Kent State University (KSU) varimax-rotated principal component analysis (VPCA) decomposition method. A and B show reflectance spectra from SND1 and SND6 swaths calculated using the empirical mirror reflectance calibration method. C and D show three-channel, band-averaged, HSI2 reflectance spectra for SND1 and SND6 at ~9 nm resolution. E and F show center-weighted derivative spectra for SND1 and SND6 calculated from the band-averaged spectra.

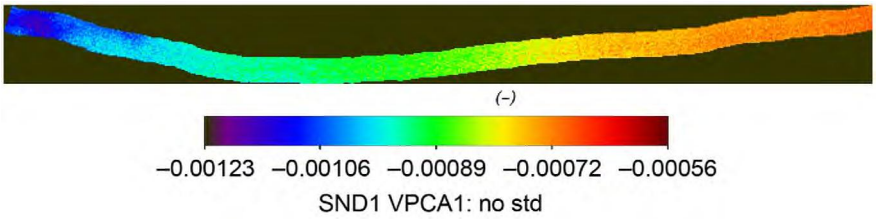

Figure 5.7.—Spatial pattern of leading varimax-rotated principal component analysis (VPCA) component scores from HSI2 swath SND1 on September 18, 2015.

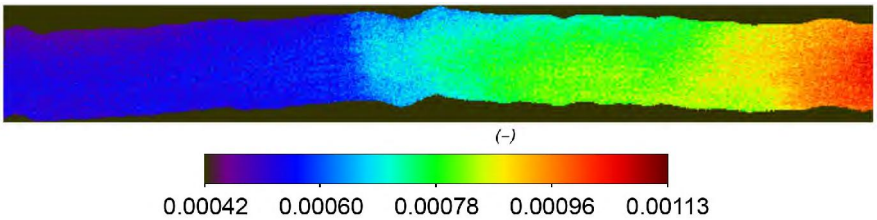

Figure 5.8.—The spatial pattern of leading varimax-rotated principal component analysis (VPCA) component scores from HSI2 swath SND6 on September 18, 2015.

5.3 VPCA of the 2015 HSI2 Data Using the MTRI Blacktop Calibration Method

For comparison with results from other groups and to document that the KSU spectral decomposition method can be applied to reflectance spectra obtained from other methods, this method to one of the swaths from near the MBSP calibration site that was processed by MTRI using their first-look, blacktop-based, vicarious calibration method. Figure 5.9 provides a plot of typical reflectance spectra and their derivative transform collected in Sandusky Bay and the Western Basin from the 2014 ASD FieldSpec® HH data set for comparison with the HSI2 spectra converted to reflectance using the empirical mirror-based calibration method (Fig. 5.6) and the blacktop-based reflectance spectra (Fig. 5.9). The greatest difference between the two types of reflectance estimation methods is that the blacktop method appears to yield higher reflectance on the blue end of the spectrum than the ASD Fieldspec® HH2 data or the mirror-based reflectance calibration method. Despite this difference, the shapes of the first derivative spectra are similar from the two methods (compare Fig. 5.6, spectrum F, and Fig. 5.10, spectrum C). This provides documentation that the derivative transform helps to remove potential bias from the reflectance spectra that can arise, for example, from variations in the diffuse-to-global ratio. Although methods based on band ratios may be sensitive to far-field variations in reflectance values, the close spacing of the derivative calculation acts as a high-pass filter to remove the low-frequency part of the reflectance spectrum that is sensitive to specular reflectance, thus boosting the signal from the diffuse component.

The leading VPCA component of the HSI2 swath obtained from the Western Basin exhibits more structure than the two swaths analyzed from Sandusky Bay (Fig. 5.11). This image was obtained from a time when there was a considerable surface bloom. The component loadings of the leading component from the decomposition of the Western Basin swath is similar to the components extracted from the Sandusky Bay swaths.

These results document the significant progress that have been made in analysis of HSI2 data collected during the 2015 field season. Future plans entail refining the application of the mirror calibration method, and to make use of Rayleigh scattering corrections and a cloud masking procedure developed at KSU or provided by one of the other groups as additional preprocessing steps prior to VPCA decomposition of the HSI2 data. The results presented here should be helpful to NASA Glenn as when planning for development and deployment of the HSI3.

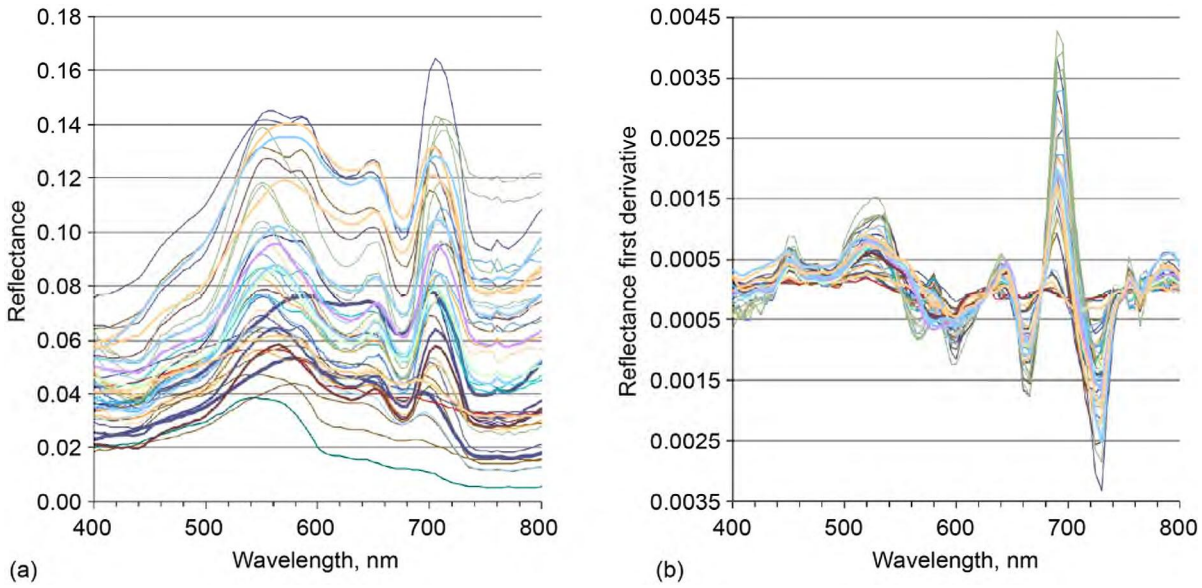

Figure 5.9.—2014 Kent State University (KSU) ASD, Inc., Fieldspec® HandHeld 2 reflectance relative to Spectralon and its first derivative transform from Western Basin and Sandusky Bay.

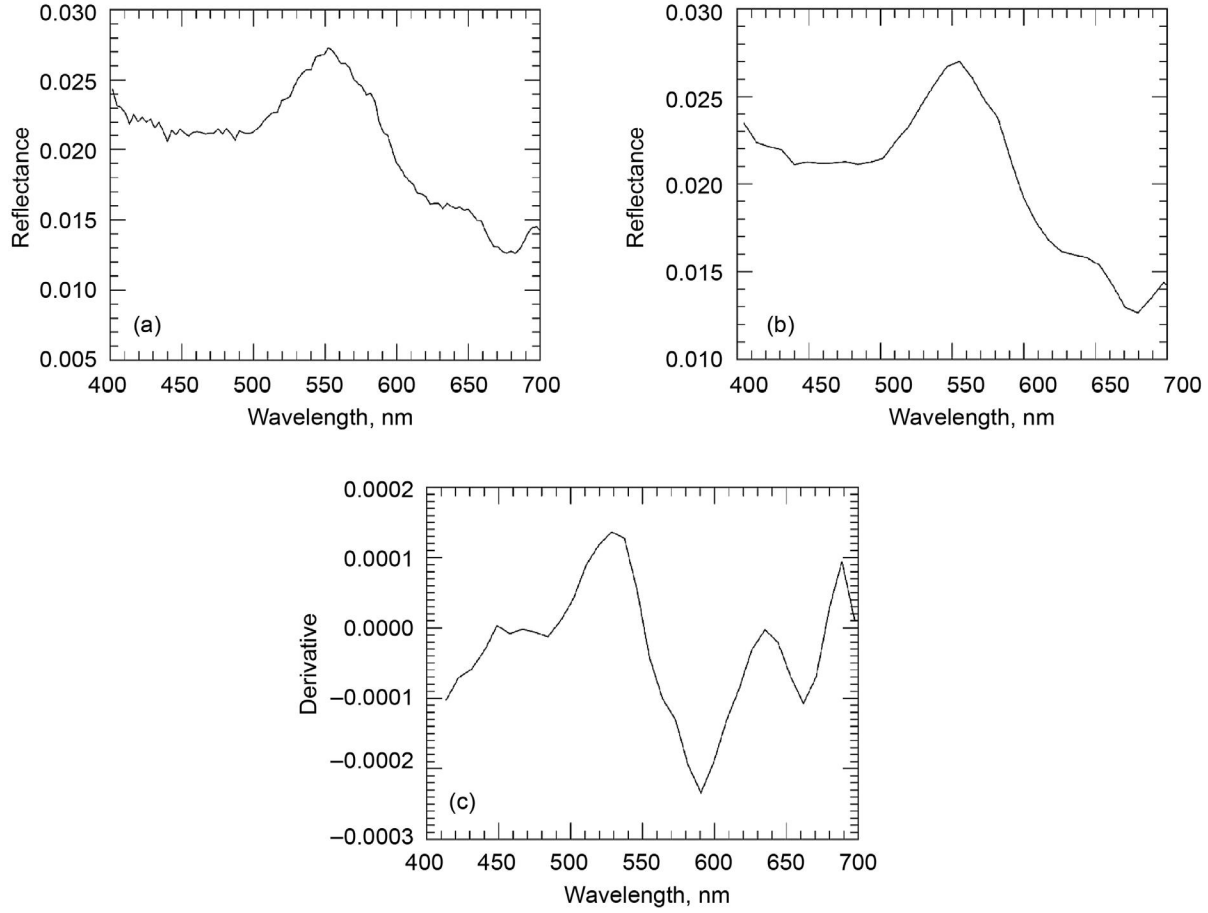

Figure 5.10.—Example spectra extracted from Michigan Technological Research Institute (MTRI) reflectance-processed swath 28 9500 on July 20, 2015. (a) Reflectance spectra calculated using MTRI vicarious calibration. (b) Three-channel, band-averaged HSI2 reflectance spectra with ~9 nm resolution. (c) Center-weighed derivative spectrum calculated from band-averaged spectra.

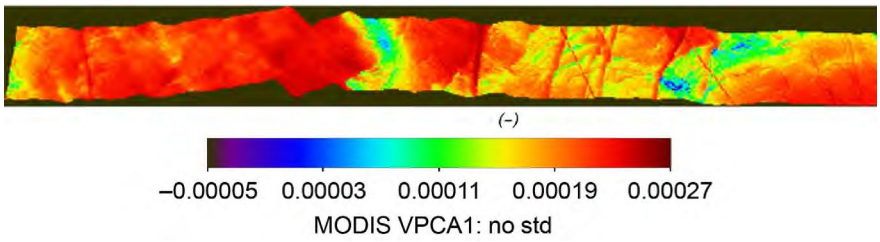

Figure 5.11.—Spatial pattern of leading varimax-rotated principal component analysis (VPCA) component scores from HSI2 swath 28 9500.

6.0 Impact to PACE and HyspIRI Mission Development and Applications for Aquatic Processes

The hyperspectral algorithms used to identify HAB species within phytoplankton communities developed by Joseph Ortiz funded in part by the NASA Glenn HSI project will contribute significantly to the product development for two future NASA satellite missions, PACE (Pre-Aerosols, Clouds, and ocean Ecosystems) and HyspIRI (Hyperspectral Infrared Imager). Impact to PACE and HyspIRI mission development and applications will be achieved by utilizing the measurement processes developed here to improve aquatic constituent products for coastal and inland case II waters.

The PACE mission will provide ocean color measurements using an advanced optical instrument, the ocean color imager (OCI), designed to provide hyperspectral ultraviolet (UV) to visible (VIS) and near-infrared (NIR) as well as multispectral short-wave infrared (SWIR) observations of the world's pelagic and coastal ecosystems. All measurement bands will have a spatial resolution of 1 km^2 (square pixel at nadir) with 2-day global coverage (National Academy of Sciences, 2007; Science Definition Team, 2012).

The HyspIRI mission will provide hyperspectral visible to SWIR and multispectral thermal data products to NOAA that would significantly enhance their ability to predict when algal blooms will occur, whether or not they are toxic, and their impact on human health.

The 30-m resolution hyperspectral data and its 19-day repeat provided from HyspIRI will allow spectroscopy at a spectral accuracy of <0.5 nm and an absolute radiometric accuracy of >95 percent from water surfaces. These data would significantly enhance the ability to identify the toxic cyanobacteria species and subspecies along with their distribution within the water column and the spatial variability in the surface waters throughout the Great Lakes.

HyspIRI's thermal IR multispectral data will also have 60-m spatial resolution, but a 5-day repeat pattern that greatly enhances the ability to obtain timely and adequate thermal data. HyspIRI's NEdT (Noise Equivalent delta Temperature) precision of <0.2 K will produce day-night pairs of calibrated surface temperatures for use in determining surface water temperature. The combination of both the VIS-SWIR and thermal wavelengths will significantly enhance the ability to identify the toxic cyanobacteria species and provide water temperature to help understand the HAB population dynamics.

The significance of having algorithms available to process the hyperspectral data from these missions is clearly stated in the 2015 HyspIRI Aquatic Studies Group white paper: The PACE and HyspIRI missions will provide the scientific community with hyperspectral observations that will lead to a more robust chl-a product as well as the opportunity to detect various accessory pigments that can be utilized to identify bio-geochemically important phytoplankton functional types (PFTs). Understanding the spatial and temporal distribution of PFTs will allow the scientific community to improve its knowledge of biologically mediated fluxes of elements that contribute to the carbon cycle (Falkowski et al., 2004). Information on biodiversity provides a valuable quantitative database for structuring sophisticated predictive models that include taxonomic phytoplankton community information such as size spectra, probability distributions of certain taxa, and upper trophic level estimations such as fisheries productivity (Chesson and Case, 1986; DeAngelis and Waterhouse, 1987; Chase et al., 2013). Determining the spatial variability and concentrations of various PFTs is critical to improving primary productivity estimates and

understanding the feedbacks of climate change (Moisan, Moisan, and Linkswiler 2011). Hyperspectral techniques that can enhance the discernment of subtle features in hyperspectral data could also enable the detection of marker pigments.

To spectrally detect marker pigments, the total absorption is first retrieved from the measured reflectance using an algorithm (e.g., based on inversion of a water-column radiative transfer model), and then the total absorption is separated into absorption by individual end members. High-resolution reflectance spectra will facilitate the retrieval of total absorption at high resolution. This will lead to better discrimination between relative concentrations of photosynthetic and photoprotective pigments, which serve as taxonomic marker pigments and provide a proxy for the physiological function of the phytoplankton community (HyspIRI Aquatic Studies Group, 2015).

7.0 Conclusions

This cooperative research effort in harmful algal bloom (HAB) hyperspectral sensing in Lake Erie, which comprise Federal and State organizations as well as academic institutions, has had numerous accomplishments as detailed in this report. The team has assembled one of the most—if not the most—comprehensive sets of airborne hyperspectral measurements with coincident in situ data. The data set has been integrated through the creation of a centralized relational database, and all HSI2 data is archived at the Ohio Supercomputer Center. Weekly flights and in situ sampling of the same body of water over an approximate period of 4 months will allow for very unique insights into how the greater research community can use hyperspectral data to better characterize water quality. Findings from this exercise have very real implications for the future of aquatic remote sensing at NASA, specifically toward the development and implementation of the PACE (Pre-Aerosols Clouds and ocean Ecosystems) mission.

The project focused on improving remote sensing capability for accurately detecting potential HABs through research towards better atmospheric correction of remote-sensed data from a hyperspectral imager HSI2, advanced algorithms for extracting more information from the data, and a number of systematic improvements in data processing. The next-day Quicklook HAB processing activity was successful in rapidly turning raw airborne imagery into informative data products for use by water resource managers and other decision makers. The streamlined process included geometric and radiometric correction (NASA Glenn), followed by atmospheric correction algorithm implementation, and product reporting (Michigan Technological Research Institute).

The project has explored several strategies for atmospheric correction of the HSI2 data, of which the most positive results were obtained from several vicarious calibration methods, such as the empirical line method and the empirical mirror-based calibration method. Theoretical calculations (South Dakota State University) provide a sound basis for the effectiveness of the empirical mirror-based calibration method. The varimax-rotated principal component analysis (VPCA) spectral decomposition method (Kent State University) has been applied successfully to NASA HSI2 data, and the results show that it is relatively insensitive to the choice of reflectance calculation method. This provides a means of comparison between sensors of variable spectral, spatial, and temporal sampling that will prove helpful for evaluation of future hyperspectral missions.

In the upcoming years the research group plans to build upon these advances, further transitioning the task of monitoring the Lake Erie algal blooms to the National Oceanic and Atmospheric Administration (NOAA) Great Lakes Environmental Research Laboratory (GLERL) and providing data products for inclusion into the NOAA HAB bulletin. The project seeks to further improve data delivery as well as the research into atmospheric correction and improved algorithms; for example, operationally test the VPCA algorithm and also focus research on real-time atmospheric correction. Some potential areas to improve data dissemination include development of a better method to share comprehensive data products produced from the HSI2 data and also creation of a centralized geospatial Web site where HSI2-derived products and in situ data can be accessed. Finally, plans are to provide this comprehensive set of information and remote sensing techniques to the larger research community in order to improve the monitoring and understanding of algal blooms in complex inland and coastal waters.

Appendix A.—Field Methods

This Appendix contains information on the field methods utilized by the University of Toledo (UT) and Michigan Technological Research Institute (MTRI).

A.1 University of Toledo Field Methods

A.1.1 Sampling Sites

Seventeen sampling sites in Lake Erie's Western Basin were used during the course of sampling in the 2014 and 2015 field seasons (Fig. 3.5). Reflectance data were used in conjunction with water samples and measured algae concentrations for the verification of the calculated cyanobacteria index (CI) as suggested by Wynne et al. (2010), and phycocyanin concentrations ([PC]) as suggested by Simis, Peters, and Gons (2005). They are also used as ground reference for the atmospheric correction techniques of airborne imagery. Additional samples were taken at the Maumee Bay State Park (MBSP) beach and south parking lot for light and dark references to optimize gain. Exact geographic locations of these sites can be found in Table A.1. MBSP beach spectra were taken starting at the specified coordinates, and again every 30 m for the length of the beach. The south parking lot spectra were taken starting at the specified coordinates and taken at the center of every third parking space.

Figure 3.5.—Study area of Lake Erie Western Basin.

TABLE A.1—CONSTANTS AND COEFFICIENTS USED IN SIMIS ALGORITHM

Location	Latitude	Longitude
CRIB/EW1	41.68966	–83.2713
SE2	41.72582	–83.1813
4P	41.7498	–83.1037
7L1	41.78003	–83.0428
7L	41.816	–83
7L2	41.82708	–83.098
GR1	41.82082	–83.1845
NW2	41.8058	–83.2714
8M	41.78947	–83.357
SW1	41.7656	–83.3794
MB18	41.74242	–83.4014
MB19	41.72715	–83.4323
MB20	41.71563	–83.4548
SW2	41.75536	–83.3542
7M/EW3	41.7332	–83.297
EW2	41.715	–83.278
EW4	41.728	–83.336
EW5	41.725	–83.37

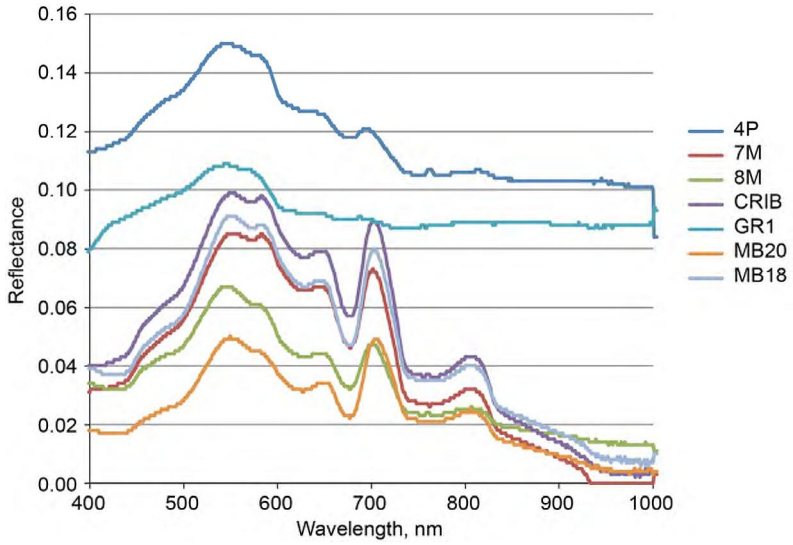

Figure A.1.—Example on-lake reflectance acquired on August 15, 2014, Lake Erie sampling trip. Figure 3.5 shows location of each site.

A.1.2 On-Lake Data Collection

The optical instrumentation used to collect ground validation samples is the ASD, Inc., FieldSpec® 3 Spectrometer, which operates at a spectral resolution of 3 nm. With a 10° optic field of view, this device collects reflectance data from the water surface unhindered by atmospheric interference. Prior to collection, gains are optimized using a white reference target, and a dark current measurement is recorded. A standard 100 percent white Spectralon (Calibrated Diffuse Reflectance Target, Labsphere, Inc.) is measured to approximate downwelling irradiance for reflectance calculations. For each sampling location, eight sets of 30 reflectance measurements are recorded. The white reference target is remeasured to assess any change in ambient light field. The data are used as ground reference to verify the atmospheric correction. An example of these data is in Figure A.1.

In addition to the ASD measurements, a number of other samples and measurements are taken at each site. These include photosynthetically active radiation (PAR), sonde depth profiles, Secchi depth, temperature, phytoplankton tows, and water samples to be further analyzed in the UT Lake Erie Center (LEC) laboratory (Bridgeman, 2012).

For each of these sampling trips, as close to concurrent with hyperspectral imager (HSI) acquisitions as possible, water samples from up to 17 sampling locations were obtained. Basic water chemistry parameters are to be measured, including vertical profiles of temperature (°C), conductivity ($\mu S\ cm^{-1}$), photosynthetic photon flux density ($\mu E \cdot m^{-2} \cdot s^{-1}$), dissolved oxygen ($mg \cdot L^{-1}$), turbidity (NTU), chlorophyll-a (chl-a) concentration (from standardized relative fluorometric unit conversions), and phycocyanin concentration (from standardized fluorometric unit conversions) using a YSI6600 multiparameter sonde.

These field activities were conducted on the following dates in 2014:
7/25/14, 8/07/14, 8/15/14, 8/28/14, 9/15/14, 9/18/14 (no chl-a samples), and 9/28/14.

Field activities were conducted on the following dates in 2015:
6/5/15, 6/15/15, 7/1/15, 7/20/15, 7/27/15, 8/4/15, 8/10/15, 8/11/15 (MBSP only), 8/17/15, 9/8/15.

A.1.3 Airborne Remotely Sensed Imagery

The NASA HSI2 provided airborne remotely sensed data used in these applications. The imager is attached to the base of an aircraft which is flown over select areas of Lake Erie's Western Basin, attempting to target our seven sampling sites. The aircraft collected imagery at altitudes between 915 m (3000 ft) and 3050 m (10 000 ft), with a spatial resolution between 2 and 10 m. Spectral resolution for the data is 3 nm, which is the same as the data collected using the ASD spectroradiometer, allowing for easy comparison.

To provide comparisons with an orbital sensor at a different scale, the 2014 data were complimented with data collected from the Hyperspectral Imager for the Coastal Ocean (HICO) sensor aboard the International Space Station. This instrument orbits continuously and so provides a regular stream of data on the lake's surface, but that data come at a coarser resolution than HSI2 data. HICO data are collected at a 5.7-nm spectral resolution over 87 bands ranging over the wavelengths of 380 through 960 nm (Oregon State University, 2009). The potential to be able to correct this imagery using the same atmospheric correction methods as with the airborne HSI2 can provide a much more robust collection of images of the lake surface with which to calculate pigment and algae concentrations, greatly reducing cost and time.

A.1.4 Laboratory Analysis

Chlorophyll-a, phycocyanin, total suspended solids (TSSs), and total volatile solids (TVSs) in water samples were analyzed at UT. A total of 169 samples were analyzed. Water samples taken at each ASD sampling station were analyzed in the LEC laboratory in order to determine aquatic parameters such as TSS, TVS, chl-a concentrations, and flouroprobe readings. Measurements are then taken of the amounts of green algae, blue-green algae, diatoms, cryptophyta, as well as colored dissolved organic materials (reported as "YS error" by probe) using a bbe FluoroProbe (bbe Moldaenke GmbH) calibrated against a standardized natural population of Lake Ontario phytoplankton (Bridgeman, 2012). Total concentration of these suspended organics is then calculated for each site.

The TSS measurements are taken using a vacuum filtration system where water from each sample site is run through a glass-fiber filter until the filter has become saturated with the nondissolvable solids so liquid can no longer pass through. The amount of water that passed through the system is recorded, and then the filter is dried, weighed, combusted, and weighed again to determine the mass of the suspended particles which remained on the filter. The measurements for the TVSs use the same procedure.

Laboratory analyses were carried out at the Western Lake Erie Limnology Laboratory at the University of Toledo Lake Erie Center, headed by Dr. Thomas Bridgeman. Chlorophyll-a (chl-a) concentrations were obtained by filtering water through glass-fiber filters, which were then dehydrated and frozen before separating the chl-a. When the chl-a had been separated from the filter, it then could be studied using a Turner fluorimeter (Bridgeman, 2012). Quality assurance procedures and multiple-laboratory comparison analysis are described in Golnick et al. (2016). Vertical zooplankton tows were also collected and later analyzed with the use of a stereomicroscope. Similarly, phytoplankton samples collected were analyzed under a compound microscope, and the species present were identified and recorded. Table A.2 shows the type of algae abundance data collected.

A.2 MTRI Field Methods

Routine field sampling was conducted by Michigan Technological Research Institute (MTRI) in 2015 in support of the NASA Glenn HSI HAB monitoring program. MTRI conducted weekly sampling at seven stations throughout the Western Basin of Lake Erie beginning in May and ending in mid-October (see Fig. A.2 for sampling locations). Efforts were made to conduct field sampling coincident with NASA HSI2 overflights when weather was permitting for small boat operations. Table A.3 is a summary of 2015 MTRI sampling dates and locations.

TABLE A.2.—ALGAE ABUNDANCE DATA COLLECTED AUGUST 15, 2014

Site name	[Measured specimen concentrations.]				
	Chl-a, ug/L	Green algae, percent	Bluegreen algae, percent	Diatoms, percent	Cryptophyta, percent
GR1	6.7677	26	22	36	15
4P	12.255	0	41	1	59
8M	19.51	0	56	2	42
7M	50.605	0	66	0	34
CRIB	55.592	0	68	0	32

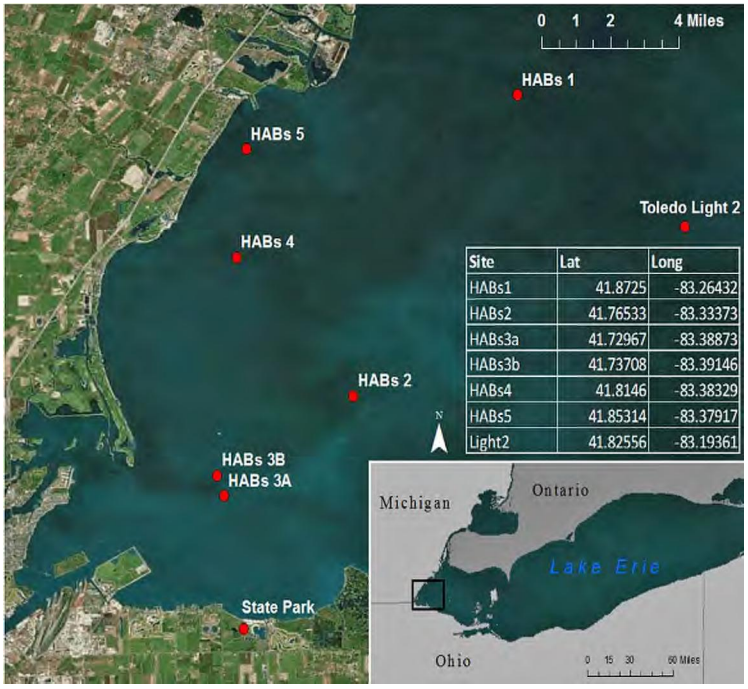

Figure A.2.—Michigan Technological Research Institute (MTRI) 2015 harmful algal bloom (HAB) sampling stations. Image from ArcGIS (Environmental Systems Research Institute, Inc.).

TABLE A.3.—SUMMARY OF MICHIGAN TECHNOLOGICAL RESEARCH INSTITUTE (MTRI) SAMPLING FREQUENCY FOR 2015

Date	Sites[a]
5/1/2015	1, 2, 3a, 3b, 4, 5
5/21/2015	1, 2, 3a, 3b, 4, 5
6/5/2015	1, 2, 3a, 3b, 4
6/19/2015	1, 2, 3a, 3b, 4
7/2/2015	5
7/10/2015	1, 2, 3a, 3b, 4, 5, TL2
7/20/2015	1, 2, 3a, 3b, 4, 5
7/27/2015	1, 2, 3a, 3b, 4, 5
8/11/2015	1, 2, 3a, 3b, 4, 5, TL2
8/17/2015	1, 2, 3a, 3b, 5, TL2
8/27/2015	1, 2, 4, 5, TL2
8/31/2015	1, 2, 3a, 3b, 4, 5
9/11/2015	2, 4, 5
9/17/2015	1, 2, 3a, 3b, 4, 5
9/25/2015	2, 3a, 3b, 4
9/28/2015	1, 2, 3a, 3b, 4, 5
10/5/2015	1, 2, 3a, 3b, 4, 5, TL2
10/22/2015	1, 2, 3a, 3b, 4, 5

[a]TL2 refers to the Toledo Light 2 station (see Fig. A.2).

At each site a suite of measurements were made, including spectral reflectance, phytoplankton composition, and water clarity. Spectral reflectance measurements were made using an ASD FieldSpec® spectrometer. Reflectance measurements were made using an 8-degree field-of-view foreoptic to measure upwelling radiance from the target surface. Incoming solar energy was measured two ways: (1) using a calibrated ASD, Inc., Remote Cosine Receptor (RCR) to correct for downwelling irradiance, and (2) using a Spectralon panel to approximate downwelling irradiance. These two methods were used to provide data that are comparable to data from other researchers who employ different methods. Radiometric measurement geometries and sequences were used following the NASA Radiometric Measurements and Data Analysis Protocols document (Mueller 2003).

MTRI also collected radiometric data at MBSP on seven different occasions with NASA HSI2 overflights. These data sets were used to resolve an empirical line fit atmospheric correction factor to transform the HSI2 data to surface reflectance.

Phytoplankton composition profiles were measured using a bbe Moldaenke GmbH FluoroProbe lowered and raised through the water column (factory calibration). The fluoroprobe has six excitation wavelength LEDs (370, 470, 525, 570, 590, 610 nm) to determine different algae class contribution to total chlorophyll-a. Water samples were also made (surface grab) at each site and were filtered using 0.7-μm Grade GF/F filter pads in the laboratory for analysis of chlorophyll, phycocyanin, and HPLC pigments. The results of these analyses are not yet available.

Other environmental parameters were collected at each station including Secchi depth, air and water temperature, sky conditions, and wave height. When present, surface-scum thickness was also measured.

Appendix B.—Summary of Previous Years NASA Glenn Airborne Hyperspectral Monitoring of HABs

The collaboration between NASA Glenn and the National Oceanic and Atmospheric Administration (NOAA) Great Lakes Environmental Research Laboratory (GLERL) began in 2006 where the first Glenn HSI was utilized for flight operations with NOAA in situ measurements. The results from this early flight testing found the signal-to-noise ratio (SNR) of the first imager to be inadequate. This imager was redesigned, and a second imager was built and deployed beginning in 2007. This imager was found to have adequate SNR. During the second field study, in situ reflectance data were obtained from the Research Vessel Lake Guardian (an Environmental Protection Agency vessel) in conjunction with reflectance data obtained with the hyperspectral imager from overflights of the same locations. A comparison of these two data sets shows that the airborne hyperspectral imager closely matches measurements obtained from instruments on the lake surface and thus positively supports its utilization for detecting and monitoring harmful algal blooms (HABs).

The second-generation imager was flown in 2007 in conjunction with a monitoring cruise of the Research Vessel Lake Guardian. During this cruise, water samples and radiometric measurements were made of the lake at multiple locations. The radiometric measurements made from the Lake Guardian included spectral measurements of downwelling irradiance and water-leaving radiance. From the ratio of the water-leaving radiance and downwelling irradiance a spectral reflectance was obtained. In order to compare the capability of the aircraft HSI2 to accurately measure water reflectance, the HSI2 measurements were compared with the in situ measurements.

The primary application of the instruments was to demonstrate the capability of early HAB detection by detecting various concentrations of the pigment phycocyanin as an indicator. The second-generation HSI2 was used to gather data in conjunction with waterborne measurements. In general, the airborne measurements show very good agreement with the in situ measurements. The largest area of variance is in the HSI2 showing a higher reflectance of blue light than the in situ measurement. This, considered an issue with atmospheric correction in the early days of HSI studies (2014), has been addressed in the present study.

In 2009, flights were conducted to acquire concurrent water samples and overflight of 75 data points. This data, while not published, has allowed the evaluation of the capability of some of the different suggested techniques for HAB identification and concentration estimation.

In 2014, the Great Lakes Workshop Series on Remote Sensing of Water Quality laid the foundation for open collaboration in developing a regional working strategy for remote sensing, applications, and data management methods. One project that stemmed from the workshop was a collaborative effort of airborne remote sensing and in situ measurements by the following partners: NASA Glenn, NOAA GLERL, Michigan Technological research Institute (MTRI), University of Toledo (UT), Kent State University (KSU), and the U.S. Naval Research Laboratory. The first of three flights was conducted before Toledo had the drinking water ban due to microcystin being detected in the treated water. Once this occurred, the team changed plans to incorporate both monitoring and data acquisition for research purposes. In all, fifteen HSI2 flights were completed in 2014. Each of these flights covered 12 water intake locations distributed from Cleveland to Toledo. Also, pre-arranged water sample and study locations were overflown when there were in situ measurements being taken. More than 60 concurrent measurements were obtained. The hyperspectral data that were concurrently obtained with water sample data will be used for the evaluation of HAB algorithms. Figure B.1 represents a sample of the data obtained. The hyperspectral image was taken at Maumee Bay State Park on September 17, 2014. The color infrared image is georeferenced and has been overlaid on a Google Earth image. The aircraft motion causes the edges of the HSI2 image to be wavy.

Atmospheric correction was a challenge for providing data in a short time period. In order to provide indicators of algal blooms for the water intakes, reference data from deep-water locations, which did not contain sediment or algal indications, were obtained—the specific deep water location north of Cleveland, called Fails, was used for this purpose. The water intake locations were then divided (normalized) by the

reference data, and this provided a very fast way to get reasonable spectral reflectance indicators. A sample result derived by this normalization method is shown in Figure B.2. Water near Toledo (Maumee Bay) and Kelleys Island showed very strong indicators for an algal bloom that appeared to contain significant Microcystis as deduced by the spectral signature (Vincent et al., 2004) in combination with other concurrent observations. Avon Lake, Ohio, showed a less-noticeable bloom that was primarily localized to small pockets along shore. The algal bloom at Avon Lake was a surprise to the Ohio EPA as it did not show up in MODIS products because it was a near-shore bloom. Its spectral signature looked primarily like chlorophyll with potentially a low indication of Microcystis. Cleveland water intake appeared almost exactly the same as the Fails deep-water location and did not have observable algal indications.

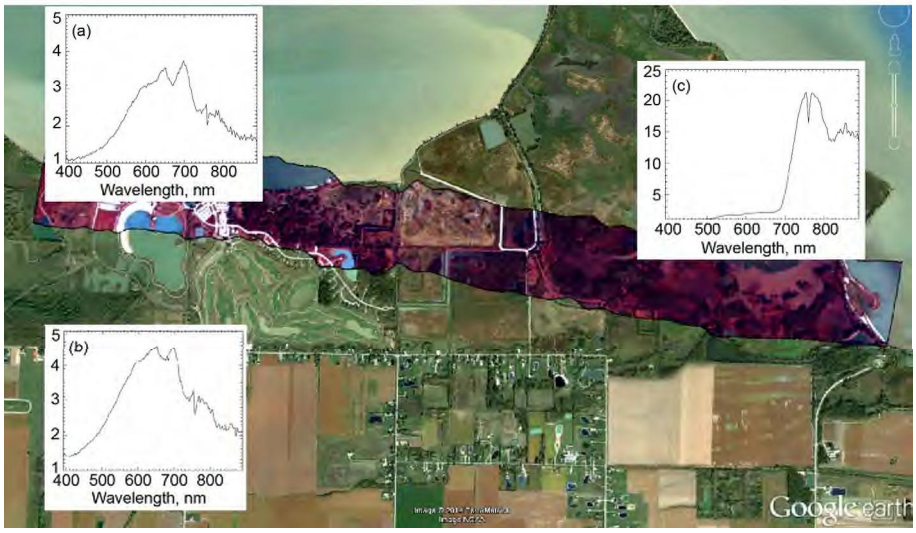

Figure B.1.—Sample of hyperspectral flight data at Maumee Bay State Park (Sept. 17, 2014). Copyright Google Earth.

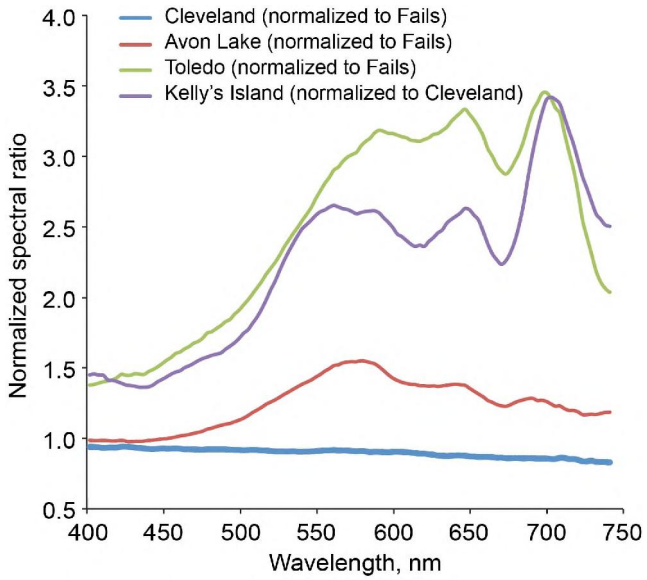

Figure B.2.—Normalized spectral results for various harmful algal bloom (HAB) intensities.

One finding that was very surprising from 2014 was the capability to observe indications of submerged algal mats when they are pulled up in the wake of passing freighters. In Figure B.3 there is a freighter (circled with yellow oval) that left a green dashed wake trail. HSI2 data of the green dashes were obtained, which appeared to be consistent with chlorophyll-a. In the MODIS image (lower right) from the same day there are no discernable indications of algae at that location, indicated by a yellow triangle.

For more rigorous data analysis, two parking lots near the study area were characterized for reflectance, and these locations were frequently revisited during each flight. All data from 2014 were empirically corrected for atmospheric effects both by using the data obtained from these reference locations and the other atmospheric correction techniques mentioned earlier.

Figure B.3.—Contrasting airborne image with MODIS (Moderate Resolution Imaging Spectroradiometer) satellite image (lower right).

References

Ali, K.A., et al., 2016: Application of Aqua MODIS Sensor Data for Estimating Chlorophyll a in the Turbid Case 2 Waters of Lake Erie Using Bio-Optical Models. GIScience & Remote Sensing, vol. 53, no. 4, DOI:10.1080/15481603.2016.1177248.

Ali, K.A.; and Ortiz, J.D., 2014: Multivariate Approach for Chlorophyll-a and Suspended Matter Retrievals in Case II Waters Using Hyperspectral Data. Hydrolog. Sci. J., vol. 59, pp. 1–14, DOI:10.1080/02626667.2014.964242.

Ali, K.A.; Witter, D.L.; and Ortiz, J.D., 2014a: Multivariate Approach To Estimate Color Producing Agents in Case 2 Waters Using First-Derivative Spectrophotometer Data. Geocarto Int., vol. 29, no. 2, pp. 102–127, DOI:10.1080/10106049.2012.743601.

Ali, K.A.; Witter, D.L.; and Ortiz, J.D., 2014b: Application of Empirical and Semi-Analytical Algorithms to MERIS Data for Estimating Chlorophyll a in Case 2 Waters of Lake Erie. Environ. Earth Sci., vol. 71, no. 9, pp. 4209–4220, DOI 10.1007/s12665-013-2814-0.

Anderson, D.M., 2004: The Growing Problem of Harmful Algae. Oceanus, vol. 43, no. 1, pp. 1–5.

Astoreca, R., et al., 2006: Variability of the Inherent and Apparent Optical Properties in a Highly Turbid Coastal Area: Impact on the Calibration of Remote Sensing Algorithms. EARSeL eProceedings, vol. 5, no. 1, pp. 1–17.

Avouris, D., et al., 2015: Algal and Cyanophyte Blooms in Lake Erie: Identifying Color-Producing Agents Using Derivative Spectroscopy, Water in a Changing Climate: Regional to Global Issues. Presented at the Third Annual Water Research Symposium Kent State University, Kent, OH.

Backer, Lorraine C.; and McGillicuddy, Dennis J., Jr., 2006: Harmful Algal Blooms at the Interface Between Coastal Oceanography and Human Health. Oceanography, vol. 19, no. 2, pp. 94–106.

Becker, R., et al., 2009: Mapping Cyanobacterial Blooms in the Great Lakes Using MODIS. J Great Lakes Res., vol. 35, pp. 447–453.

Bridgeman, Thomas B., et al., 2012: From River to Lake: Phosphorus Partitioning and Algal Community Compositional Changes in Western Lake Erie. J. Great Lakes Res., vol. 38, no. 1, pp. 90–97.

Buiteveld, H.; Hakvoort, J.H.M.; and Donze, M., 1994: Optical Properties of Pure Water. Proc. SPIE 2258, Ocean Optics XII, pp. 174–183.

Bullerjahn, G.S., et al., 2016: Global Solutions to Regional Problems: Collecting Global Expertise to Address the Problem of Harmful Cyanobacterial Blooms—A Lake Erie Case Study. Harmful Algae, vol. 54, pp. 223–238.

Butler, Ned, et al., 2009: Microcystins: A brief Overview of Their Toxicity and Effects, With Special Reference to Fish, Wildlife, and Livestock. California Environmental Protection Agency.

Chase, Alison, et al., 2013: Decomposition of In Situ Particulate Absorption Spectra. Methods in Oceanography, vol. 7, pp. 110–124.

Chesson, Peter L.; and Case, Ted J., 1986: Overview: Nonequilibrium Community Theories: Chance, Variability, History, and Coexistence. Community Ecology. J. Diamond and T. Case, eds., Harper and Row, New York, NY, pp. 229–239.

DeAngelis, Donald; and Waterhouse, J.C., 1987: Equilibrium and Nonequilibrium Concepts in Ecological Models. Ecol. Monogr., vol. 57, no. 1, pp. 1–21.

Falconer, Ian R., 1999: An Overview of Problems Caused By Toxic Blue-Green Algae (Cyanobacteria) in Drinking and Recreational Water. Environ. Toxicol., vol. 14, no. 1, pp. 5–12.

Falkowski, P.G., et al., 2004: The Evolution of Modern Eukaryotic Phytoplankton. Science, vol. 305, pp. 354–360.

Gao, B.-C., et al., 2009: Atmospheric Correction Algorithms for Hyperspectral Remote Sensing Data of Land and Ocean. Remote Sens. Environ., vol. 113, pp. S17–S24.

Golnick, P.C., et al., 2016: A Comparison of Water Sampling and Analytical Methods in Western Lake Erie. J. Great Lakes Res., vol. 42, no. 5, pp. 965–971.

Gons, H.J., 1999: Optical Teledetection of Chlorophyll *a* in Turbid Inland Waters. Environ. Sci. Technol., vol. 33, no. 7, pp. 1127–1132.

Gordon, H., et al., 1988: A Semianalytic Radiance Model of Ocean Color. J. Geophys. Res.-Atmos., vol. 93, no. D9, pp. 10909–10924.

Hallegraeff, G.M., 1993: A Review of Harmful Algal Blooms and Their Apparent Global Increase. Phycologia, vol. 32, no. 2, pp. 79–99.

HyspIRI Aquatic Studies Group, 2015: Coastal and Inland Aquatic Data Products for the Hyperspectral Infrared Imager (HyspIRI): A Preliminary Report by the HASG. http://hyspiri.jpl.nasa.gov/downloads/reports_whitepapers/HASG_White_Paper_Report_20150226_v3.pdf (Accessed Feb. 18, 2016).

Lekki, John, et al., 2009: Development of Hyperspectral Remote Sensing Capability for the Early Detection and Monitoring of Harmful Algal Blooms (HABs) in the Great Lakes. Proceedings of AIAA Infotech@Aerospace Conference (AIAA 2009–1978), Seattle, WA.

Moisan, John R.; Moisan, Tiffany A.H.; and Linkswiler, Matthew A., 2011: An Inverse Modeling Approach to Estimating Phytoplankton Pigment Concentrations From Phytoplankton Absorption Spectra. J. Geophys. Res.-Oceans, vol. 116, no. C9, pp. 148–227.

Morel, A., 1980: In-Water and Remote Measurements of Ocean Color. Bound.-Layer Meteor., vol. 18, no. 2, pp. 177–201.

Morel, A., and Prieur, L., 1977: Analysis of Variations in Ocean Color. Limnol. Oceanogr., vol. 22, no. 4, pp. 709–722.

Mueller, J.L., 2003: In-Water Radiometric Profile Measurements and Data Analysis Protocols. Ocean Optics Protocols for Satellite Ocean Color Sensor Validation, Revision, vol. 4, pp. 7–20.

National Academy of Sciences, 2007: Earth Science and Applications From Space: National Imperatives for the Next Decade and Beyond. The National Academies Press, Washington, DC.

Oregon State University, 2009: Hyperspectral Imager for the Coastal Ocean (HICO). http://hico.coas.oregonstate.edu/index.shtml (Accessed July 27, 2015).

O'Reilly, J., et al., 1998: Ocean Color Algorithms for SeaWiFS. J. Geophys. Res., vol. 103, no. 24, pp. 937–953.

O'Reilly, John E., 2000: SeaWiFS Postlaunch Calibration and Validation Analyses. SeaWiFS Postlaunch Technical Report Series, NASA Technical Memorandum 2000–206892, vol. 11, part 3.

Ortiz, Joseph D., et al., 2013: Evaluating Multiple Colour-Producing Agents in Case II Waters From Lake Erie. Int. J. Remote Sens., vol. 34, no. 24, pp. 8854–8880.

Ortiz, J.D.; Schiller, S.; and Luvall, J., 2015: Climate Change and the Potential Future of CyanoHABS in Sandusky Bay: Insights From the 2015 CyanoHAB. Presented at the Water in a Changing Climate: Regional to Global Issues, Kent, OH.

Randolph, K., et al., 2008: Hyperspectral Remote Sensing of Cyanobacteria in Turbid Productive Water Using Optically Active Pigments, Chlorophyll a and Phycocyanin. Remote Sens. Environ., vol. 112, no. 11, pp. 4009–4019.

Richardson, Laurie L., 1996: Remote Sensing of Algal Bloom Dynamics. BioScience, vol. 46, no. 7, pp. 492–501.

Rinta-Kanto, J.M., et al., 2005: Quantification of Toxic Microcystis spp. During the 2003 and 2004 Blooms in Western Lake Erie Using Quantitative Real-Time PCR. Environ. Sci. Technol., vol. 39, no. 11, pp. 4198–4205.

Ryan, John P., et al., 2014: Application of the Hyperspectral Imager for the Coastal Ocean to Phytoplankton Ecology Studies in Monterey Bay, CA, USA. Remote Sens., vol. 6, no. 2, pp. 1007–1025.

Sayers, M., et al., 2016: Cyanobacteria Blooms in Three Eutrophic Basins of the Great Lakes: A Comparative Analysis Using Satellite Remote Sensing. Int. J. Remote Sens., vol. 37, no. 17, pp. 4148–4171.

Science Definition Team, 2012: Pre-Aerosol, Clouds, and Ocean Ecosystem (PACE) Mission Science Definition Team Report. http://decadal.gsfc.nasa.gov/PACE/PACE_SDT_Report_final.pdf (Accessed Feb. 18, 2016).

Shuchman, R.A., et al., 2013: An Algorithm to Retrieve Chlorophyll, Dissolved Organic Carbon, and Suspended Minerals From Great Lakes Satellite Data. J. Great Lakes Res., vol. 39, pp. 14–33.

Simis, Stefan G.; Peters S.W.; and Gons, H.J., 2005: Remote Sensing of the Cyanobacterial Pigment Phycocyanin in Turbid Inland Water. Limnol Oceanogr., vol. 50, no. 1, pp. 237–245.

Stumpf, Richard P., et al., 2012: Interannual Variability of Cyanobacterial Blooms in Lake Erie. PLoS ONE, vol. 7, no. 8. http://journals.plos.org/plosone/article?id=10.1371/journal.pone.0042444 (Accessed Feb. 2, 2016).

Szell, A.; Turner, K.; and Ortiz, J.D., 2015: Multi-Temporal Water Quality Assessment Using Landsat TM Imagery, in a Changing Climate: Regional to Global Issues. Presented at the Third Annual Kent State University Water Symposium, Kent, OH.

Turpie, K, et al., 2016: Earth System Science Theme: Marine and Terrestrial Ecosystems and Natural Resource Management (III). White Paper to Steering Committee, National Academies of Science, Engineering, and Medicine Study, Earth Science and Applications from Space, Request for Information.

University of Colorado, 1999: ATmosphere REMoval Program (ATREM). User's Guide, Version 3.1.

Vincent, R.K., et al., 2004: Phycocyanin Detection From LANDSAT TM Data for Mapping Cyanobacterial Blooms in Lake Erie. Remote Sens. Environ., vol. 89, pp. 381−392.

Witter, D., et al., 2009: Assessing the Application of SeaWiFS Ocean Color Algorithms to Lake Erie. J. Great Lakes Res., vol. 35, pp. 361–370.

Wynne, T.T., et al. 2010: Characterizing a Cyanobacterial Bloom in Western Lake Erie Using Satellite Imagery and Meteorological Data. Limnol Oceanogr., vol. 55, no. 5, pp. 2025–2036.

Wynne, T.T., et al., 2008: Relating Spectral Shape to Cyanobacterial Blooms in the Laurentian Great Lakes. Int. J. Remote Sens., vol. 29, no. 12, pp. 3665–3672.